

AD-A131 250 SOME CLASSICAL MECHANISMS INFLUENCING THE HIGH-ALTITUDE 1/1

NUCLEAR ENVIRONMENT(U) JAYCOR SAN DIEGO CA

J L SPERLING ET AL. 15 MAY 82 JAYCOR-J530-82-012

UNCLASSIFIED DNA-TR-81-128 DNA001-81-C-0148

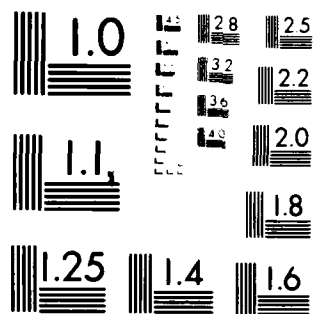
F/G 18/3 NL

END

DATE
FILMED

9 83

DTIC



12

DNA-TR-81-128

ADA 131250

SOME CLASSICAL MECHANISMS INFLUENCING THE HIGH-ALTITUDE NUCLEAR ENVIRONMENT

J. L. Sperling
S. Hamasaki
JAYCOR
P.O. Box 85154
San Diego, California 92138

15 May 1982

Technical Report

CONTRACT No. DNA 001-81-C-0148

APPROVED FOR PUBLIC RELEASE;
DISTRIBUTION UNLIMITED.

THIS WORK WAS SPONSORED BY THE DEFENSE NUCLEAR AGENCY
UNDER RDT&E RMSS CODE B322081466 S99QAXHC00026 H2590D.

DTIC FILE COPY

Prepared for
Director
DEFENSE NUCLEAR AGENCY
Washington, DC 20305

DTIC
ELECTE
AUG 10 1983
S B

83 06 20 001

Destroy this report when it is no longer
needed. Do not return to sender.

PLEASE NOTIFY THE DEFENSE NUCLEAR AGENCY,
ATTN: STTI, WASHINGTON, D.C. 20305, IF
YOUR ADDRESS IS INCORRECT, IF YOU WISH TO
BE DELETED FROM THE DISTRIBUTION LIST, OR
IF THE ADDRESSEE IS NO LONGER EMPLOYED BY
YOUR ORGANIZATION.



SECURITY CLASSIFICATION OF THIS PAGE (When Data Entered)

DD FORM 1473 EDITION OF 1 NOV 65 IS OBSOLETE

SECURITY CLASSIFICATION OF THIS PAGE (When Data Entered)

TABLE OF CONTENTS

| <u>Section</u> | <u>Page</u> |
|---|-------------|
| LIST OF ILLUSTRATIONS | 2 |
| SUMMARY | 5 |
| 1. THE DECAY OF STRUCTURE BY CHARGE EXCHANGE | 8 |
| 1.1 Introduction | 8 |
| 1.2 Model | 10 |
| 1.3 Results | 14 |
| 1.4 Concluding Remarks | 38 |
| References | 39 |
| 2. ANALYSIS OF RADIATIVE RECOMBINATION EFFECTS ON DENSITY PROFILES AND THEIR FOURIER SPECTRUMS | 40 |
| 2.1 Introduction | 40 |
| 2.2 Model | 41 |
| 2.3 Examples | 43 |
| 2.4 Summary and Conclusions | 67 |
| References | 70 |
| 3. NONADIABATICITY AND THE HIGH-ALTITUDE NUCLEAR ENVIRONMENT | 71 |
| 3.1 Introduction | 71 |
| 3.2 Fokker-Planck Model for Nonadiabaticity | 72 |
| 3.3 Example for the Vicinity of an Ionospheric Nuclear Burst | 76 |
| 3.4 Nonadiabaticity in the Magnetosphere | 80 |
| 3.5 Summary and Concluding Remarks | 82 |
| References | 83 |



| | |
|--------------------|-------------------------------------|
| Accession for | |
| REC'D | <input checked="" type="checkbox"/> |
| FILED | <input type="checkbox"/> |
| Unrecorded | <input type="checkbox"/> |
| Index | |
| Date | |
| Distribution/ | |
| Availability Codes | |
| Dist | Avail and/or Special |
| A | |

LIST OF ILLUSTRATIONS

| <u>Figure</u> | | <u>Page</u> |
|---------------|---|-------------|
| 1.1 | Model for the calculation of structure decay due to successive charge exchange and impact ionization collisions | 11 |
| 1.2 | Model for calculating $f(z)$, the fraction of fast neutrals which undergo impact ionization collisions before crossing the boundaries of the structure | 13 |
| 1.3 | $f(z)$ as given by Eq. (1.12) versus a | 15 |
| 1.4 | $n(h)/n_0$ versus $k(\text{km}^{-1})$ for singly ionized monatomic oxygen ions with a speed of 5×10^2 km/s. The CIRA 1972 reference atmosphere for an exospheric temperature of 900°K is used. The various curves from top to bottom correspond to altitudes of $h = 500$ km, 400 km, 300 km, 200 km, and 120 km. The initial altitude of the ions is $h = 600$ km | 17-21 |
| 1.5 | $n(h)/n_0$ versus $k(\text{km}^{-1})$ for singly ionized monatomic oxygen ions with a speed of 1×10^3 km/s. The CIRA 1972 reference atmosphere for an exospheric temperature of 900°K is used. The various curves from top to bottom correspond to altitudes of 500 km, 400 km, 300 km, 200 km, and 120 km. The initial altitude of the ions is $h = 600$ km | 22-26 |
| 1.6 | $n(h)/n_0$ versus $k(\text{km}^{-1})$ for singly ionized monatomic oxygen ions with a speed of 5×10^2 km/s. The CIRA 1972 reference atmosphere for an exospheric temperature of 1800°K is used. The various curves from top to bottom correspond to altitudes of 500 km, 400 km, 300 km, 200 km, and 120 km. The initial altitude of the ions is $h = 600$ km | 27-31 |
| 1.7 | $n(h)/n_0$ versus $k(\text{km}^{-1})$ for singly ionized monatomic oxygen ions with a speed of 1×10^3 km/s. The CIRA 1972 reference atmosphere for an exospheric temperature of 1800°K is used. The various curves from top to bottom correspond to altitudes of 500 km, 400 km, 300 km, 200 km, and 120 km. The initial altitude of the ions is $h = 600$ km | 32-36 |

LIST OF ILLUSTRATIONS (Continued)

| <u>Figure</u> | <u>Page</u> |
|--|-------------|
| 2.1 $a_0(t)/N$ versus ϵ for $T_e = 0.043$ eV and 0.518 eV, respectively. Initial density profile specified by Eq. (2.13) | 46-49 |
| 2.2 $n(x,t)/N$ versus x/L for $T_e = 0.043$ eV and various ϵ . Initial density profile specified by Eq. (2.13) | 50-53 |
| 2.3 $n(x,t)/N$ versus x/L for $T_e = 0.518$ eV and various ϵ . Initial density profile specified by Eq. (2.13) | 54-57 |
| 2.4 $ a_p(t)/a_0(t) $ versus ϵ for $T_e = 0.043$ eV and various p . Initial density profile specified by Eq. (2.13) | 59-62 |
| 2.5 $ a_p(t)/a_0(t) $ versus ϵ for $T_e = 0.518$ eV and various p . Initial density profile specified by Eq. (2.13) | 63-66 |
| 2.6a $t(s)$ versus ϵ for $T_e = 0.043$ eV. The numbers at the top and right represent $N(\text{cm}^{-3})$ | 68 |
| 2.6b $t(s)$ versus ϵ for $T_e = 0.518$ eV. The numbers at the top and right represent $N(\text{cm}^{-3})$ | 69 |
| 3.1 Qualitative plot of $K(v^2/v_{10}^2)$ versus v^2/v_{10}^2 | 74 |
| 3.2a $2\mu/mc^2$ (G^{-1}) versus $z(\text{km})$ for singly ionized monatomic oxygen ions with $v = 1 \times 10^3$ km/s | 78 |
| 3.2b $2\mu/mc^2$ (G^{-1}) versus $z(\text{km})$ for singly ionized monatomic oxygen ions with $v = 2 \times 10^3$ km/s | 79 |

SUMMARY

Classical mechanisms (e.g., collisions, chemistry, single particle dynamics, and radiation) always contribute to the evolution of nonequilibrium plasmas. From the theoretical, experimental, or observational viewpoints, the study of classical mechanisms is an especially important first step which defines the upper limit to the time scale for plasma evolution and also gives the minimum level of turbulence required to make a plasma anomalous. In fact, the development of a plasma can be classified as being anomalous only after the classical behavior of the plasma is understood. In practice, a particular plasma can consist of different components, some of which act in a primarily classical way, while the rest have an anomalous behavior. For example, in the tokamak fusion-oriented device, ion heat transport is close to being classical while electron heat transport is anomalous. However, in the bumpy torus fusion-oriented device, electron transport is classical while ion transport is anomalous.

Classical mechanisms are necessary, basic ingredients in theoretical or numerical representations of the high-altitude nuclear environment.

This report is a compilation of three separate papers, each of which describes and analyzes a classical mechanism which can influence the ionospheric and magnetospheric environments following a high-altitude nuclear burst. The three mechanisms considered are (1) charge exchange, (2) radiative recombination, and (3) nonadiabaticity.

Chapter 1, "The Decay of Structure by Charge Exchange," considers structural decay by charge exchange. Particular emphasis is given to those structures, consisting of energetic ions with kinetic energies on the order of 10 or even larger than 100 keV, which may develop following a high-altitude nuclear burst in the ionosphere. Charge exchange affects the lifetime of these structures by transforming ions into neutrals whose motion is not fixed to the magnetic field geometry. The result is a loss rate for particles which does not depend on the magnetic field to lowest order. This loss is either convective or diffusive

depending on whether the effective neutral mean free path across the structure is larger or smaller than the structure size transverse to the magnetic field, respectively. It is demonstrated that structures, consisting initially of monatomic oxygen ions, are attenuated by at least two orders of magnitude in traveling from altitudes above 400 kilometers down to altitudes below approximately 200 kilometers where strong ionization of ambient ionospheric neutrals and fluid structuring occurs. Recent fluid simulations suggest that density variations, below 15 percent on a larger density profile, do not determine the long-term outer scale length of the power spectral density and so the attenuation of structure whose scale size is smaller than 10 kilometers may not impose the outer scale length at lower altitudes. Indeed, morphology, consisting of energetic ions with pitch angles approaching 90 degrees and forming near the geomagnetic equator, imply outer scale lengths at lower altitudes which are comparable to or greater than 100 kilometers. It follows that structures like prompt striations, whose scale size is comparable to or smaller than the ion-gyroradius, do not specify the long-term outer scale lengths at lower altitudes by propagation from starting points at higher altitudes.

Chapter 2, "Analysis of Radiative Recombination Effects on Density Profiles and Their Fourier Spectrums," discusses the role that radiative recombination can play in the modification and decay of cool, dense, ionospheric morphology. Fourier spectrums of density profiles are functions of time when recombination is active. Initially, Fourier components which are not at first present in the spectrum grow relative to the Fourier component which alone is present in a uniform plasma. However, eventually they and the other Fourier components present because of plasma nonuniformity decay relative to the uniform Fourier component. Because the uniform Fourier component, which is proportional to total density, always decays because of recombination, it is evident that for long times the plasma becomes uniform on a faster time scale than total ionization decay.

Chapter 3, "Nonadiabaticity and the High-Altitude Nuclear Environment," points out that nonadiabatic changes in magnetic moment may play a substantial role in the evolution of the ionosphere and magnetosphere following a high-altitude nuclear burst. This is because the magnetic moment is only an adiabatic constant of motion in magnetic field configurations having sufficiently gentle magnetic field gradients and slow temporal variations. However, spatial or temporal variations of the magnetic field of sufficient size are not consistent with the

constancy of the magnetic moment. This nonadiabaticity can be a factor in the ionospheric and magnetospheric environments, following a high-altitude nuclear burst, in two ways. First, a high-altitude nuclear burst can push aside the ambient geomagnetic field. A new magnetic field configuration is created with substantial magnetic field gradients and local extremums in magnetic field strength where nonadiabatic jumps in the magnetic moment can occur. Because these jumps depend on both pitch angle and gyrophase, nonadiabaticity supports the premise of outer scale length being at least as large as the gyroradius of energetic ions. Second, ions injected into the magnetosphere following a high-altitude nuclear burst can be confined on a specific magnetic flux surface in the magnetosphere only if their kinetic energy is below a bound determined by nonadiabatic considerations. Hence, nonadiabatic effects can influence the coupled ionospheric and magnetospheric current system.

1. THE DECAY OF STRUCTURE BY CHARGE EXCHANGE

1.1 INTRODUCTION

The undisturbed ionosphere is a complex mixture of charged and neutral particle species. One way in which a nuclear detonation can modify this composition is through the generation of ions and neutrals with energies on the order of 10 or even larger than 100 keV. Once formed, the fast, high energy ions can be transformed into fast neutrals by charge exchange collisions while fast neutrals can be transformed back into ions by impact ionization collisions.^{1.1} Between charge exchange and impact ionization events, high energy ions and neutrals can increase the thermal charged particle density of the ionosphere through ionization collisions.^{1.2} Eventually, a sufficiently large number of collisions occur so that the initially high energy particles become part of the thermal background.

The persistence of coherent structures, consisting of fast ions, from higher to lower altitudes is adversely affected by the charge exchange process. Ions are strongly coupled to the magnetic field geometry but neutrals are not. Consequently, a charge exchange collision permits a fast particle to traverse a plasma unimpeded by the magnetic field. Two different situations are evident. If the probability of an impact ionization collision by a neutral is low before fast particles cross a structural boundary, then the loss of fast particles is convective. Conversely, if the probability is high, then fast particle loss is diffusive. In general, convective loss tends to degrade structure more rapidly than diffusive loss. Nevertheless, if the neutral mean free path for collision is larger than the gyroradius of fast ions, the diffusive loss of fast particles is always larger than the loss rate associated with classical ion diffusion across a magnetic field.

A substantial qualitative statement, which is supported by the numerical results subsequently presented, can be made regarding the persistence of structure consisting of fast ions down magnetic field lines. Specifically, structure originating at a relative'v high altitude (i.e., ≥ 400 km) and having a transverse

size which is comparable to or smaller than the gyroradius of fast ions (e.g., monatomic oxygen) will be substantially degraded by the successive charge exchange and impact ionization processes before it reaches lower altitudes (i.e., ≥ 100 km). To demonstrate this assertion, we first assume that the structure has a sufficiently small size transverse to the magnetic field so that the neutrals formed following a charge exchange collision are convectively lost. This implies that, for straight magnetic field lines, the ion pitch angles must be sufficiently oblique. Quantitatively, for a cross-section for impact ionization of $\sim 4 \times 10^{-16} \text{ cm}^2$ and a background neutral density of $\sim 1 \times 10^9 \text{ cm}^{-3}$, the structural size perpendicular to the magnetic field must be smaller than ~ 25 km. By comparison, a singly ionized, monatomic oxygen ion with a speed of $1 \times 10^3 \text{ km/s}$ in a magnetic field of 0.3 gauss has a gyroradius of 5.6 km. When neutrals are convectively lost the decay of structure is determined by the rate of charge exchange collisions. For this situation, the structural density decays in accordance with

$$n(z) = n(z_0) \exp \left[- \sigma_x \frac{v}{v_{\parallel}} \int_{z_0}^z dz' n_n(z') \right] \quad (1.1)$$

Here $n(z)$, σ , v , v_{\parallel} , and $n_n(z')$ are the ion density at position z , the charge exchange cross section, total ion speed, ion speed parallel to the magnetic field, and neutral density at position z' , respectively. In writing Eq. (1.1), σ_x , v , and v_{\parallel} are treated as constants. For $\sigma_x \approx 1 \times 10^{-15} \text{ cm}^2$, $v/v_{\parallel} \approx 1$, $n_n(z') \approx 1 \times 10^9 \text{ cm}^{-3}$ and $z - z_0 \approx 100 \text{ km}$, it follows that

$$n(z) \approx n(z_0) \exp(-10) \approx 4.5 \times 10^{-5} n(z_0) \quad (1.2)$$

Equation (1.2) implies severe degradation of structure with scale size smaller than the fast ion-gyroradius. Now, recent fluid simulations of the EXB gradient drift instability suggest that density perturbations, smaller than 15 percent on a larger density profile, do not determine the outer scale of the power spectral density.^{1.3} It seems likely that attenuation to the degree specified by Eq. (1.2) should be more than sufficient to preclude this structure from determining the outer scale at the lower altitudes.

Prompt striations are structures with a scale size which is comparable to or smaller than the gyroradius of energetic ions.^{1.4} It has been previously demonstrated that these structures are strongly stabilized by the background plasma and

electromagnetic effects in the limit of small density gradients, and so prompt striations if they develop are likely limited to high altitude (i.e., ≥ 1000 km) in the HANE environment when density gradients are small.^{1.5,1.6} It is clear from the discussion in the previous paragraph that the propagation of ions, which are organized as prompt striations, down magnetic field lines results in the essential destruction of the prompt striations once altitudes like ~ 100 to ~ 200 km are reached.

This chapter is divided in the following way. Section 1.2 gives the model for the decay of structure due to consecutive charge exchange and impact ionization collisions. Section 1.3 presents results of the numerical evaluation of the model. Section 1.4 summarizes the results and conclusions.

1.2 MODEL

The plasma model illustrated in Figure 1.1 is used. A uniform magnetic field is aligned along the z-direction which is at an angle of θ_1 , with respect to gravity, i.e.,

$$\theta_1 = \cos^{-1}[\vec{g} \cdot \vec{B} / (|\vec{g}| |\vec{B}|)] \quad . \quad (1.3)$$

The y-direction is ignorable and the structure, consisting of high energy ions, has a width, $2L$, in the x-direction. The calculations assume that the ions within the structure have the same speed and pitch angle,

$$\theta_2 = \cos^{-1}(v_{\parallel}/v) \quad . \quad (1.4)$$

As the ions travel down the magnetic field lines, the number of charge exchange collisions which occur in an infinitesimal distance, dz , is

$$dn(z) = n(z) \lambda_x^{-1}(z) dz \quad , \quad (1.5)$$

where

$$\lambda_x(z) = \left[\sum_n \sigma_{xn} n_n(z) \right]^{-1} \quad . \quad (1.6)$$

In Eq. (1.6) the cross section for collision with the background species is represented by σ_{xn} and the density of the background neutral species at z is $n_n(z)$.

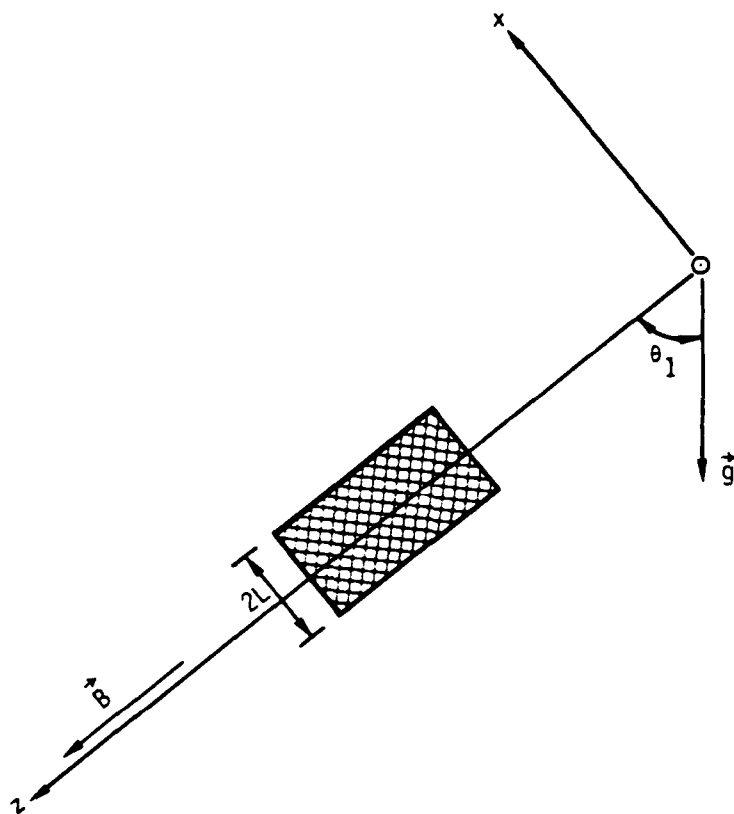


Figure 1.1. Model for the calculation of structure decay due to successive charge exchange and impact ionization collisions. The structure consisting of particles, with high energy, is crosshatched.

Now a fraction of the charge exchange collisions, $f(z)$, results in neutrals which undergo subsequent impact ionization collisions before the neutrals can leave the structure. Hence, the ultimate decrease in the number of fast particles within structure as a result of charge exchange collisions over a distance, dz , and a time, dt , is

$$\begin{aligned} dn(z) &= -n(z)\lambda_x^{-1}(z)[1 - f(z)]dz \\ &= -n(z)\lambda_x^{-1}(z)[1 - f(z)]v_{\parallel}dt \end{aligned} \quad (1.7)$$

Equation (1.7) implies that

$$n(z) = n(z_0) \exp \left\{ - \int_{z_0}^z dz' \lambda_x^{-1}(z') [1 - f(z')] \right\} \quad (1.8)$$

Figure 1.2 illustrates the model used to derive an expression for $f(z)$, the fraction of fast neutrals which undergo impact ionization collisions before crossing the boundaries of the structure. The derivation assumes that the fast ion and fast neutral density within the structure is not a function of spatial coordinate. Now charge exchange collisions do not depend upon ion-gyrophase and so the fast neutral velocity distribution function formed because of charge exchange is

$$g(\vec{v}') = \frac{\delta(v' - v) \delta(\theta' - \theta_2)}{2\pi v^2 \sin(\theta_2)} \quad (1.9)$$

which is independent of the azimuthal angle ϕ' . Equation (1.9) assumes that the fast neutral has the same velocity vector, at the point of charge exchange collision, as the ion from which it is created. It follows that

$$f(z) = 1 - \frac{1}{L\pi} \int_0^{\pi/2} d\phi' \int_0^{2L} dx \exp \left[- \frac{x \csc(\theta_2) \csc(\phi')}{\lambda_I(z)} \right] \quad (1.10)$$

where

$$\lambda_I(z) = \left[\sum_n n_n(z) \sigma_{In} \right]^{-1} \quad (1.11)$$

and σ_{In} is the impact ionization cross section for collision of a fast neutral with background neutral species, n . In writing Eqs. (1.10-1.11), it has been assumed

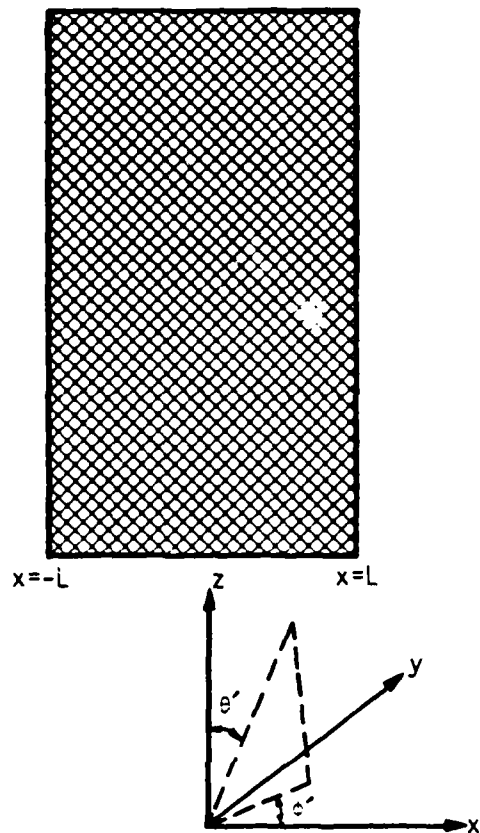


Figure 1.2. Model for calculating $f(z)$, the fraction of fast neutrals which undergo impact ionization collisions before crossing the boundaries of the structure. The structure consisting of particles, with high energy, is crosshatched.

that the mean free path for impact ionization collision is evaluated at the altitude where the fast neutrals are formed. This approximation permits an analytic integration of Eq. (1.10) and is asymptotically valid, in the limit of greatest present interest, when the size of the structure transverse to the magnetic field is smaller than the atmospheric scale height. The integration of Eq. (1.10) implies that

$$f(z) = \frac{2}{\pi a} [aK_1(a) - 1] + \frac{2}{\pi} \left\{ aK_0(a) + \frac{\pi}{2} a [L_0(a)K_1(a) + L_1(a)K_0(a)] \right\}, \quad (1.12)$$

with

$$a = [2L/\lambda_I(z)] \csc(\theta_2) \quad . \quad (1.13)$$

Several different functions are used in Eq. (1.12): the modified Bessel function of the second kind and order zero $[K_0(a)]$, the modified Bessel function of the second kind and order one $[K_1(a)]$,^{1.7} the modified Struve function of order zero $[L_0(a)]$,^{1.8} and the modified Struve function of order one $[L_1(a)]$.^{1.8}

Figure 1.3 is a plot of the fraction, $f(z)$, as a function of the non-dimensional parameter, a . The figure demonstrates that $f(z)$ has the correct asymptotic behavior. For $a \gg 1$, the effective mean free path across the structure is much smaller than the size of the structure. Essentially all the fast neutrals formed undergo an impact ionization collision before they can cross the structure boundary and $f(z) \rightarrow 1$. For $a \ll 1$, the effective mean free path across the structure is much larger than the structural size. Fast neutrals are lost before an impact ionization collision can occur within the structure and appropriately, $f(z) \rightarrow 0$.

1.3 RESULTS

The quantitative results presented in this subsection emphasize monatomic oxygen particles with speeds of 5×10^2 km/s and 1×10^3 km/s. For a speed of 5×10^2 km/s, the appropriate cross sections for charge exchange used are 1×10^{-15} cm², 1.5×10^{-15} cm², and 1.5×10^{-15} cm² for collisions of singly ionized, energetic,

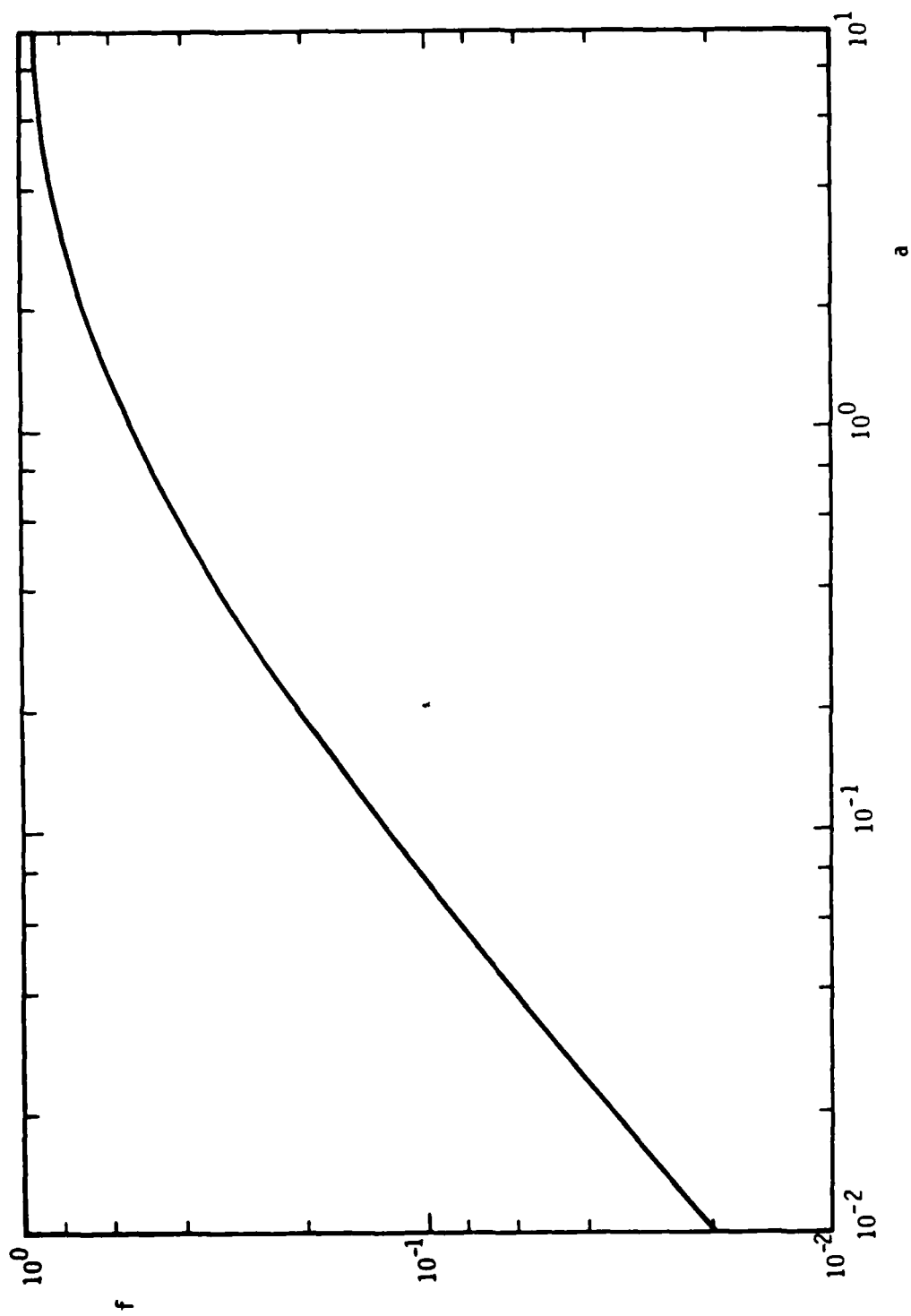


Figure 1.3. $f(z)$ as given by Eq. (1.12) versus a .

monatomic oxygen ions with monatomic oxygen atoms, diatomic oxygen molecules, and diatomic nitrogen molecules, respectively.^{1.1,1.9} The cross section for impact ionization is $2 \times 10^{-16} \text{ cm}^2$ for collision of the energetic, monatomic oxygen atoms with either monatomic oxygen atoms, diatomic oxygen molecules, or diatomic oxygen molecules.^{1.1,1.9} Similarly, for energetic, monatomic oxygen ions with speeds of $1 \times 10^3 \text{ km/s}$, the cross sections for charge exchange which are used are $8 \times 10^{-16} \text{ cm}^2$, $1 \times 10^{-15} \text{ cm}^2$, and $1 \times 10^{-15} \text{ cm}^2$, respectively, for collision with monatomic oxygen atoms, diatomic oxygen molecules, and diatomic nitrogen molecules, respectively.^{1.1,1.9} The corresponding cross section for impact ionization of energetic, monatomic oxygen atoms by collision with either monatomic oxygen atoms, diatomic oxygen molecules, or diatomic nitrogen molecules is $4 \times 10^{-16} \text{ cm}^2$.^{1.1,1.9}

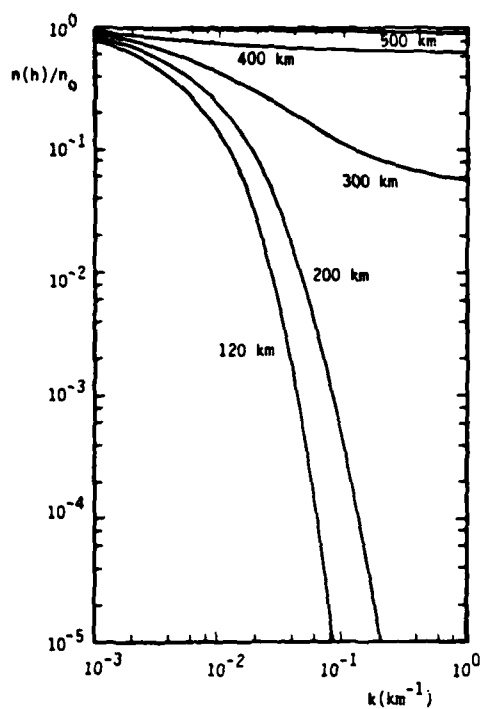
Figures 1.4-1.7 are plots of $n(h)/n_0$ versus $k(\text{km}^{-1})$ for monatomic oxygen ions with various pitch angles, various orientations of the geomagnetic field with respect to gravity, and two different CIRA reference atmospheres. Here $n(h)/n_0$ is the ion density at an altitude h in units of the density at the starting point of the ion structure which is assumed to be at an altitude of 600 km. The inverse of the Fourier wavenumber, k , is approximately equivalent to the structural size transverse to the ambient magnetic field. It is evident from the way that the figures are plotted that it is possible to determine the attenuation of structure, for a specific wavenumber, k , from some higher altitude, h_1 , to some lower altitude, h_2 , by taking the ratio of $[n(h_1)/n_0]/[n(h_2)/n_0]$ where $n(h_{1,2})/n_0$ are determined from the figures.

Figures 1.4-1.7 have the following qualitative form. For an initial altitude of 600 km, the disparity in the attenuation of small structure as compared to large structure increases as altitude decreases. This is a consequence of particle loss being more rapid (i.e., convective) for small structure and slower (i.e., diffusive) for large structure. Because the convective loss is only weakly dependent on wavenumber when it is active [cf, Eq. (1.1)], decay is roughly equal for all morphology whose scale size is smaller than the mean free path, across the structure, for impact ionization.

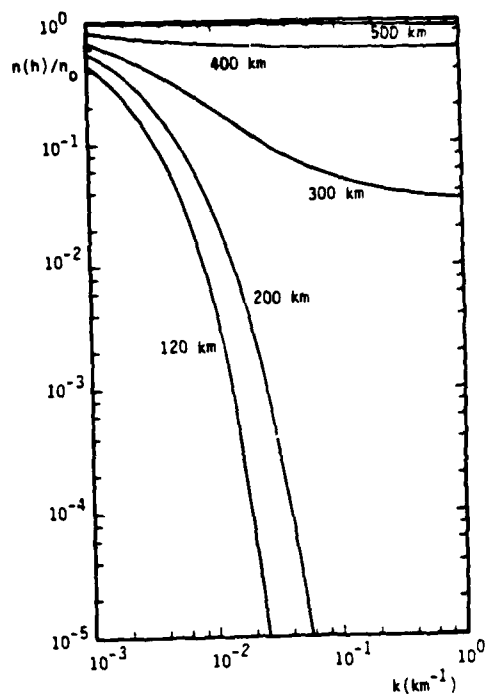
Figures 1.4-1.7 demonstrate that the persistence of structure down to lower altitudes is decreased for values of θ_1 deviating from 0 and approaching $\pi/2$. The larger values of θ_1 imply that structure originates closer to the geomagnetic

Figure 1.4. $n(h)/n_0$ versus $k(\text{km}^{-1})$ for singly ionized monatomic oxygen ions with a speed of 5×10^2 km/s. The CIRA 1972 reference atmosphere for an exospheric temperature of 900°K is used. The various curves from top to bottom correspond to altitudes of $h = 500$ km, 400 km, 300 km, 200 km, and 120 km. The initial altitude of the ions is $h = 600$ km. (Sheet 1 of 5)

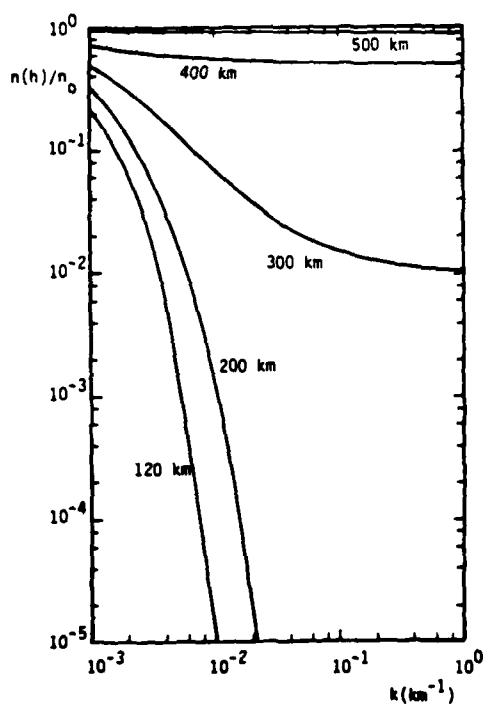
- (a) $\theta_1 = \pi/18$, $\theta_2 = \pi/18$
- (b) $\theta_1 = \pi/18$, $\theta_2 = \pi/6$
- (c) $\theta_1 = \pi/18$, $\theta_2 = 5\pi/18$
- (d) $\theta_1 = \pi/18$, $\theta_2 = 7\pi/18$
- (e) $\theta_1 = \pi/6$, $\theta_2 = \pi/18$
- (f) $\theta_1 = \pi/6$, $\theta_2 = \pi/6$
- (g) $\theta_1 = \pi/6$, $\theta_2 = 5\pi/18$
- (h) $\theta_1 = \pi/6$, $\theta_2 = 7\pi/18$
- (i) $\theta_1 = 5\pi/18$, $\theta_2 = \pi/18$
- (j) $\theta_1 = 5\pi/18$, $\theta_2 = \pi/6$
- (k) $\theta_1 = 5\pi/18$, $\theta_2 = 5\pi/18$
- (l) $\theta_1 = 5\pi/18$, $\theta_2 = 7\pi/18$
- (m) $\theta_1 = 7\pi/18$, $\theta_2 = \pi/18$
- (n) $\theta_1 = 7\pi/18$, $\theta_2 = \pi/6$
- (o) $\theta_1 = 7\pi/18$, $\theta_2 = 5\pi/18$
- (p) $\theta_1 = 7\pi/18$, $\theta_2 = 7\pi/18$



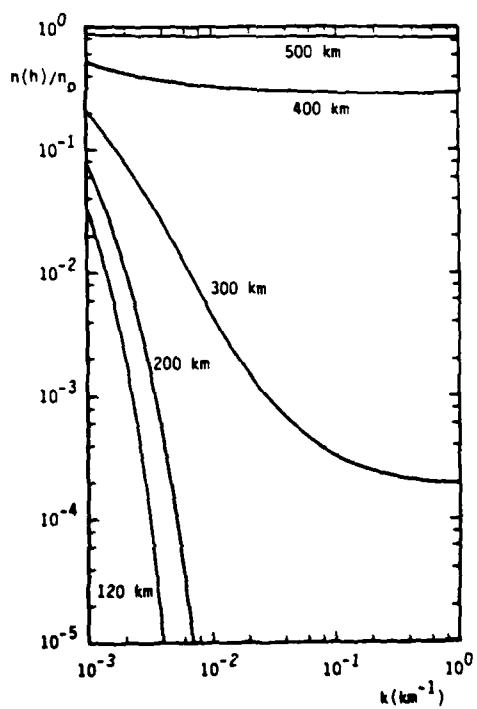
(a)



(b)

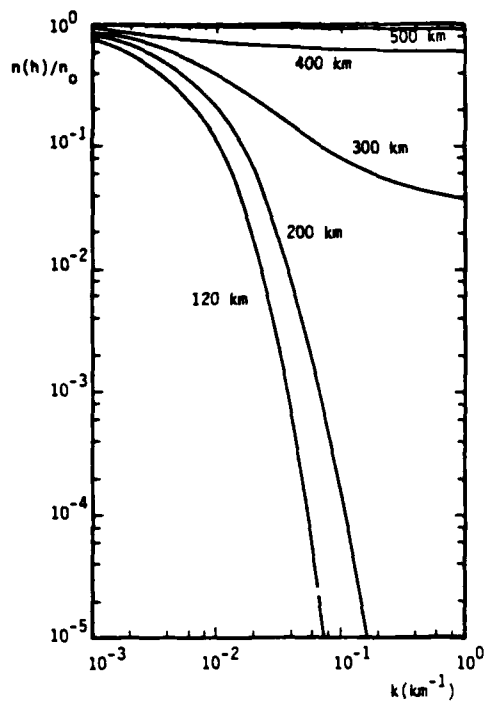


(c)

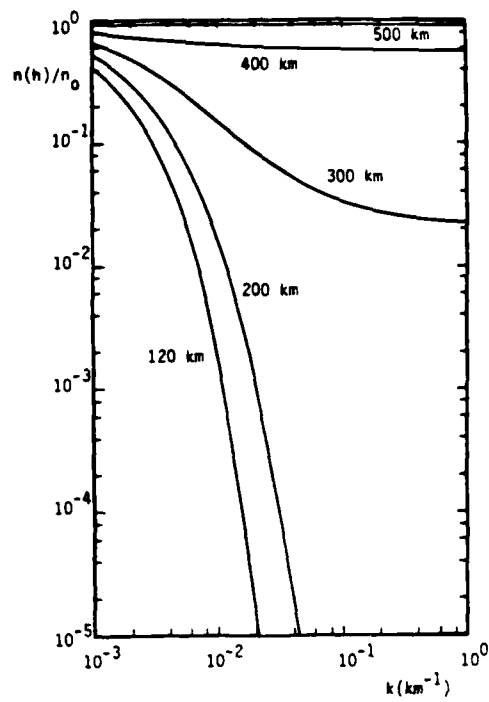


(d)

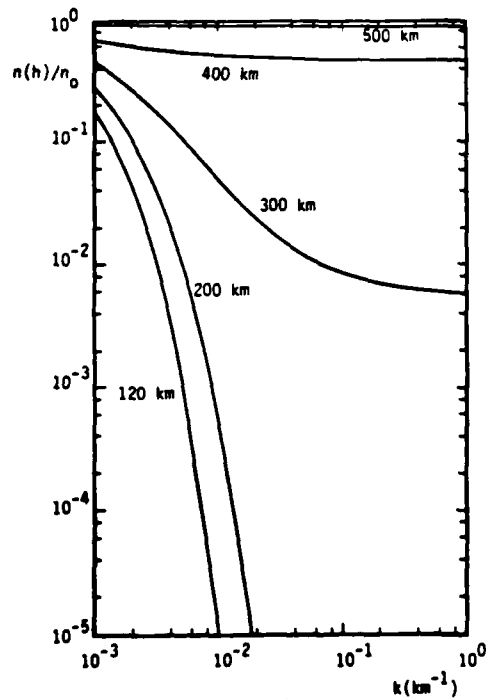
Figure 1.4. Continued (Sheet 2 of 5)



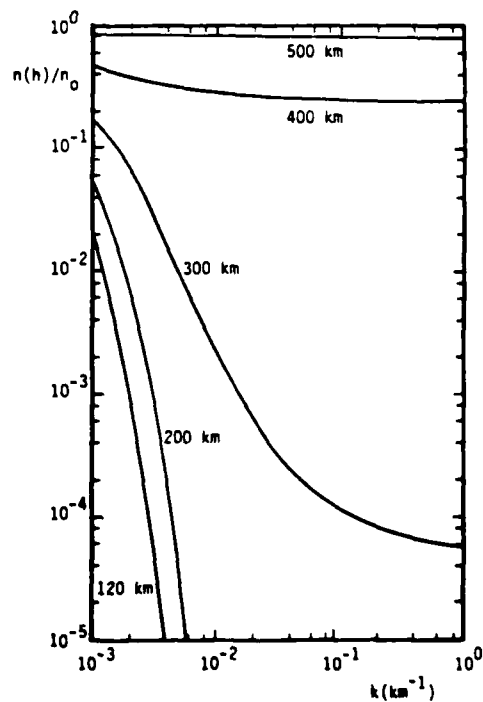
(e)



(f)



(g)



(h)

Figure 1.4. Continued (Sheet 3 of 5)

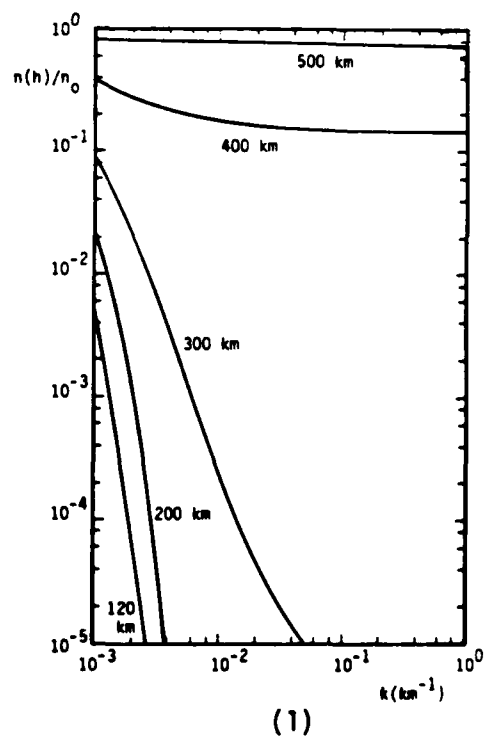
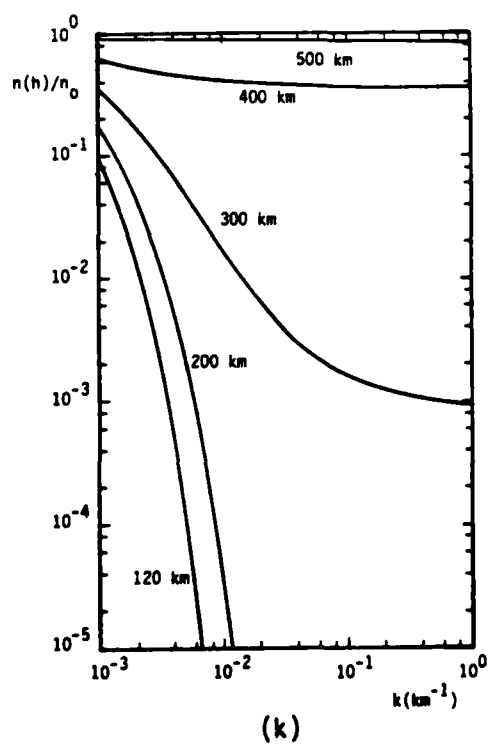
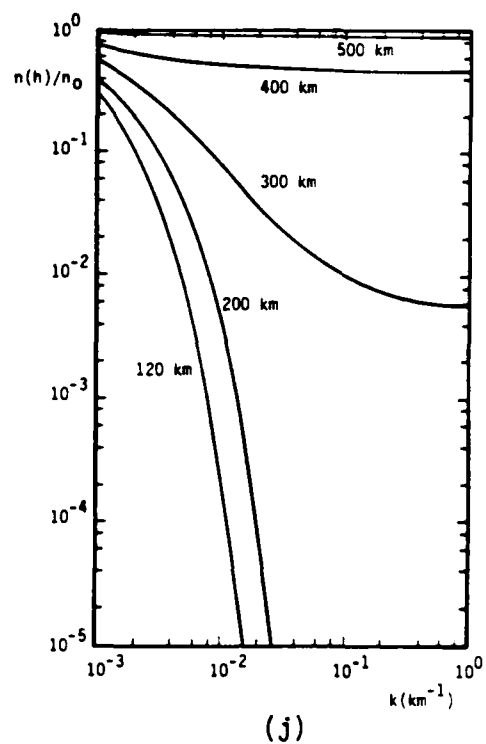
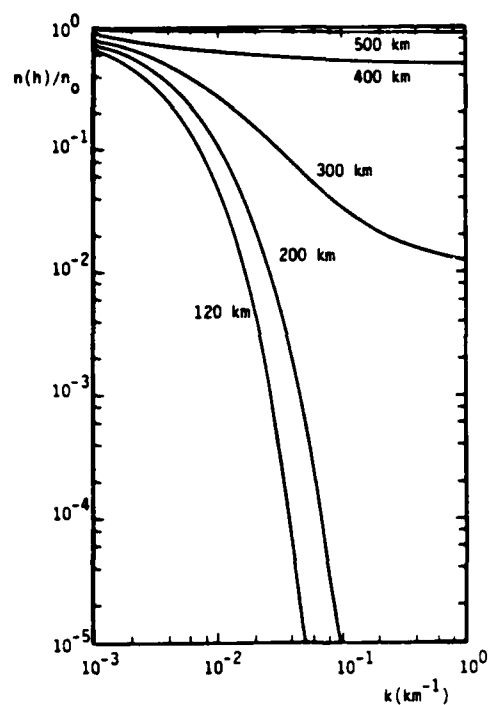


Figure 1.4. Continued (Sheet 4 of 5)

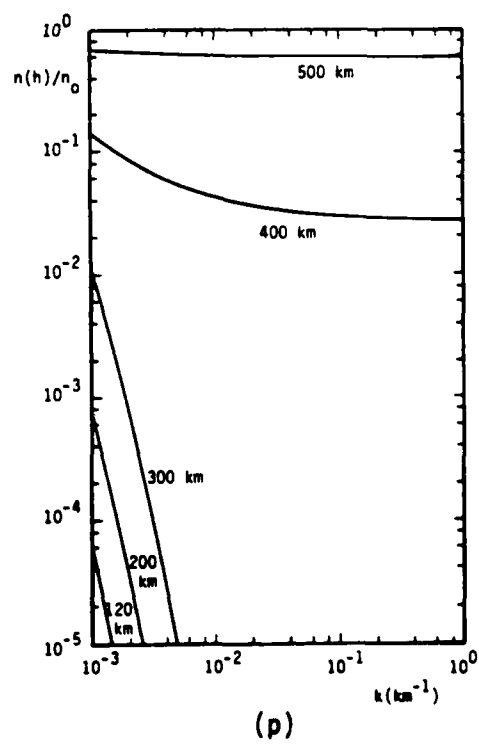
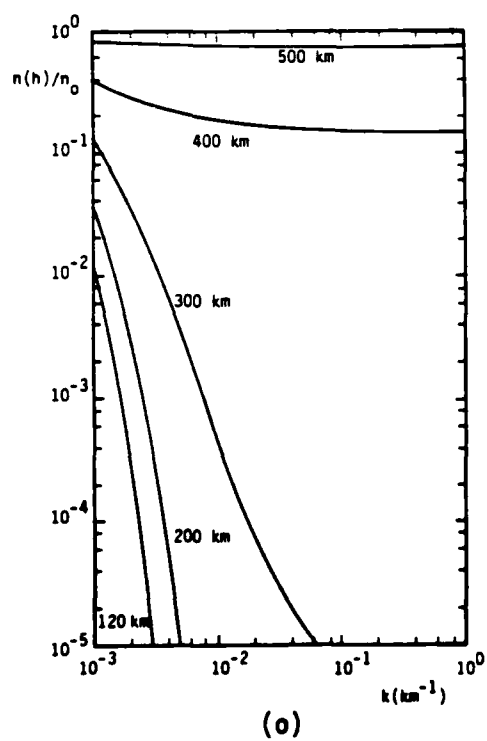
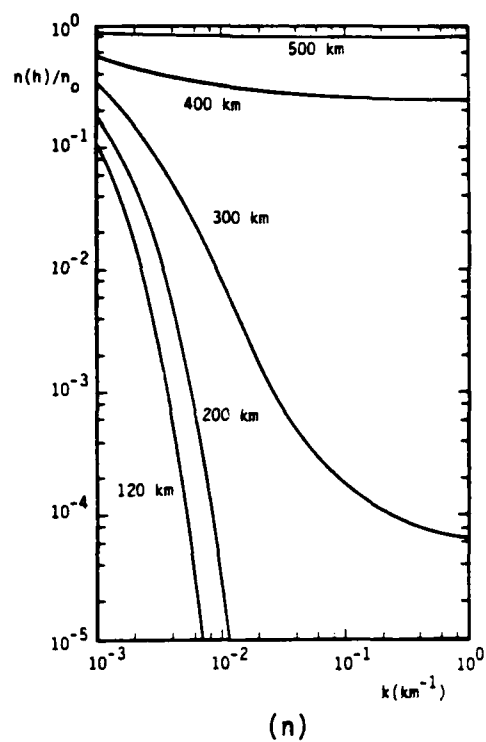
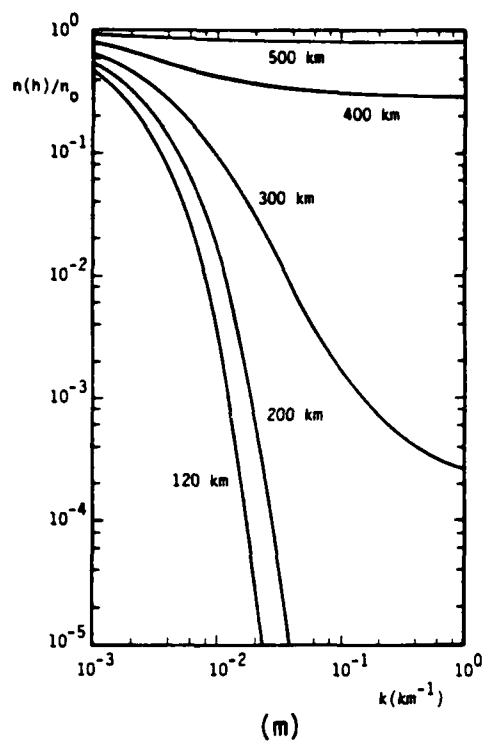
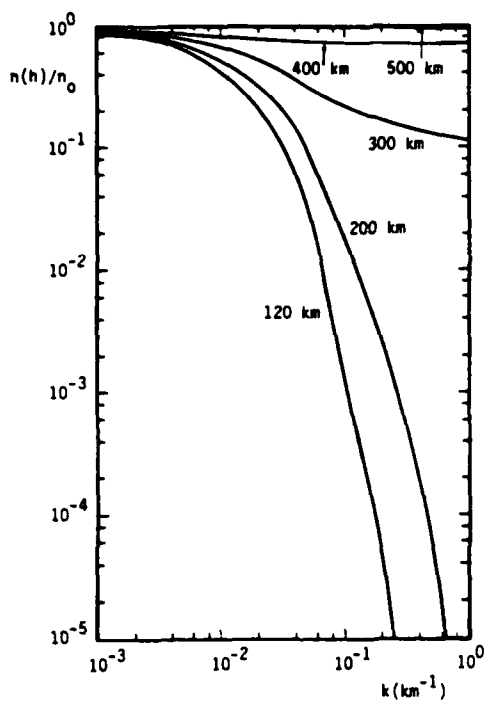


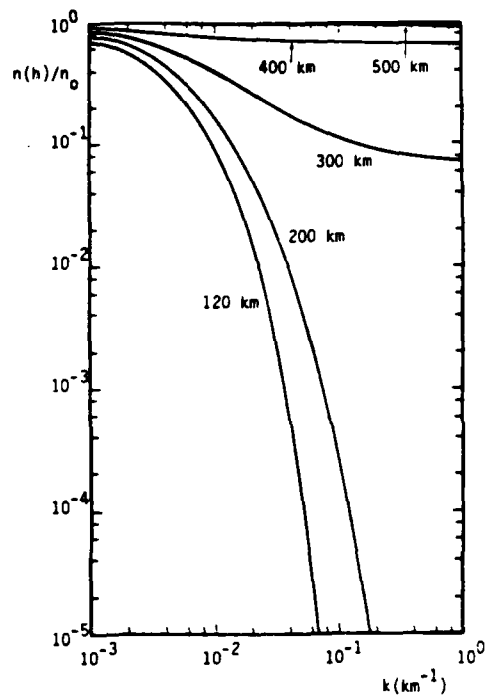
Figure 1.4. Continued (Sheet 5 of 5)

Figure 1.5. $n(h)/n_0$ versus $k(\text{km}^{-1})$ for singly ionized monatomic oxygen ions with a speed of 1×10^3 km/s. The CIRA 1972 reference atmosphere for an exospheric temperature of 900°K is used. The various curves from top to bottom correspond to altitudes of 500 km, 400 km, 300 km, 200 km, and 120 km. The initial altitude of the ions is $h = 600$ km. (Sheet 1 of 5)

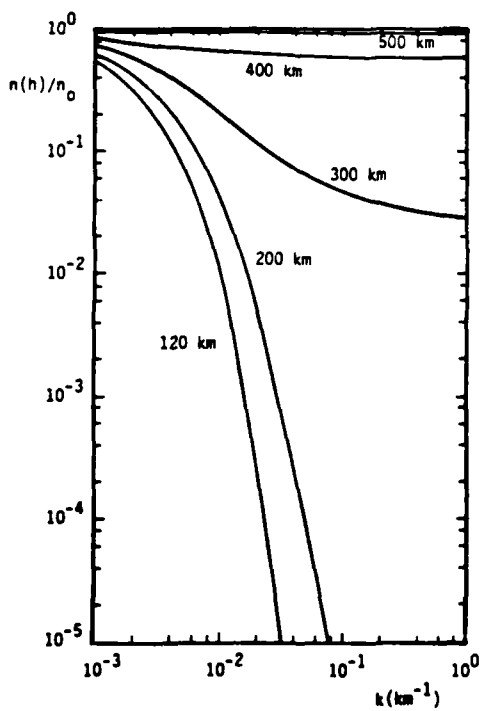
- (a) $\theta_1 = \pi/18$, $\theta_2 = \pi/18$
- (b) $\theta_1 = \pi/18$, $\theta_2 = \pi/6$
- (c) $\theta_1 = \pi/18$, $\theta_2 = 5\pi/18$
- (d) $\theta_1 = \pi/18$, $\theta_2 = 7\pi/18$
- (e) $\theta_1 = \pi/6$, $\theta_2 = \pi/18$
- (f) $\theta_1 = \pi/6$, $\theta_2 = \pi/6$
- (g) $\theta_1 = \pi/6$, $\theta_2 = 5\pi/18$
- (h) $\theta_1 = \pi/6$, $\theta_2 = 7\pi/18$
- (i) $\theta_1 = 5\pi/18$, $\theta_2 = \pi/18$
- (j) $\theta_1 = 5\pi/18$, $\theta_2 = \pi/6$
- (k) $\theta_1 = 5\pi/18$, $\theta_2 = 5\pi/18$
- (l) $\theta_1 = 5\pi/18$, $\theta_2 = 7\pi/18$
- (m) $\theta_1 = 7\pi/18$, $\theta_2 = \pi/18$
- (n) $\theta_1 = 7\pi/18$, $\theta_2 = \pi/6$
- (o) $\theta_1 = 7\pi/18$, $\theta_2 = 5\pi/18$
- (p) $\theta_1 = 7\pi/18$, $\theta_2 = 7\pi/18$



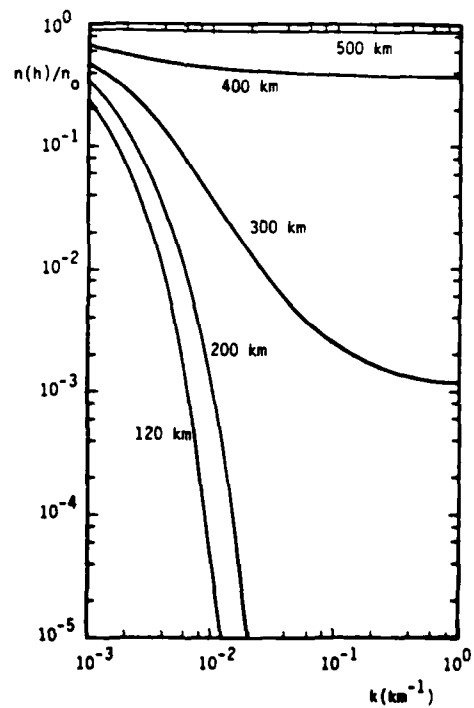
(a)



(b)

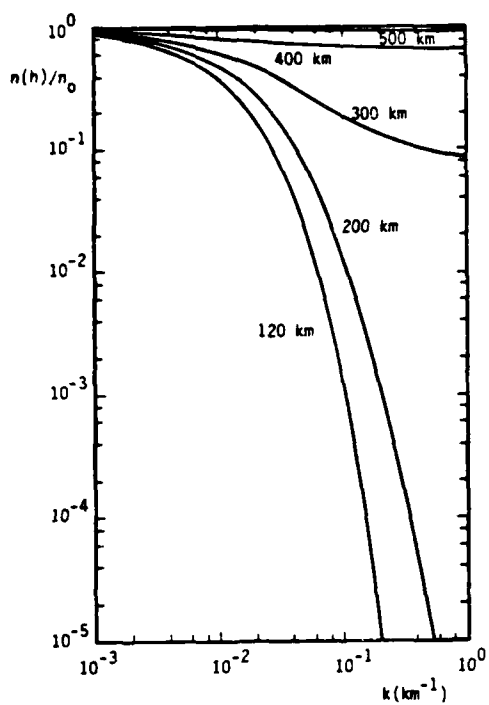


(c)

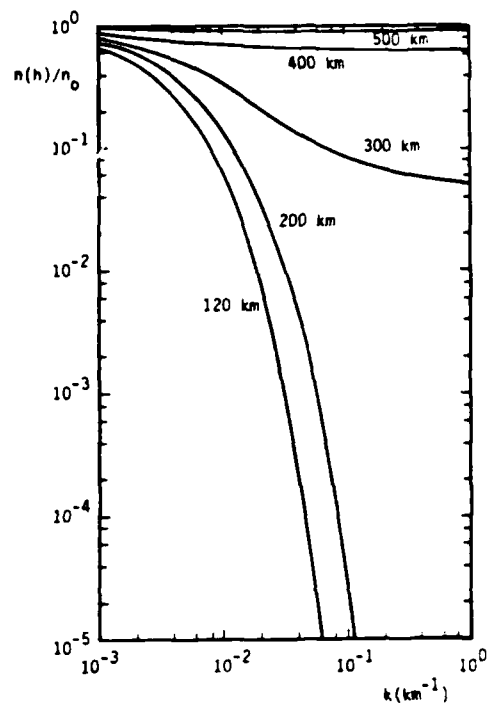


(d)

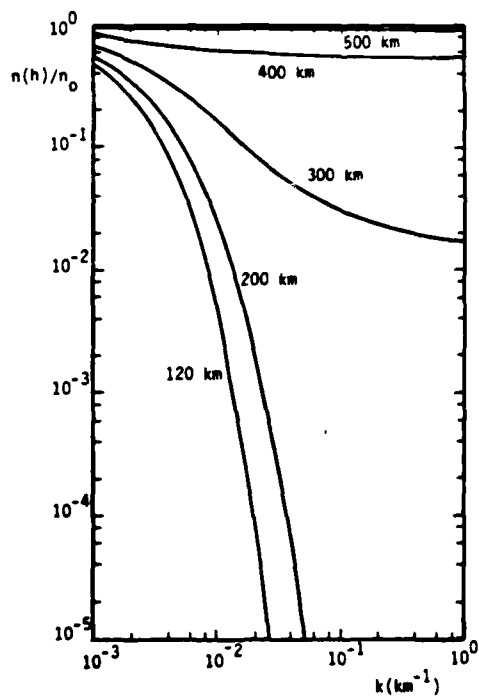
Figure 1.5. Continued (Sheet 2 of 5)



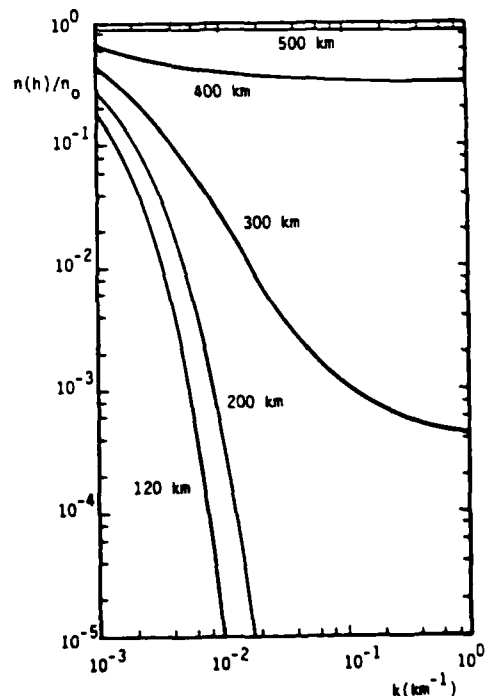
(e)



(f)

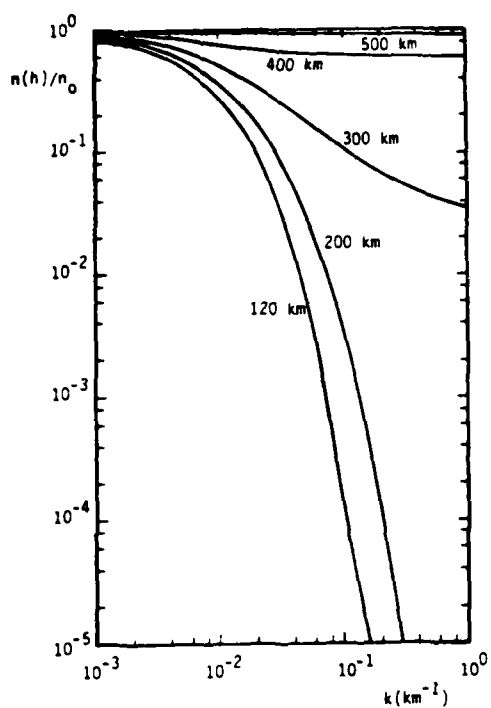


(g)

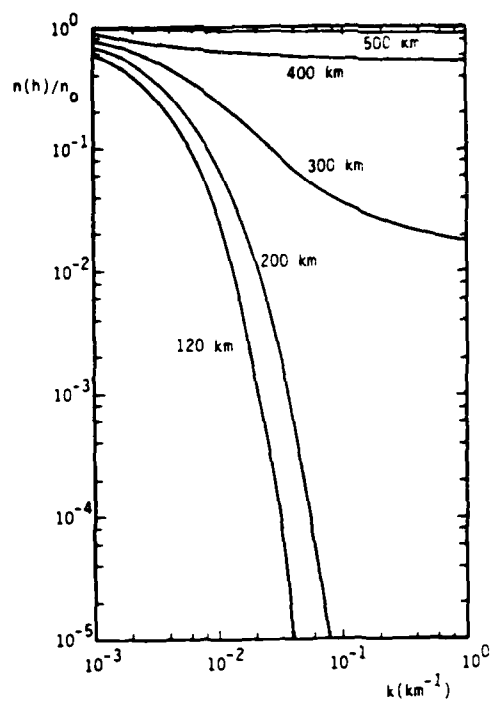


(h)

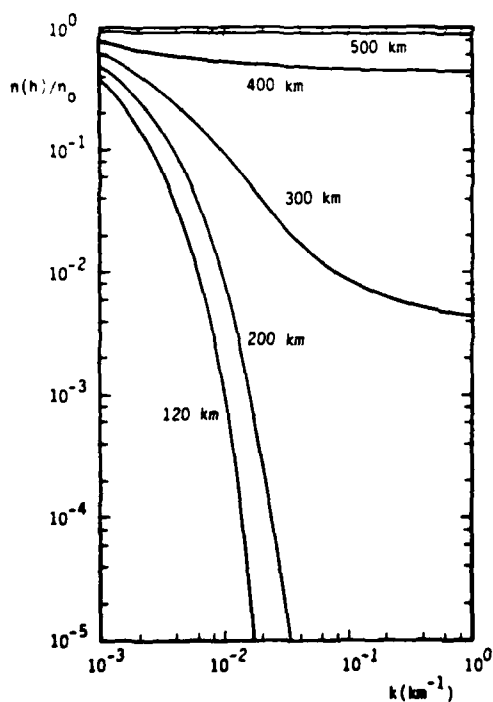
Figure 1.5. Continued (Sheet 3 of 5)



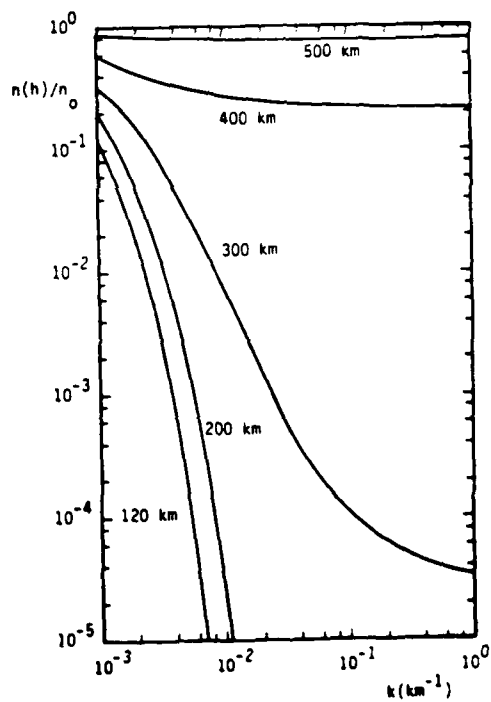
(i)



(j)



(k)



(l)

Figure 1.5. Continued (Sheet 4 of 5)

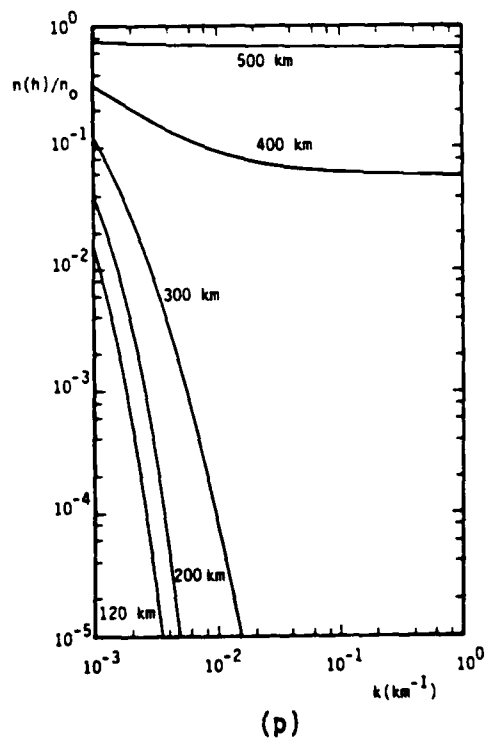
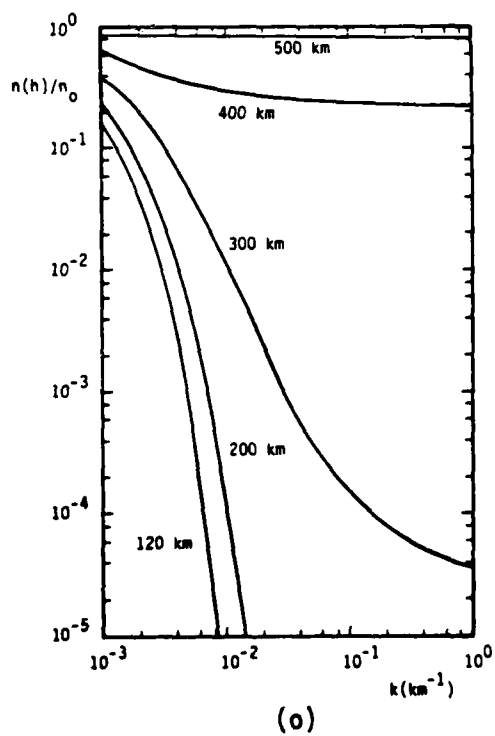
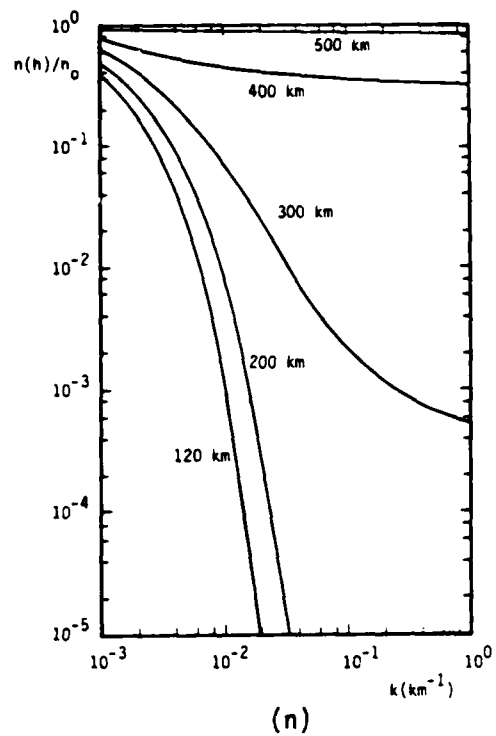
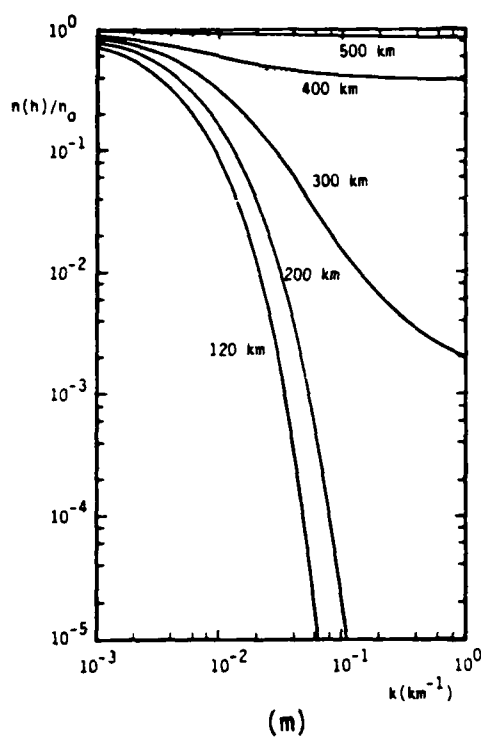
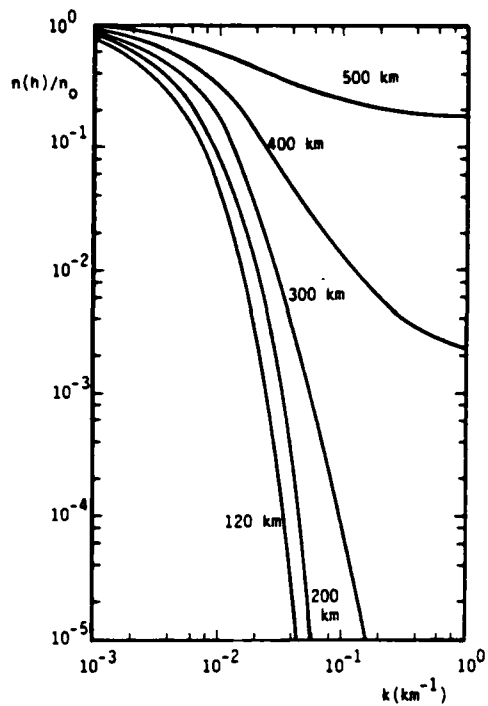


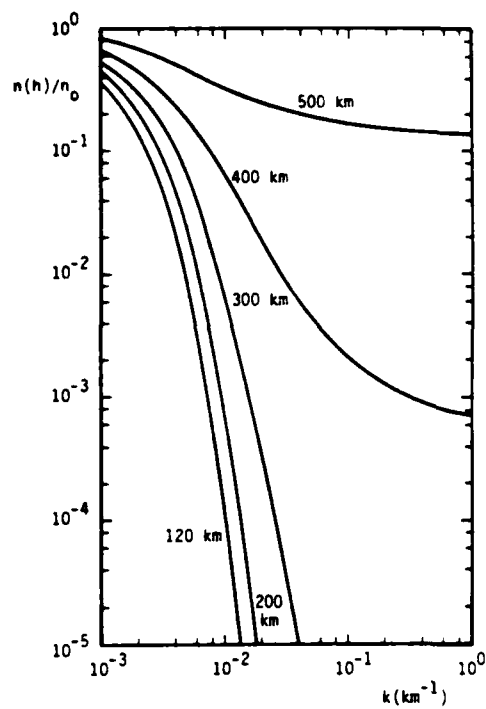
Figure 1.5. Continued (Sheet 5 of 5)

Figure 1.6. $n(h)/n_0$ versus $k(\text{km}^{-1})$ for singly ionized monatomic oxygen ions with a speed of 5×10^2 km/s. The CIRA 1972 reference atmosphere for an exospheric temperature of 1800°K is used. The various curves from top to bottom correspond to altitudes of 500 km, 400 km, 300 km, 200 km, and 120 km. The initial altitude of the ions is $h = 600$ km. (Sheet 1 of 5)

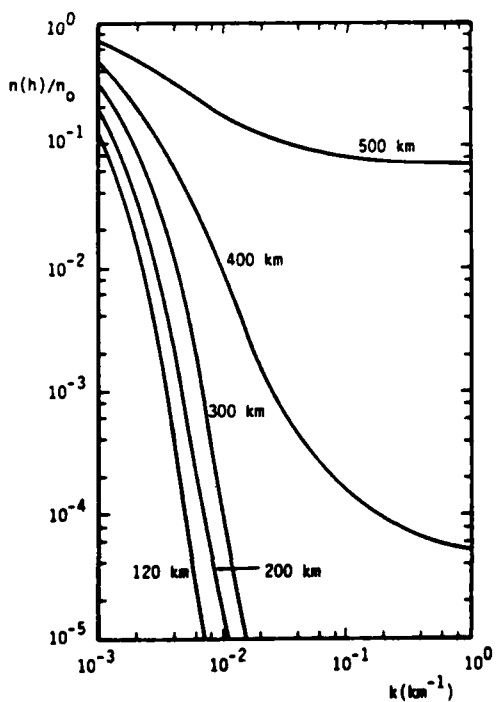
- (a) $\theta_1 = \pi/18$, $\theta_2 = \pi/18$
- (b) $\theta_1 = \pi/18$, $\theta_2 = \pi/6$
- (c) $\theta_1 = \pi/18$, $\theta_2 = 5\pi/18$
- (d) $\theta_1 = \pi/18$, $\theta_2 = 7\pi/18$
- (e) $\theta_1 = \pi/6$, $\theta_2 = \pi/18$
- (f) $\theta_1 = \pi/6$, $\theta_2 = \pi/6$
- (g) $\theta_1 = \pi/6$, $\theta_2 = 5\pi/18$
- (h) $\theta_1 = \pi/6$, $\theta_2 = 7\pi/18$
- (i) $\theta_1 = 5\pi/18$, $\theta_2 = \pi/18$
- (j) $\theta_1 = 5\pi/18$, $\theta_2 = \pi/6$
- (k) $\theta_1 = 5\pi/18$, $\theta_2 = 5\pi/18$
- (l) $\theta_1 = 5\pi/18$, $\theta_2 = 7\pi/18$
- (m) $\theta_1 = 7\pi/18$, $\theta_2 = \pi/18$
- (n) $\theta_1 = 7\pi/18$, $\theta_2 = \pi/6$
- (o) $\theta_1 = 7\pi/18$, $\theta_2 = 5\pi/18$
- (p) $\theta_1 = 7\pi/18$, $\theta_2 = 7\pi/18$



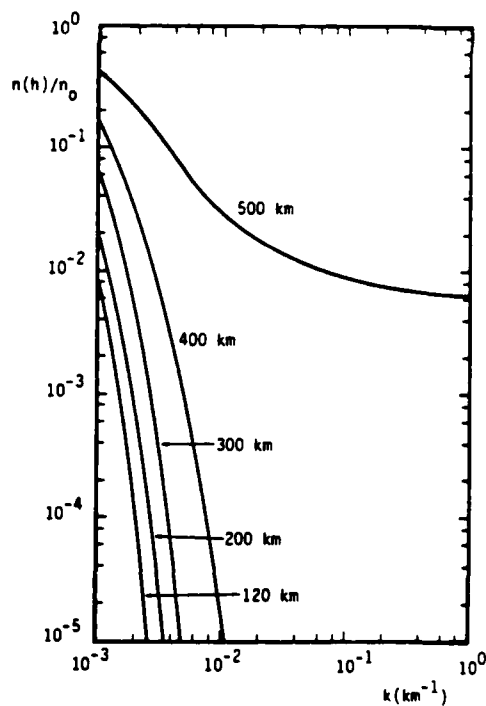
(a)



(b)

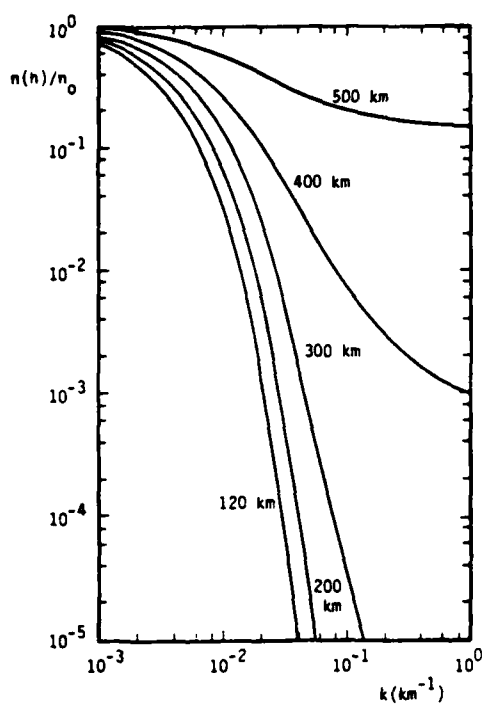


(c)

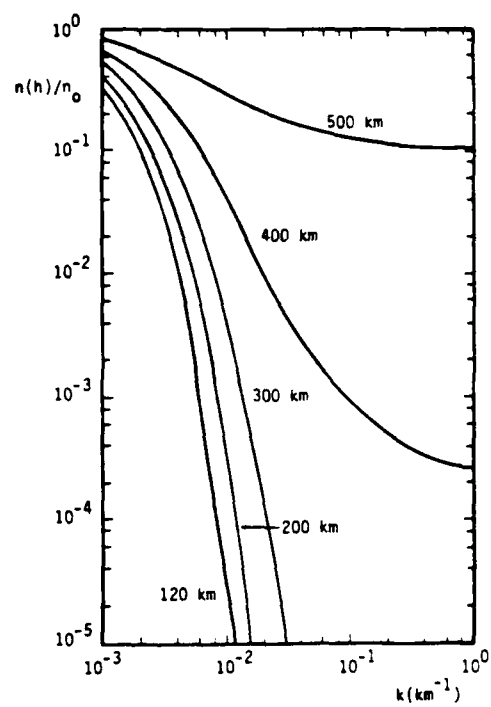


(d)

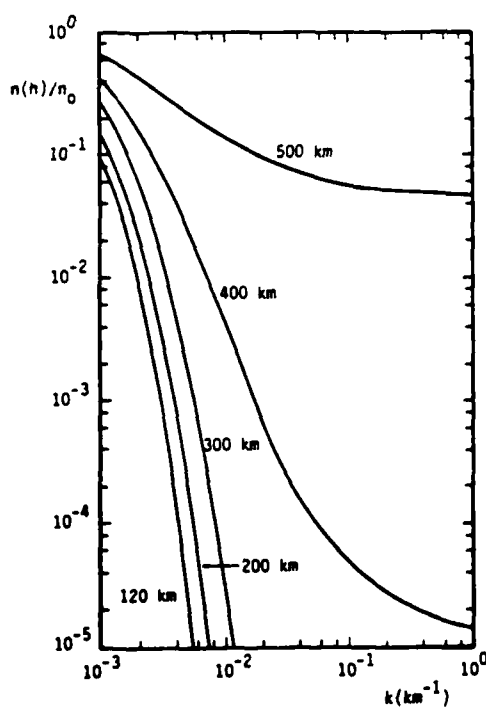
Figure 1.6. Continued (Sheet 2 of 5)



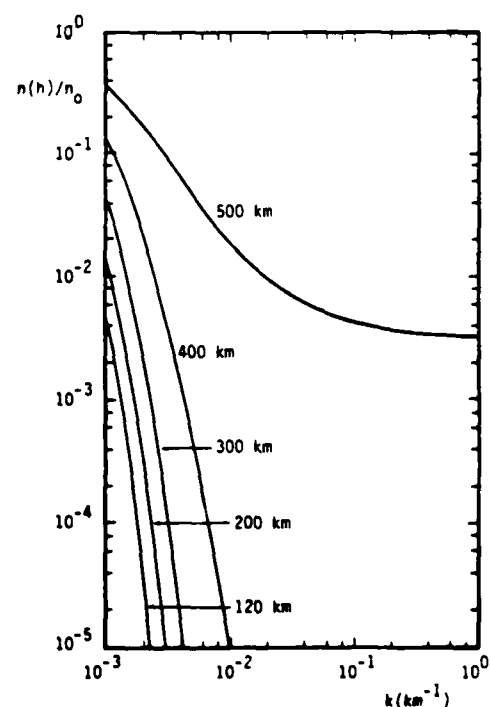
(e)



(f)

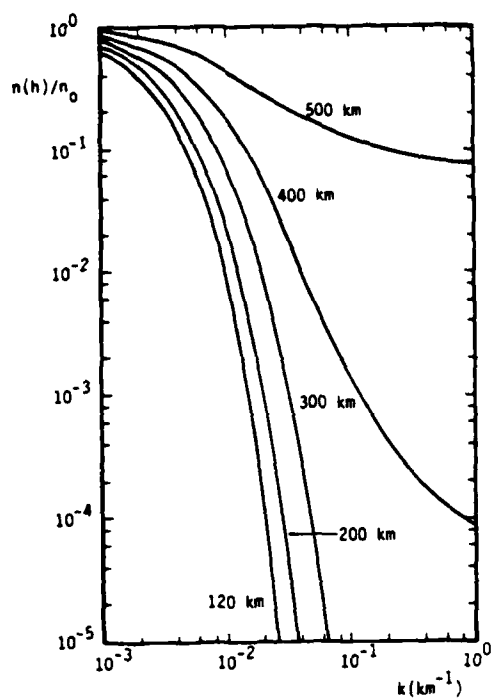


(g)

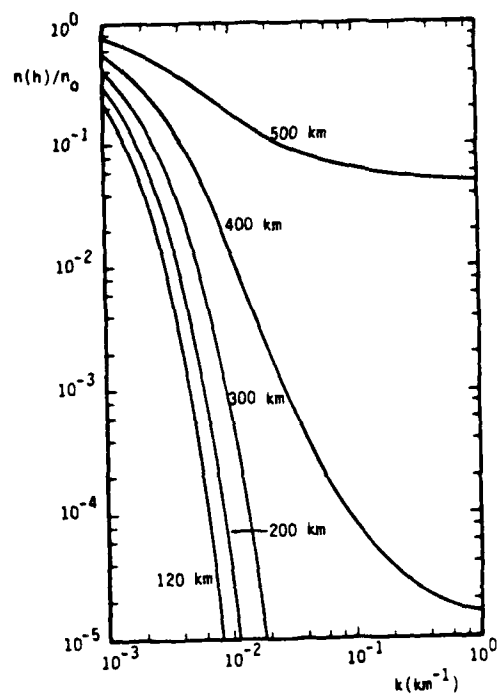


(h)

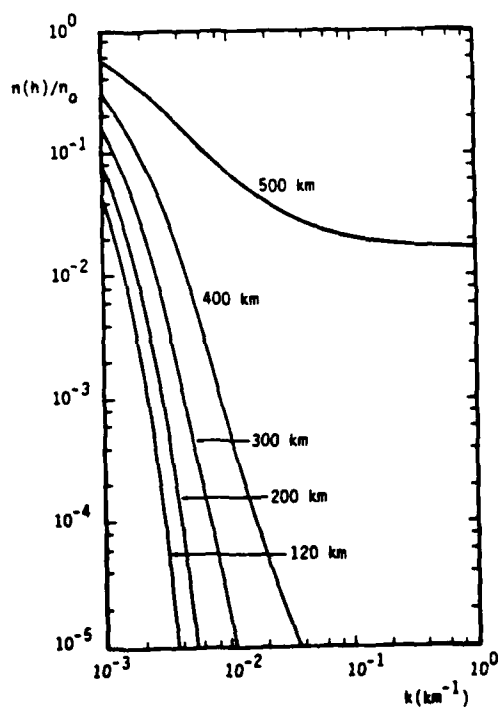
Figure 1.6. Continued (Sheet 3 of 5)



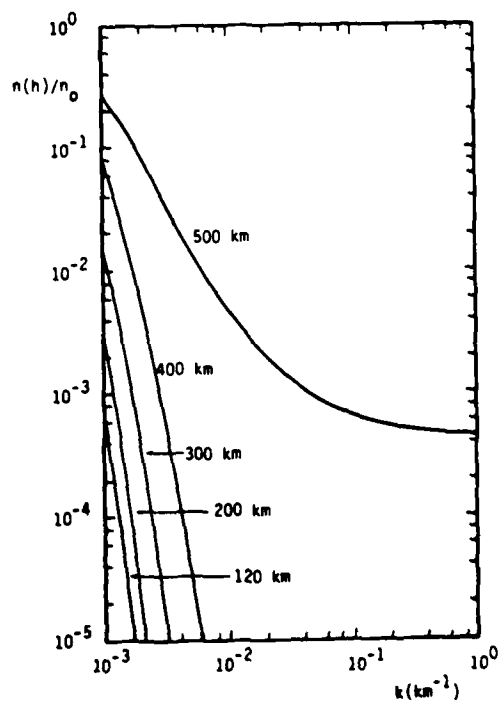
(i)



(j)



(k)



(l)

Figure 1.6. Continued (Sheet 4 of 5)

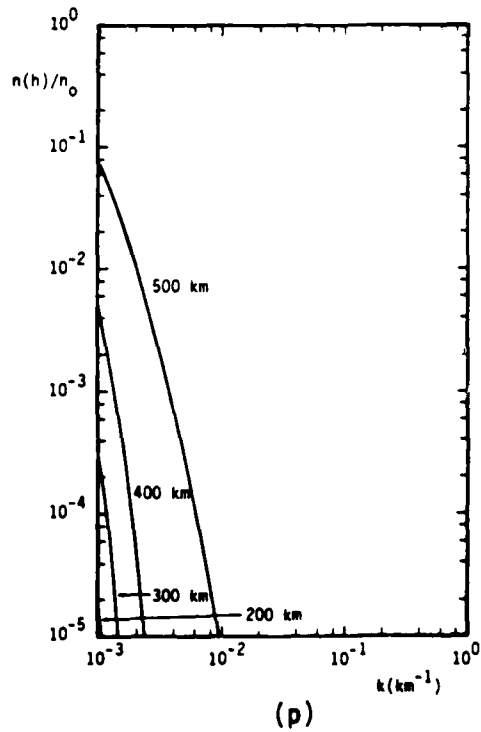
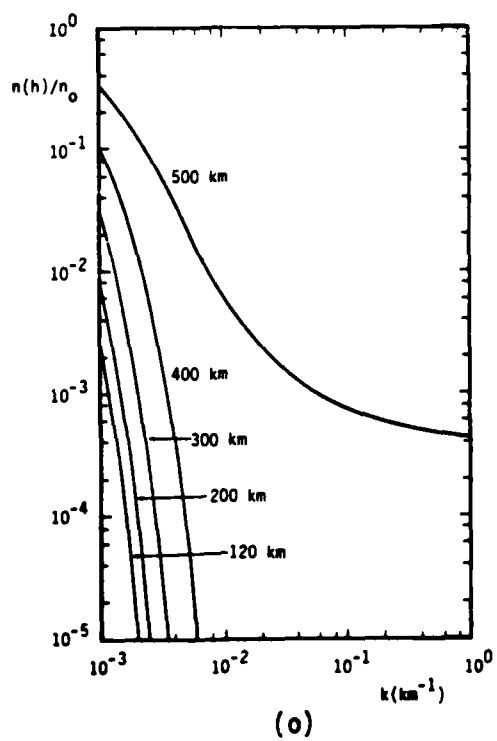
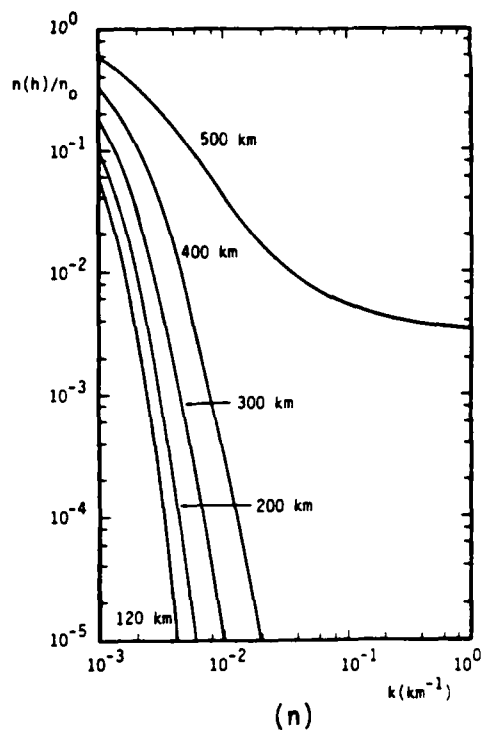
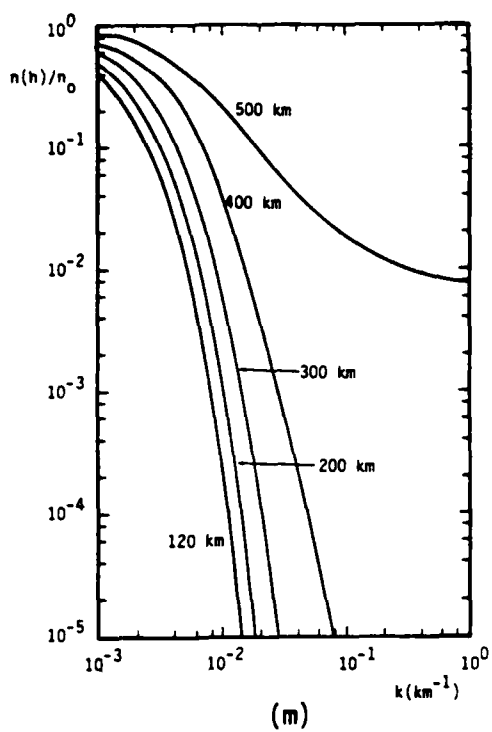
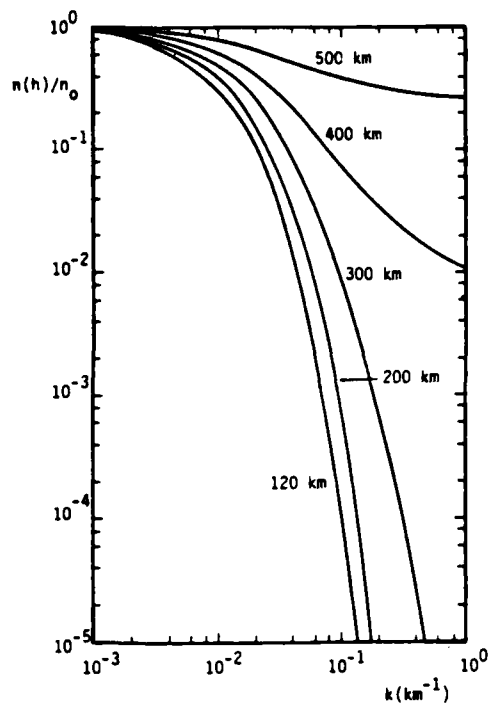


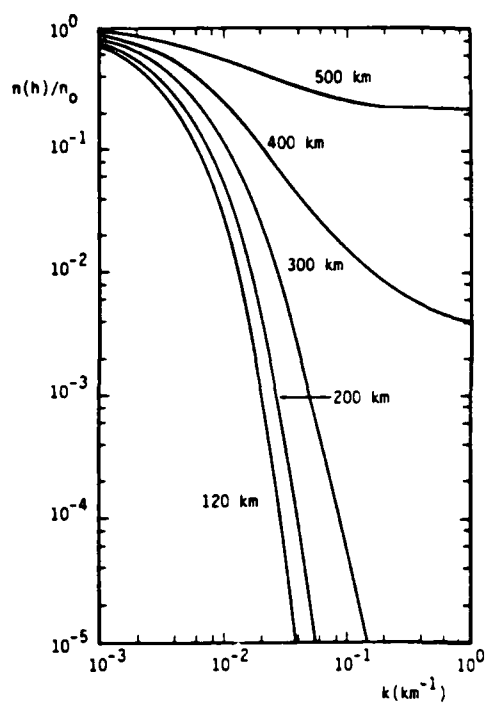
Figure 1.6. Continued (Sheet 5 of 5)

Figure 1.7. $n(h)/n_0$ versus $k(\text{km}^{-1})$ for singly ionized monatomic oxygen ions with a speed of 1×10^3 km/s. The CIRA 1972 reference atmosphere for an exospheric temperature of 1800°K is used. The various curves from top to bottom correspond to altitudes of 500 km, 400 km, 300 km, 200 km, and 120 km. The initial altitude of the ions is $h = 600$ km. (Sheet 1 of 5)

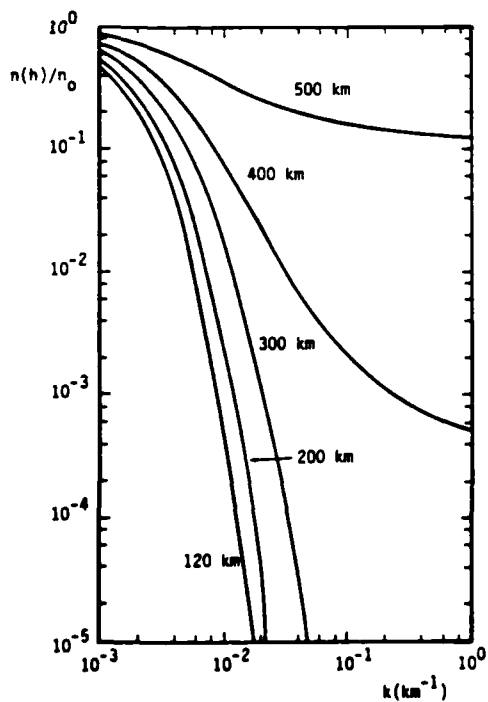
- (a) $\theta_1 = \pi/18$, $\theta_2 = \pi/18$
- (b) $\theta_1 = \pi/18$, $\theta_2 = \pi/6$
- (c) $\theta_1 = \pi/18$, $\theta_2 = 5\pi/18$
- (d) $\theta_1 = \pi/18$, $\theta_2 = 7\pi/18$
- (e) $\theta_1 = \pi/6$, $\theta_2 = \pi/18$
- (f) $\theta_1 = \pi/6$, $\theta_2 = \pi/6$
- (g) $\theta_1 = \pi/6$, $\theta_2 = 5\pi/18$
- (h) $\theta_1 = \pi/6$, $\theta_2 = 7\pi/18$
- (i) $\theta_1 = 5\pi/18$, $\theta_2 = \pi/18$
- (j) $\theta_1 = 5\pi/18$, $\theta_2 = \pi/6$
- (k) $\theta_1 = 5\pi/18$, $\theta_2 = 5\pi/18$
- (l) $\theta_1 = 5\pi/18$, $\theta_2 = 7\pi/18$
- (m) $\theta_1 = 7\pi/18$, $\theta_2 = \pi/18$
- (n) $\theta_1 = 7\pi/18$, $\theta_2 = \pi/6$
- (o) $\theta_1 = 7\pi/18$, $\theta_2 = 5\pi/18$
- (p) $\theta_1 = 7\pi/18$, $\theta_2 = 7\pi/18$



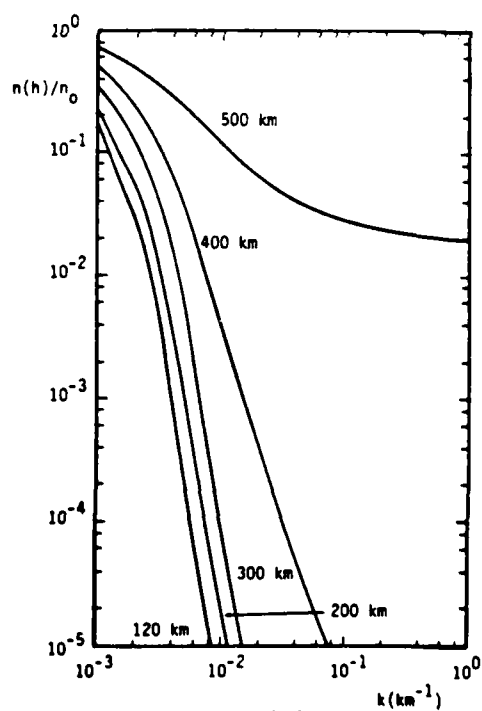
(a)



(b)

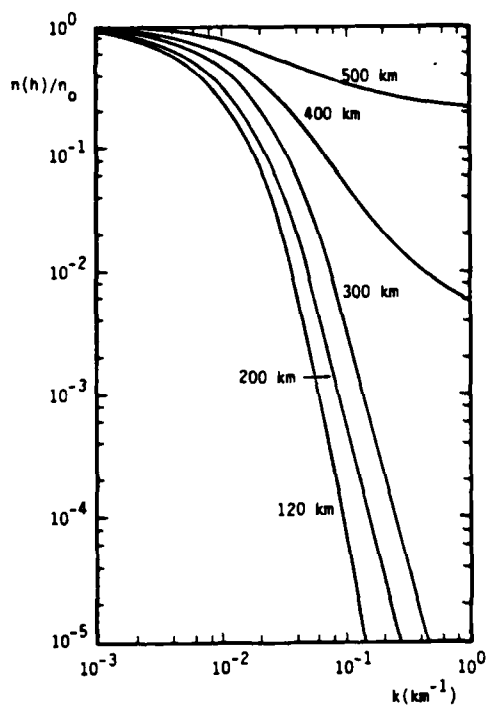


(c)

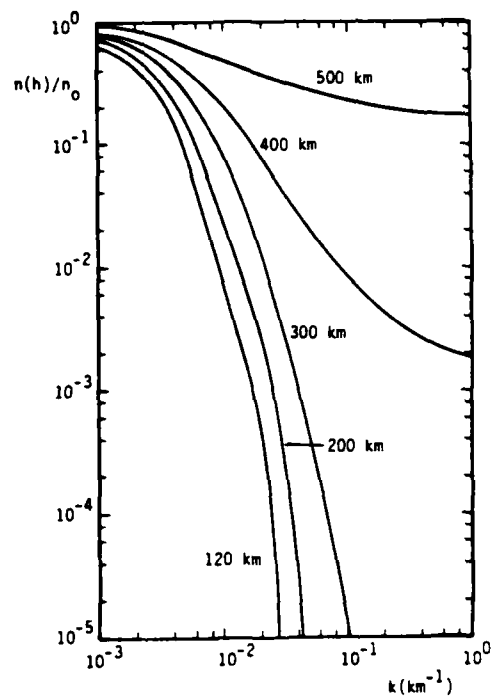


(d)

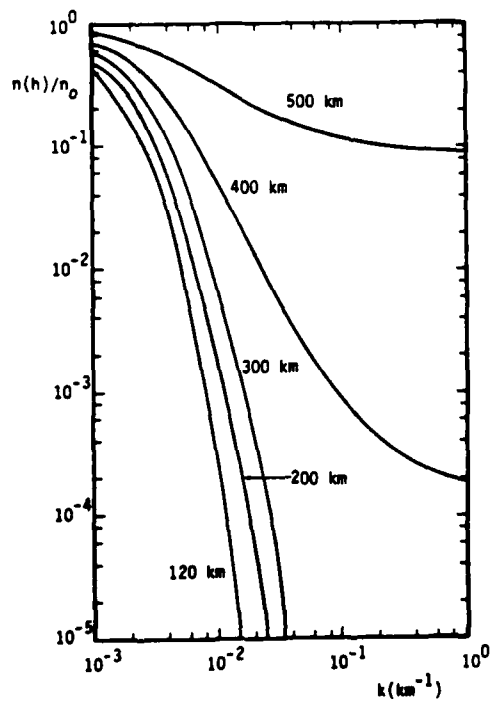
Figure 1.7. Continued (Sheet 2 of 5)



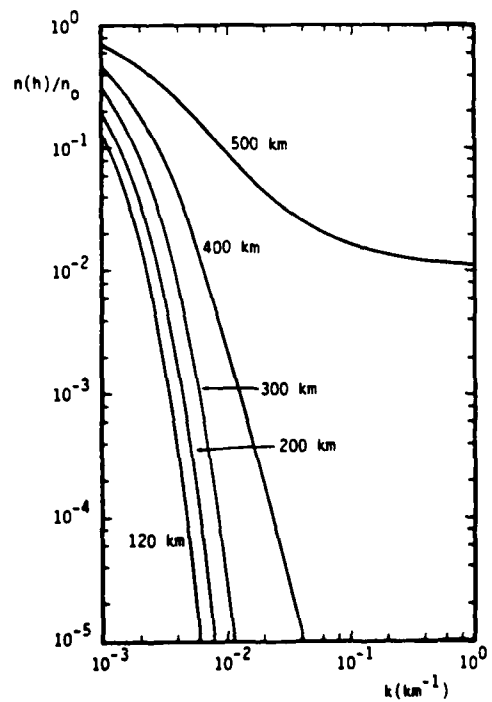
(e)



(f)



(g)



(h)

Figure 1.7. Continued (Sheet 3 of 5)

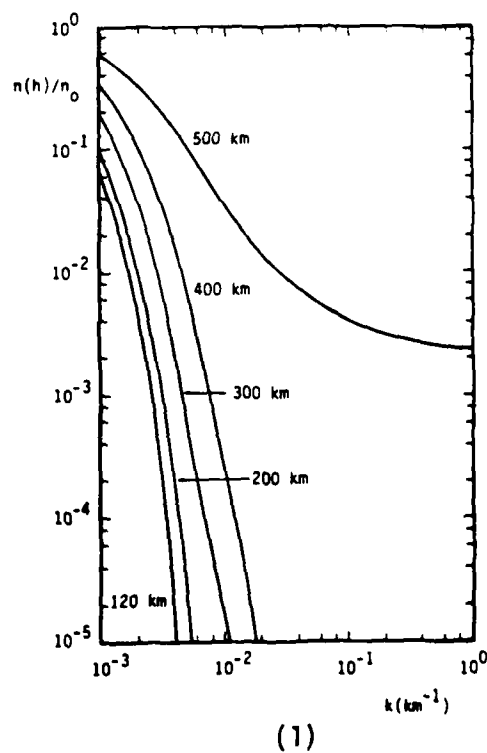
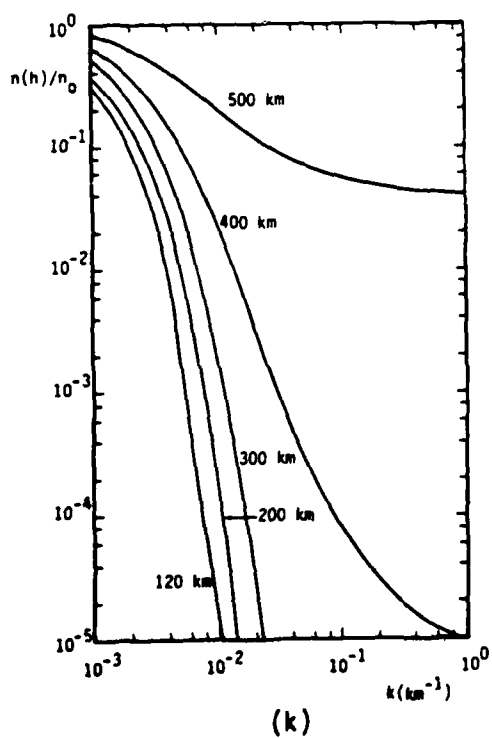
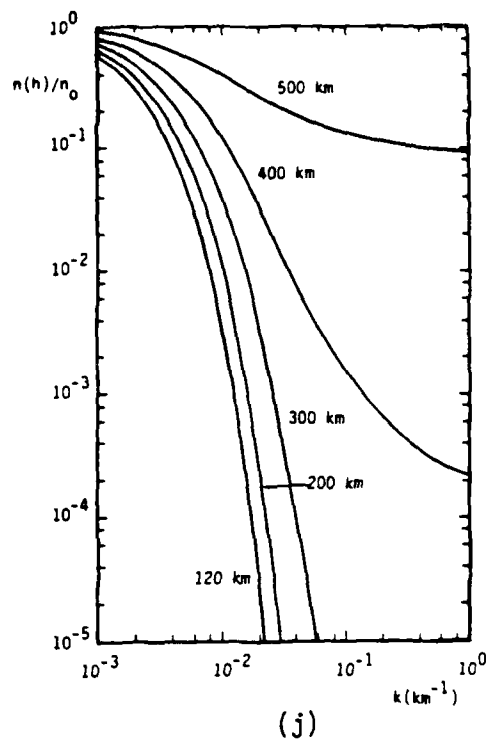
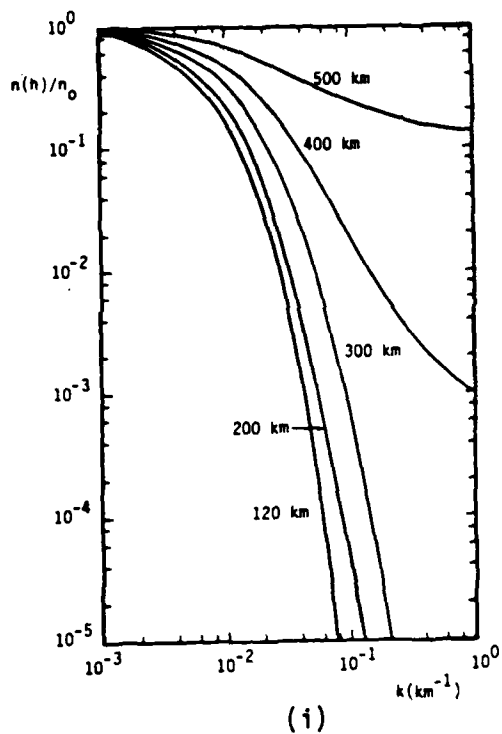


Figure 1.7. Continued (Sheet 4 of 5)

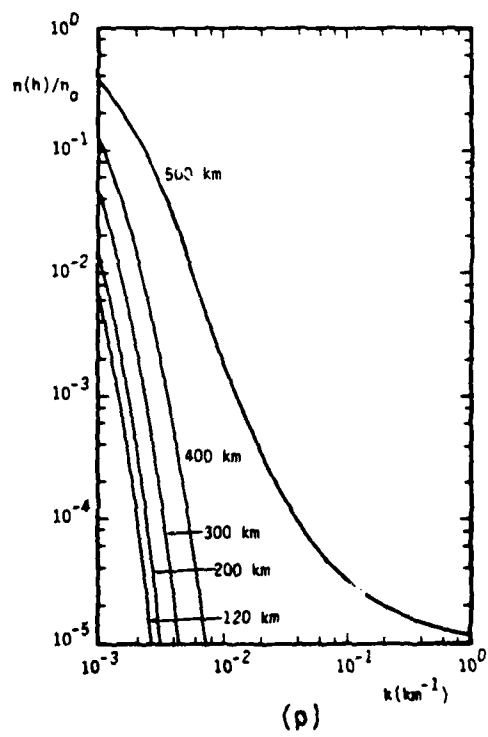
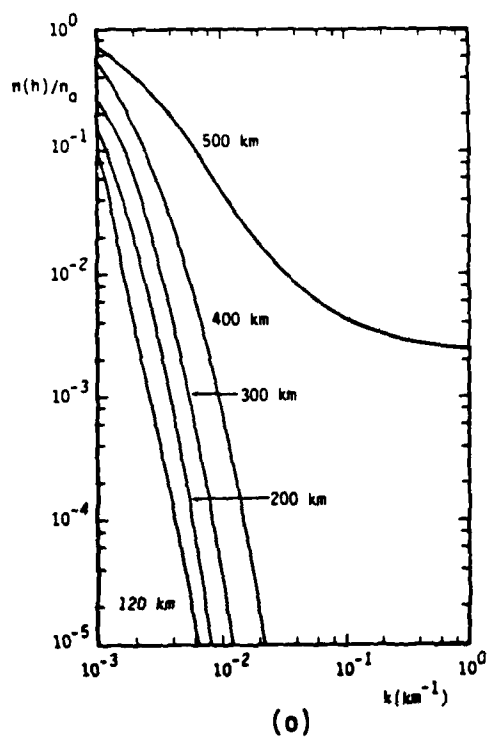
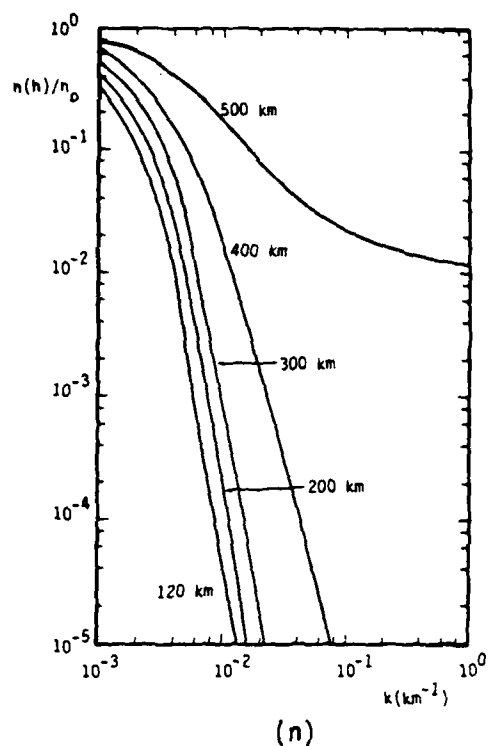
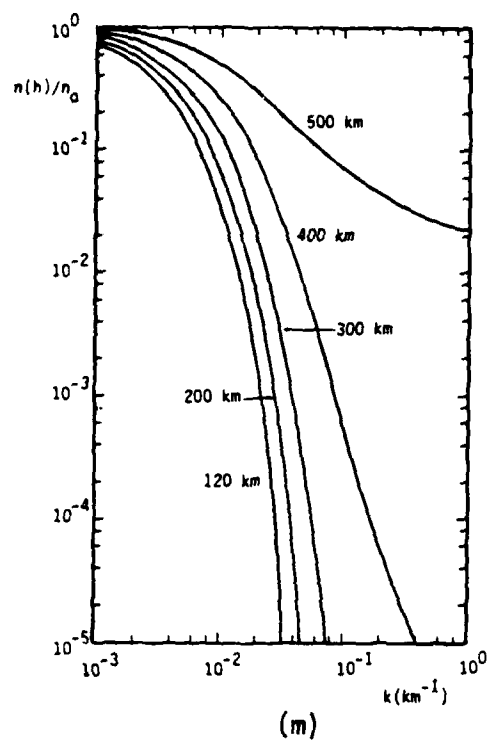


Figure 1.7. Continued (Sheet 5 of 5)

equator. Such structure, traveling along the geomagnetic field, is more likely to be subject to a charge exchange collision as it goes to a lower altitude than similar structure which forms at the geomagnetic pole. Stated another way, between two altitudes, the effective columnar density of neutrals and so the probability for charge exchange, is larger if the structure originates nearer to the geomagnetic equator rather than nearer to the geomagnetic pole.

The probability that structure persists to lower altitude is also decreased if the ion pitch angle approaches $\pi/2$. Two factors contribute to this result. First, particles with larger pitch angle must contend with an effectively larger columnar density of neutrals as they spiral down to lower altitudes. Second, energetic neutrals formed by charge exchange are more likely to leave the structure before they undergo an impact ionization collision if the ion pitch angle approaches $\pi/2$. This second factor is the reason why, for a_1 and a_2 constants, the decay for $\theta_1 = a_1$ and $\theta_2 = a_2$ with $a_2 > a_1$ generally results in larger attenuation than if $\theta_1 = a_2$ and $\theta_2 = a_1$.

Figures 1.4-1.5 use a CIRA 1972 900⁰K exospheric temperature table for the neutral atmosphere, while Figures 1.6-1.7 use the 1800⁰K table. The curves in the figures reflect the lower neutral density which occurs at a specific altitude if the exospheric temperature is smaller. Specifically, structure, especially if its transverse size is smaller than the effective fast neutral mean free path, persists to a lower altitude for lower exospheric temperatures.

It is evident from Figures 1.4-1.7 that the combination of charge exchange and impact ionization collisions preferentially destroys fine scale structure superimposed on large scale structure. The result is a shift of the wavenumber spectrum to scale sizes which are comparable to or larger than the mean free path for impact ionization.

Consider a hypothetical structure initially consisting of energetic ions at an altitude above 400 km. It is evident from the various curves in Figures 1.4-1.7 that the wavenumber greater than 0.1 km components of this structure are attenuated by at least two orders of magnitude as they travel down to altitudes below roughly 200 km where the energetic ions deposit their energy, partially by ionization of the neutral ionosphere. At these altitudes, fluid mechanisms like the EXB gradient drift instability can cause fluid structuring. The corresponding outer scale length of the power spectral density is likely larger than 10 km based on recent

fluid simulations of EXB structuring. These simulations suggest that density perturbations smaller than 15 percent (superimposed on a larger density profile) do not determine the long-term outer scale.^{1.3}

The outer scale length associated with energetic ionic structure convecting down field lines is at least 10 km, a length which is larger than the expected gyroradii of monatomic oxygen ions. Hence, structures similar to prompt striations with a scale size comparable to or smaller than the ion-gyroradius^{1.4-1.6} and originating at higher altitudes (i.e., ≥ 400 km), do not impose the long-term outer scale length at lower altitudes by propagation down magnetic field lines. Indeed, Figures 1.4-1.7 suggest that structure consisting of energetic ions may set an outer scale length larger than 100 kilometers at lower altitudes, especially if the structure originates near the magnetic equator and initially consists of ions with large pitch angles.

1.4 CONCLUDING REMARKS

Charge exchange collisions can convert ions into neutrals, whose trajectories are unaffected by the magnetic field to lowest order. As a result, structure consisting initially of energetic ions can decay at a more rapid rate than classical, cross-field, ion diffusion implicates. This decay of structure is convective or diffusive depending on whether the effective neutral mean free path for impact ionization is larger or smaller than the structural size transverse to the magnetic field. The degradation of structure is most significant when particle loss is convective and particles do not become reionized within the confines of the original structural boundaries.

It has been demonstrated that structures, consisting of energetic (in particular monatomic oxygen) particles and having a scale size transverse to the magnetic field which is smaller than or comparable to 10 kilometers, are attenuated by at least two orders of magnitude as they travel down field lines from altitudes of approximately 400 to 600 kilometers down to altitudes of 100 to 200 kilometers. Because recent fluid simulations suggest that density perturbations comparable to or less than 15 percent, on a larger density profile, do not determine the long-term outer scale of the power spectral density,^{1.3} it seems likely that the propagation of the structure from higher to lower altitudes imposes an outer scale length at least as large as 10 kilometers at the lower altitudes. Origination near

the magnetic equator and particle pitch angles approaching 90 degrees suggest even larger outer scale lengths (i.e., ≥ 100 km). Structures, like prompt striations, which form at higher altitudes (i.e., ≥ 400 km)^{1.5-1.6} and have scale sizes perpendicular to the magnetic field comparable to or smaller than the ion-gyroradius, evidently do not impose the long-term outer scale length at lower altitudes by propagating down magnetic field lines.

REFERENCES

- 1.1 W. L. Fite, J. S. Greene, Jr., A. W. Ali, and I. M. Pikus, "Kinetics of High-Energy Heavy-Particle Collisional Process," in Defense Nuclear Agency Reaction Rate Handbook, DNA 1948H, M. H. Bortner and T. Baurer, Eds., General Electric Company, Philadelphia, PA, ch. 15, 1979.
- 1.2 S. R. Goldman and J. L. Sperling, "Some Physical and Chemical Aspects of Striation Structure," J510-80-023/2128-02, JAYCOR, San Diego, CA, 1980.
- 1.3 M. J. Keskinen and S. L. Ossakow, "Effects of Different Initial Conditions on the Evolution of the E X B Gradient Drift Instability in Ionospheric Clouds," NRL Memorandum Report 4490, Naval Research Laboratory, Washington, D.C., 1981.
- 1.4 D. J. Simons, M. B. Pongratz, and S. P. Gary, "Prompt Striations in Ionospheric Barium Clouds Due to Velocity Space Anisotropy," J. Geophys. Res., **85**, No. A2, pp. 671-677, 1980.
- 1.5 J. L. Sperling and N. A. Krall, "Stabilization of Electrostatic, Purely Growing, Finite Ion Gyroradius, Flute Instabilities in the Ionosphere," J. Geophys. Res., **86**, No. A9, pp. 7513-7518, 1981.
- 1.6 J. L. Sperling, "Electromagnetic Effects in the Analysis of Prompt Striations," J. Geophys. Res. (to be published).
- 1.7 F. W. J. Olver, "Bessel Functions of Integer Order," in Handbook of Mathematical Functions with Formulas, Graphs, and Mathematical Tables, M. Abramowitz and I. A. Stegun, Eds., U.S. Government Printing Office, Washington, D.C., ch. 9, 1970.
- 1.8 M. Abramowitz, "Struve Functions and Related Functions," in Handbook of Mathematical Functions with Formulas, Graphs, and Mathematical Tables, M. Abramowitz and I. A. Stegun, Eds., U.S. Government Printing Office, Washington, D.C., ch. 12, 1970.
- 1.9 D. Sappenfield, private communication.

2. ANALYSIS OF RADIATIVE RECOMBINATION EFFECTS ON DENSITY PROFILES AND THEIR FOURIER SPECTRUMS

2.1 INTRODUCTION

In the ionosphere, radiative recombination is an incontrovertible classical process which reduces ionization density.^{2.1-2.4} Because it requires more than one particle, a most significant feature of the recombination process is its inherent nonlinear dependence on density. Consequently, recombination alters the Fourier spectrum of density profiles and so recombination gives a lower bound to the coupling of Fourier modes. This bound may be exceeded when other plasma processes, like turbulence, are active. From the practical standpoint, the change in Fourier spectrum resulting from recombination implies an effect on communications which is in addition to ionization decay.^{2.5}

A simple model for radiative recombination is quantitatively demonstrated to cause changes in both the morphology and Fourier spectrum of model one-dimensional ionization density profiles. A key result of the analysis is the observation that the short- and long-term effects of recombination on structure are different. For the specific density profiles considered, Fourier components of the spectrum which are initially small have a general tendency to at first increase relative to the spatially uniform component. This effective mode coupling process is most evident for very cold plasmas (at least for the monatomic oxygen or nitrogen model considered here) in which the recombination process is most nonlinear. Those components of the Fourier spectrum which are initially present decay relative to the spatially uniform component. In the long-term, recombination leads to the general decay of all Fourier components, resulting from density inhomogeneity, relative to the spatially uniform component.

This chapter is divided into four sections including this Introduction. Section 2.2 describes the analytic model used for the calculations. Section 2.3 describes results from the numerical evaluation of the chemical recombination mode. Section 2.4 summarizes the major results and conclusions.

2.2 MODEL

As the basis for the model, a weakly ionized neutral plasma is assumed which consists of electrons and singly charged positive ions recombining into monatomic atoms of the same isotopic species. The evolution of electron (ion) density as a function of time, $n(t)$, is then determined from the equation^{2.1,2.2}

$$\frac{dn(t)}{dt} = -\alpha[n(t)] n^2(t) \quad . \quad (2.1)$$

In Eq. (2.1) the quantity $\alpha[n(t)]$ is permitted to be a function of density. The assumption,

$$\alpha[n(t)] \equiv \beta n(t)^\gamma \quad , \quad (2.2)$$

with β and γ nonnegative constants, permits Eq. (2.1) to be solved exactly as a function of time. Specifically,

$$n(t) = \frac{n_0}{\left[1 + (\gamma + 1) \beta t n_0^{\gamma+1}\right]^{1/(\gamma+1)}} \quad , \quad (2.3)$$

where n_0 is the initial density at $t = 0$.

By assuming that density evolution at a given spatial location depends on the value of density at that point only, it is evident that spatial variation can be included in the evolution equation through the replacement

$$n(t) \rightarrow n(\vec{x}, t) \quad , \quad n_0 \rightarrow n_0(\vec{x}) \quad , \quad (2.4)$$

where \vec{x} is the position vector. Equation (2.3) now becomes

$$n(\vec{x}, t) = \frac{n_0(\vec{x})}{\left[1 + (\gamma + 1) \beta t n_0(\vec{x})^{\gamma+1}\right]^{1/(\gamma+1)}} \quad . \quad (2.5)$$

For simplicity, it is assumed here that the density depends on one spatial coordinate only, the x -direction. Assuming an arbitrary continuous density variation which is periodic over a length $2L$ and is symmetric about $x = 0$ permits the general density profile of Eq. (2.5) to be written in terms of a Fourier series in the x -coordinate:

$$n(x,t) = \frac{a_0(t)}{(2L)^{1/2}} + \sum_{p=1}^{\infty} \frac{a_p(t)}{(L)^{1/2}} \cos\left(\frac{p\pi}{L} x\right) \quad (2.6)$$

In Eq. (2.6) the time dependent Fourier amplitudes are determined by

$$a_p(t) = \frac{2}{\{1 + [(2)^{1/2} - 1] \delta_{p,0}\} (L)^{1/2}} \int_0^L dx n(x,t) \cos\left(\frac{p\pi}{L} x\right) \quad (2.7)$$

with $\delta_{p,0}$ the Kronecker delta. It follows from Eq. (2.7) that the quantity, $(2L)^{1/2} a_0(t)$, is the total ion density between $x = -L$ and $x = +L$ at any time t and is the only Fourier amplitude present in an uniform plasma.

It is useful to examine the form of the Fourier amplitudes in two limits [i.e., $(\gamma+1) \beta t n_0(x)^{\gamma+1} \ll 1$ and $\gg 1$]. For $(\gamma+1) \beta t n_0(x)^{\gamma+1} \ll 1$ for all x , the binomial expansion permits Eq. (2.7) to be approximately written

$$a_p(t) \approx \frac{2}{\{1 + [(2)^{1/2} - 1] \delta_{p,0}\} (L)^{1/2}} \int_0^L dx n_0(x) \{1 - \beta t n_0(x)^{\gamma+1}\} \cos\left(\frac{p\pi}{L} x\right) \quad (2.8)$$

Similarly, for $(\gamma+1) \beta t n_0(x)^{\gamma+1} \gg 1$ for all x ,

$$a_p(t) \approx \frac{2}{\{1 + [(2)^{1/2} - 1] \delta_{p,0}\} (L)^{1/2}} \int_0^L dx \frac{\cos(p\pi x/L)}{[(\gamma+1) \beta t]^{1/(\gamma+1)}} \left[1 - \frac{1/(\gamma+1)^2}{\beta t n_0(x)^{\gamma+1}}\right] \quad (2.9)$$

Equation (2.9) implies that,

$$a_0(t) \approx \frac{(2L)^{1/2}}{[(\gamma+1) \beta t]^{1/(\gamma+1)}} \quad (2.10a)$$

and

$$a_{p \neq 0} \approx - \frac{2}{(L)^{1/2}} \frac{1/(\gamma+1)^{(2\gamma+3)/(\gamma+1)}}{(\beta t)^{(\gamma+2)/(\gamma+1)}} \int_0^L dx \frac{\cos(p\pi x/L)}{n_0(x)^{\gamma+1}} \quad (2.10b)$$

Explicit quantitative temporal and spatial evaluation of the density profile when recombination is active requires specific values for the parameters, β and γ . In this paper it is assumed that the ion and neutral species are monatomic nitrogen or oxygen. The particular exothermic reactions considered are:



where N^+ , e^- , N , O^+ , and O represent a positive nitrogen ion, an electron, a neutral nitrogen particle, a positive oxygen ion, and a neutral oxygen particle, respectively. For the reactions specified by Eq. (2.11), the values of $\alpha(n)$ in Eq. (2.1) are tabulated in Table 2.1 for different densities and for electron temperatures, T_e , of 0.043 eV and 0.518 eV, respectively.^{2,6} A linear regression analysis for $\ln[\alpha(n)]$ gives

$$T_e = 0.043 \text{ eV} \quad , \quad \beta \approx 4.433 \times 10^{-17} \quad , \quad \gamma \approx 0.6689 \quad (2.12a)$$

$$T_e = 0.518 \text{ eV} \quad , \quad \beta \approx 1.202 \times 10^{-13} \quad , \quad \gamma \approx 0.04565 \quad (2.12b)$$

with β in cgs units. Clearly, the recombination coefficient $\alpha(n)$ is more sensitively dependent on density for lower temperatures than for higher temperatures.

2.3 EXAMPLES

To demonstrate the quantitative decay of ionized density structure as a function of time, four different initial density profiles are considered:

$$n_0(x) = N[1 - 0.3 (x/L)] \quad , \quad (2.13a)$$

$$= N[1 - 0.7 (x/L)] \quad , \quad (2.13b)$$

$$= N\{1 + 0.1 [\cos(4\pi x/L) + \cos(5\pi x/L)]\} \quad , \quad (2.13c)$$

$$= N\{1 + 0.3 [\cos(4\pi x/L) + \cos(5\pi x/L)]\} \quad . \quad (2.13d)$$

Table 2.1. Values of $\alpha(n)$ in units of cm^3/s for various densities and electron temperatures, T_e , of 0.043 eV and 0.518 eV

| $T_e(\text{eV})$ $n(\text{cm}^{-3})$ | 0.043 | 0.518 |
|---|-----------------------|-----------------------|
| 10^7 | 4.1×10^{-12} | 2.5×10^{-13} |
| 10^8 | 9.3×10^{-12} | 2.7×10^{-13} |
| 10^9 | 2.7×10^{-11} | 3.1×10^{-13} |
| 10^{10} | 1.1×10^{-10} | 3.6×10^{-13} |
| 10^{11} | 1.0×10^{-9} | 4.0×10^{-13} |
| 10^{12} | 9.0×10^{-9} | 4.0×10^{-13} |

In Eqs. (2.13a)-(2.13d) the parameter N is a constant which is determined by the actual quantitative density at some specified point in the density profile (e.g., $x = 0$) and $2L$ is the periodicity length. Figures 2.1a-d are plots, for the four different density profiles, of $a_0(t)/N$ versus

$$\epsilon = N[(\gamma+1) \beta t]^{1/(\gamma+1)} \quad , \quad (2.14)$$

for recombination at $T_e = 0.043$ eV and $T_e = 0.518$ eV. Because $a_0(t)$ is directly proportional to the total ion density for $-L \leq x \leq L$ at any time, t , it is evident from the figures that the rate of total density decay for the two values of T_e considered, is most rapid for $\epsilon < 1$ when density is greatest. This feature of the figures is clearly consistent with Eq. (2.1) and the positive values of β and γ given by Eqs. (2.12a-b). There are two other ubiquitous features of Figures 2.1a-d. First, the curves for $T_e = 0.043$ eV decrease less rapidly than those for $T_e = 0.518$ eV when ϵ is small. This characteristic of the curves is, from Eqs. (2.8) and (2.14), a consequence of

$$a_0(t) \approx (2L)^{1/2} N \int_0^L dx \frac{n_0(x)}{N} \left[1 - \frac{1}{\gamma+1} \left(\frac{\epsilon n_0(x)}{N} \right)^{\gamma+1} \right] \quad , \quad (2.15a)$$

$$\frac{da_0(t)}{d\epsilon} \approx -(2L)^{1/2} N \int_0^L dx \left(\frac{n_0(x)}{N} \right)^{\gamma+2} \epsilon^\gamma \quad , \quad (2.15b)$$

and γ being larger for $T_e = 0.043$ eV than for $T_e = 0.518$ eV. Second, for asymptotically large values of ϵ the curves, for the two different temperatures, approach each other because

$$a_0(t) \approx \frac{(2L)^{1/2} N}{\epsilon} \quad , \quad (2.16a)$$

$$\frac{da_0(t)}{d\epsilon} \approx - \frac{(2L)^{1/2} N}{\epsilon^2} \quad , \quad (2.16b)$$

which is independent of γ .

Figures 2.2a-d and 2.3a-d are plots of the four density profiles in normalized units, $n(x,t)/N$, as a function of (x/L) for $T_e = 0.043$ eV and 0.518 eV,

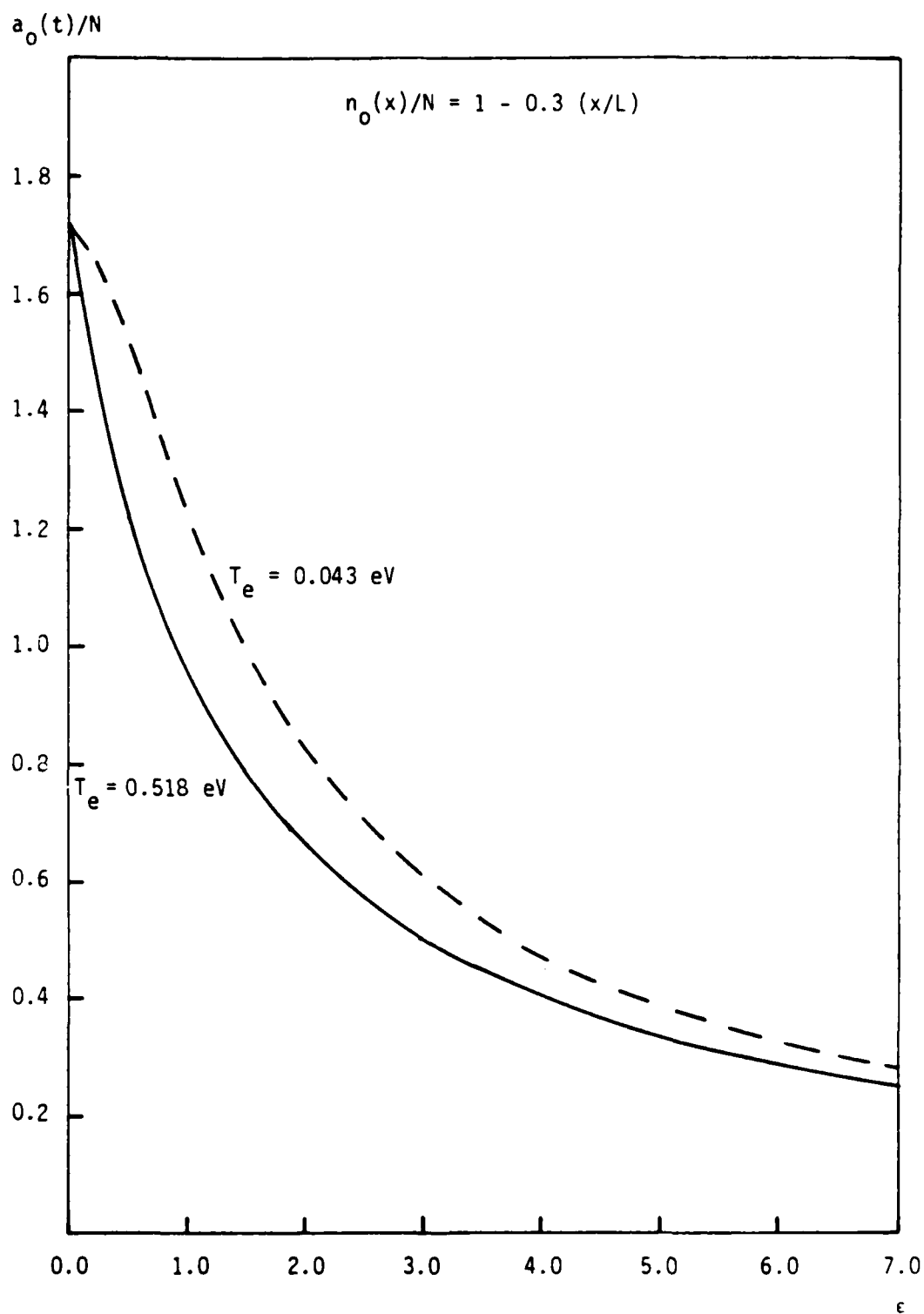


Figure 2.1a. $a_0(t)/N$ versus ϵ for $T_e = 0.043$ eV and 0.518 eV, respectively. Initial density profile specified by Eq. (2.13a).

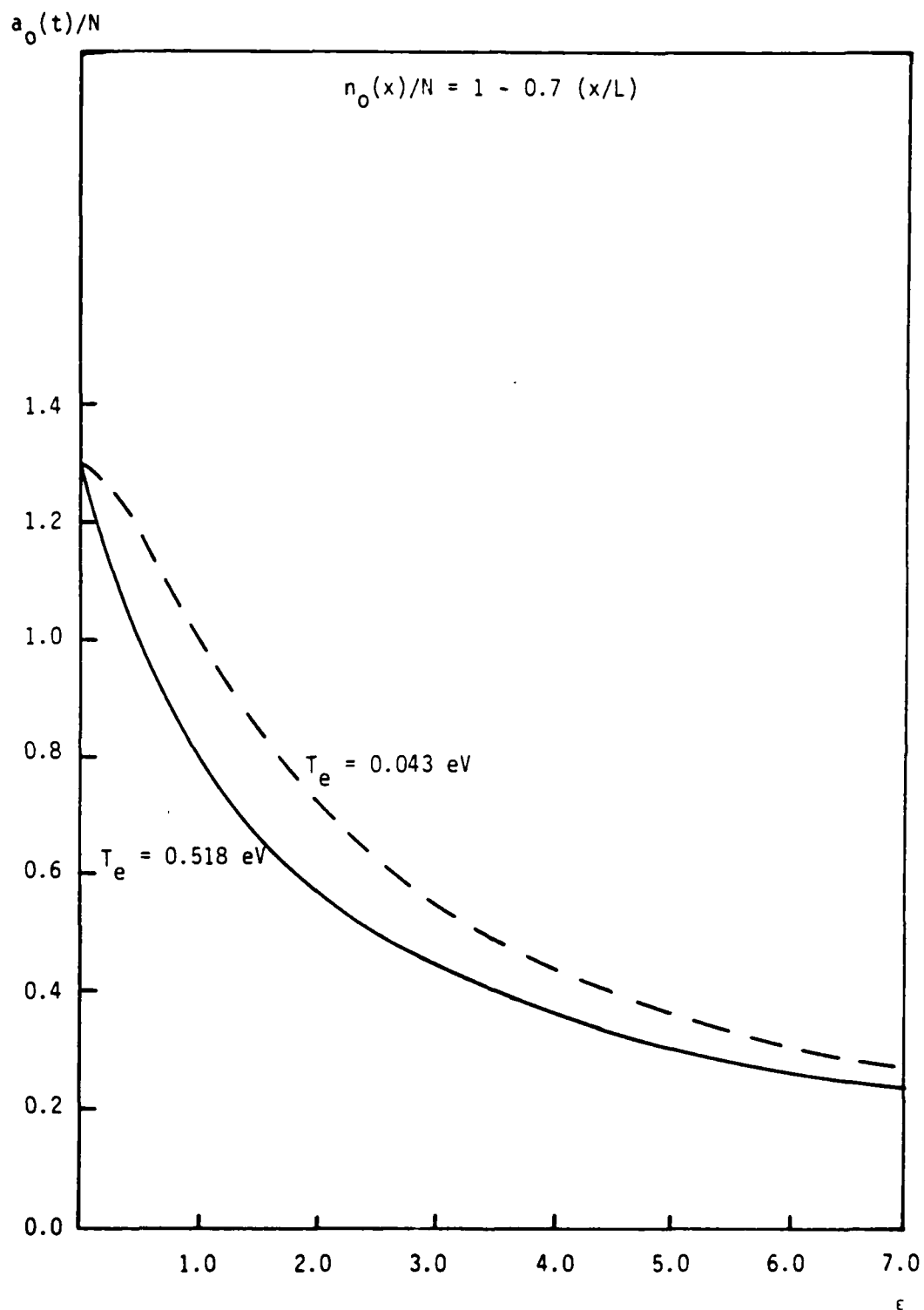


Figure 2.1b. $a_0(t)/N$ versus ϵ for $T_e = 0.043$ eV and 0.518 eV, respectively. Initial^e density profile specified by Eq. (2.13b).

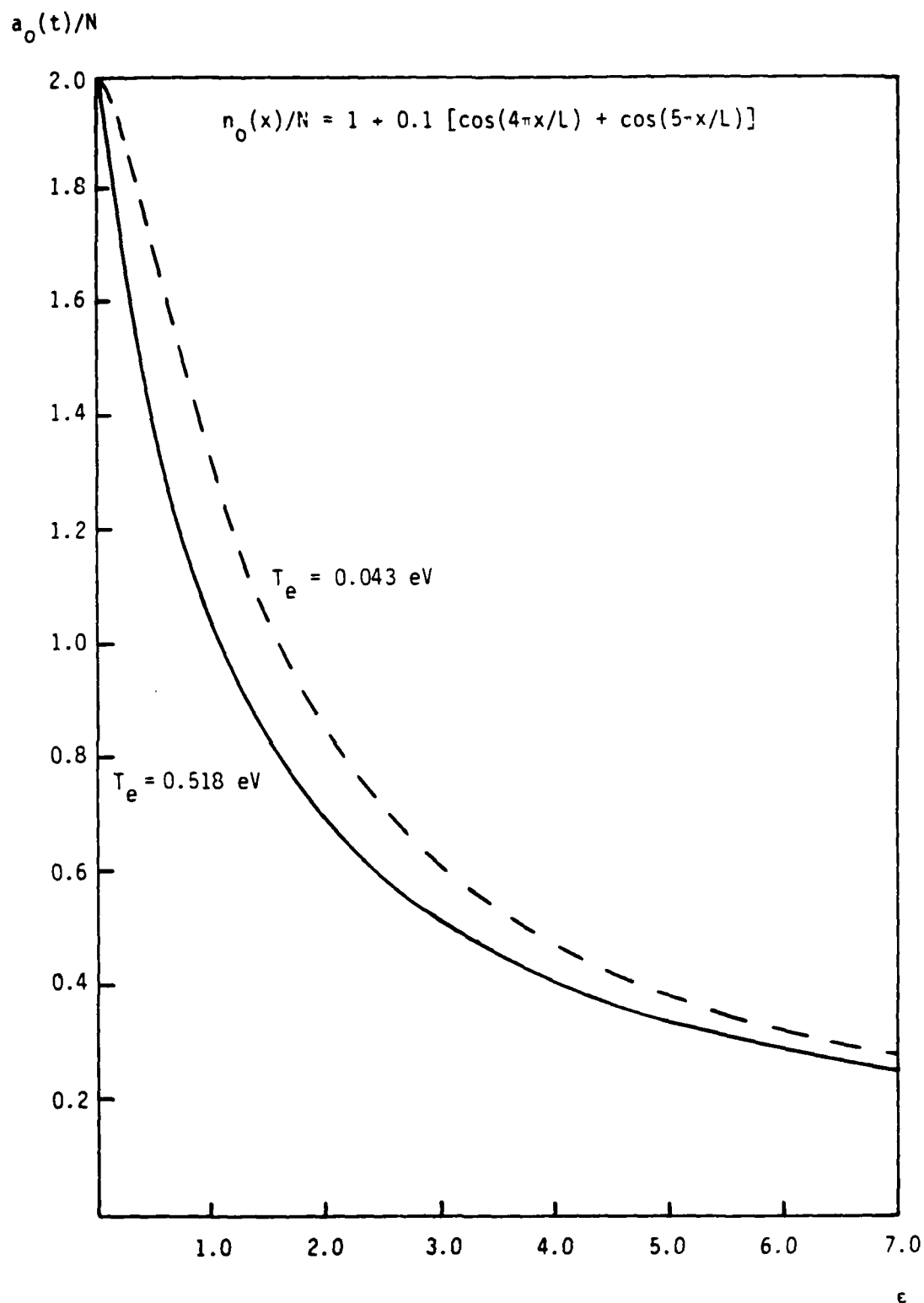


Figure 2.1c. $a_0(t)/N$ versus ϵ for $T_e = 0.043 \text{ eV}$ and 0.518 eV , respectively. Initial density profile specified by Eq. (2.13c).

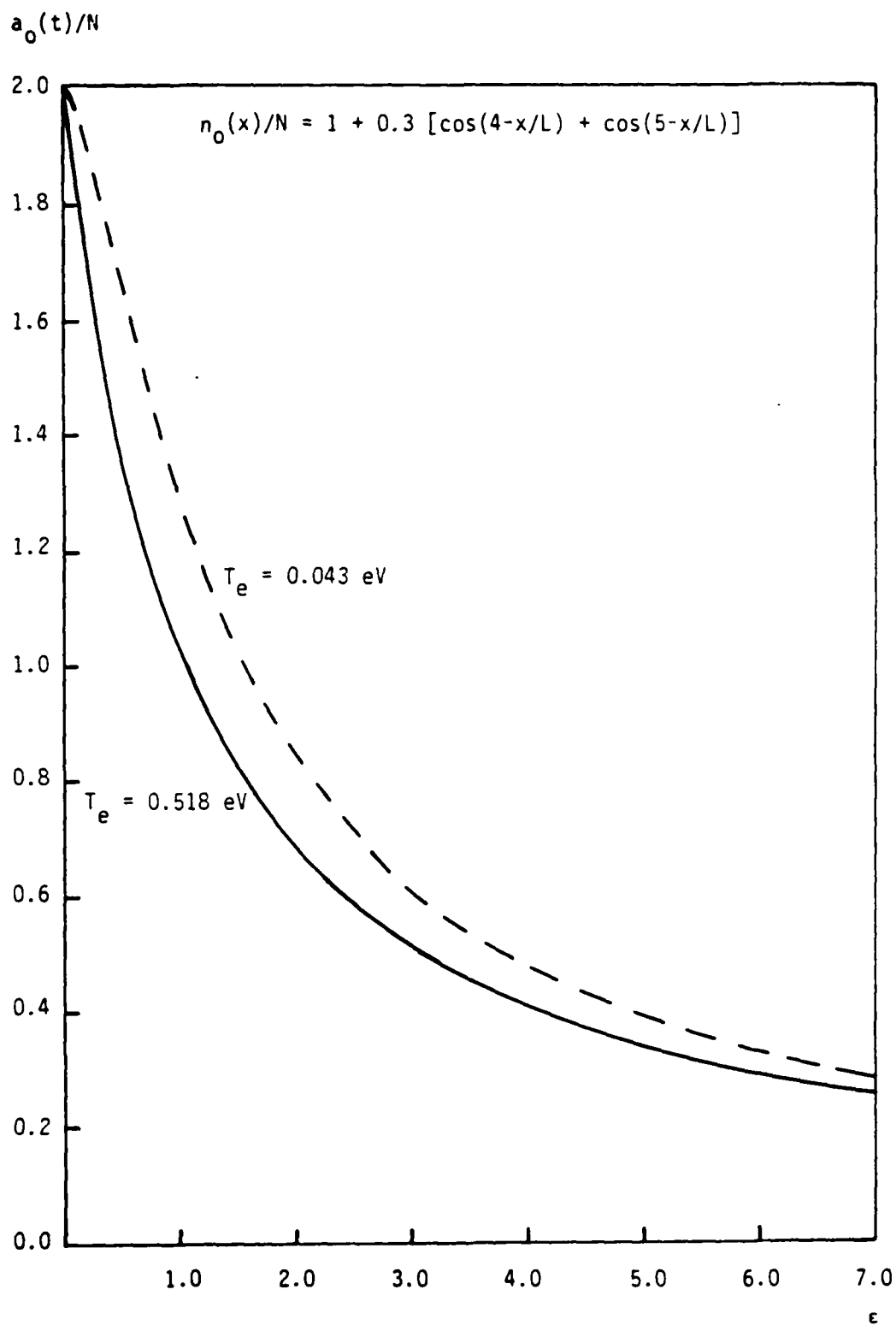


Figure 2.1d. $a_0(t)/N$ versus ϵ for $T_e = 0.043 \text{ eV}$ and 0.518 eV , respectively. Initial density profile specified by Eq. (2.13d).

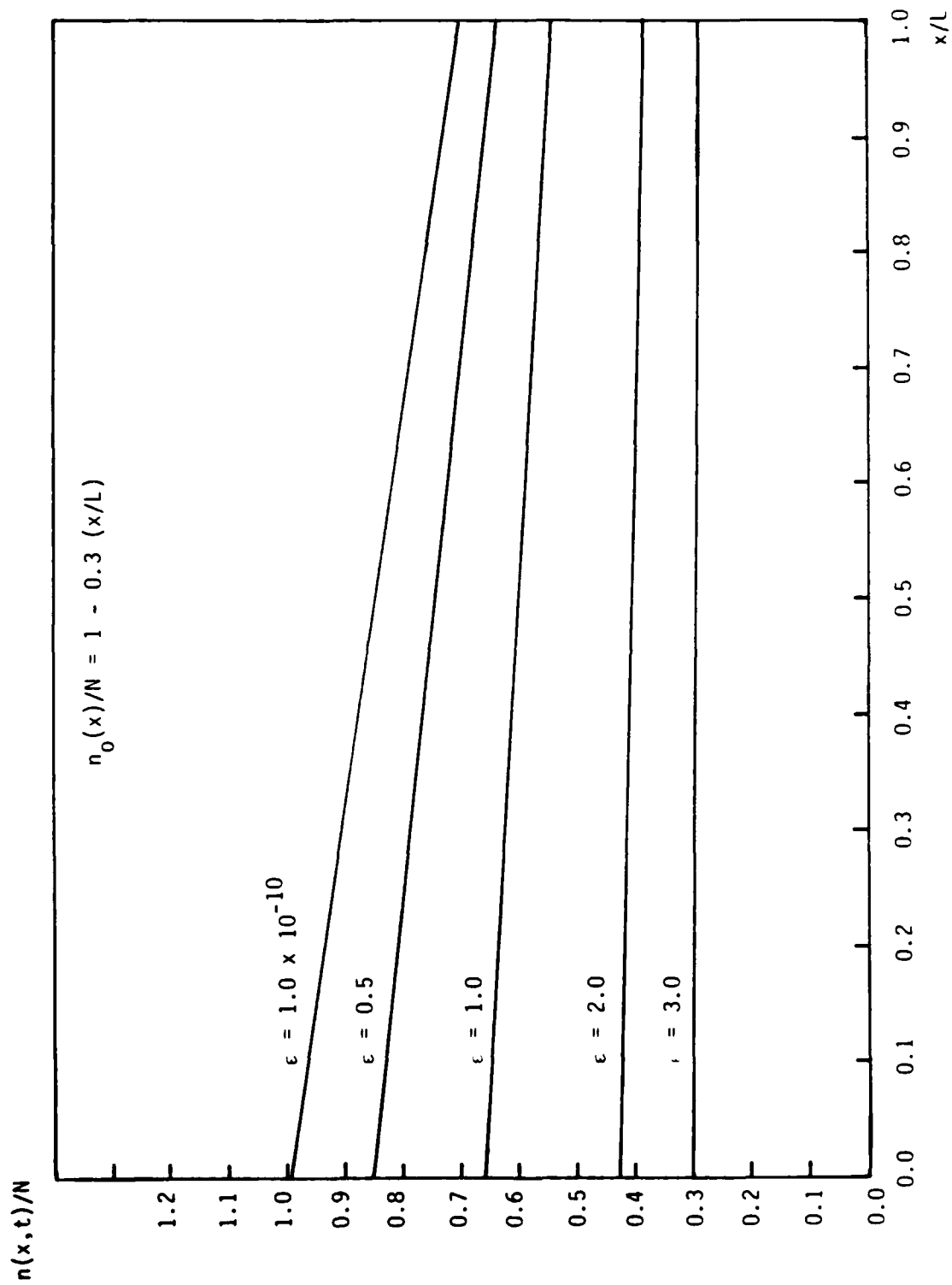


Figure 2.2a. $n(x,t)/N$ versus x/L for $T_e = 0.043$ eV and various ϵ . Initial density profile specified by Eq. (2.13a).

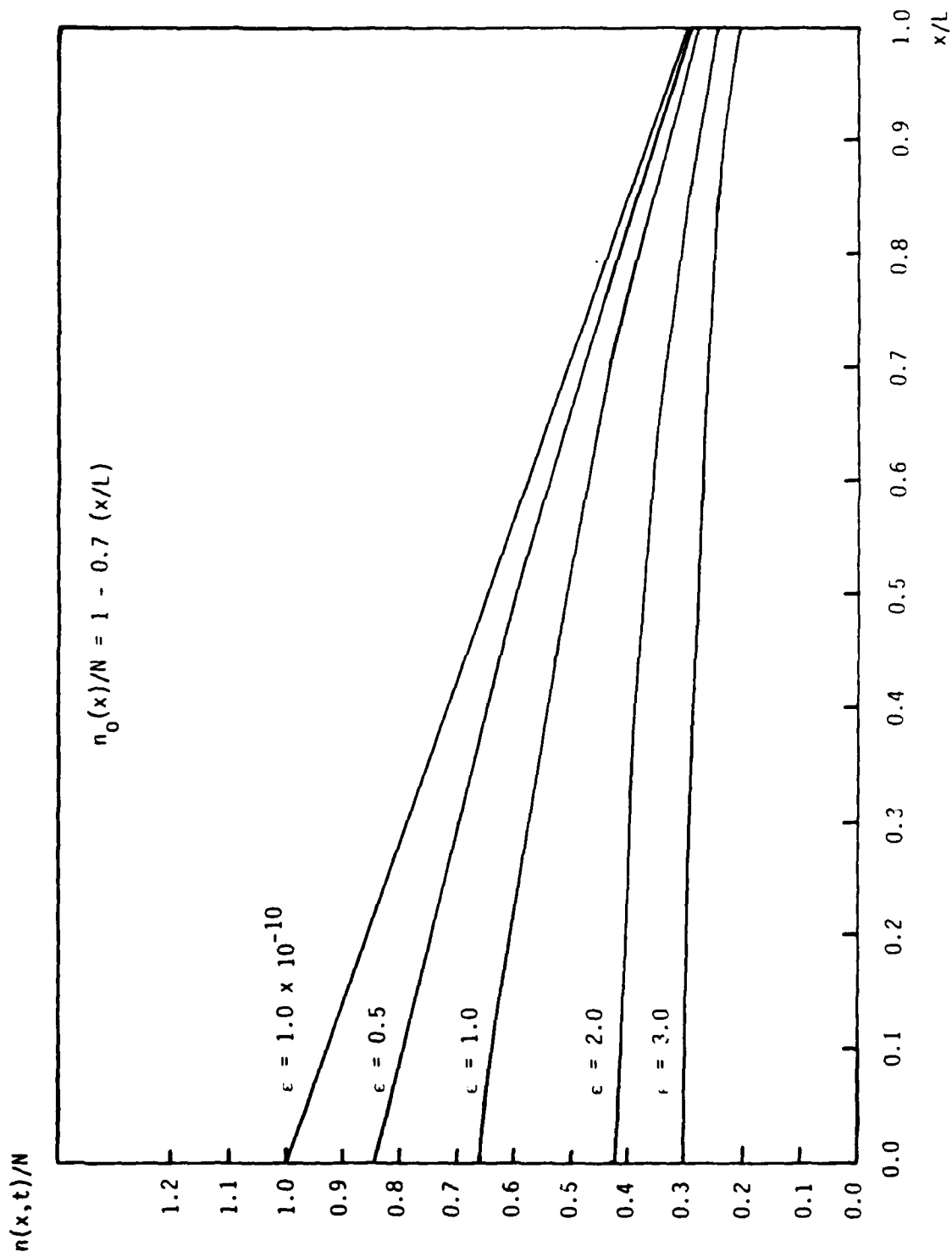


Figure 2.2b. $n(x,t)/N$ versus x/L for $T_e = 0.043$ eV and various ϵ . Initial density profile specified by Eq. (2.13b).

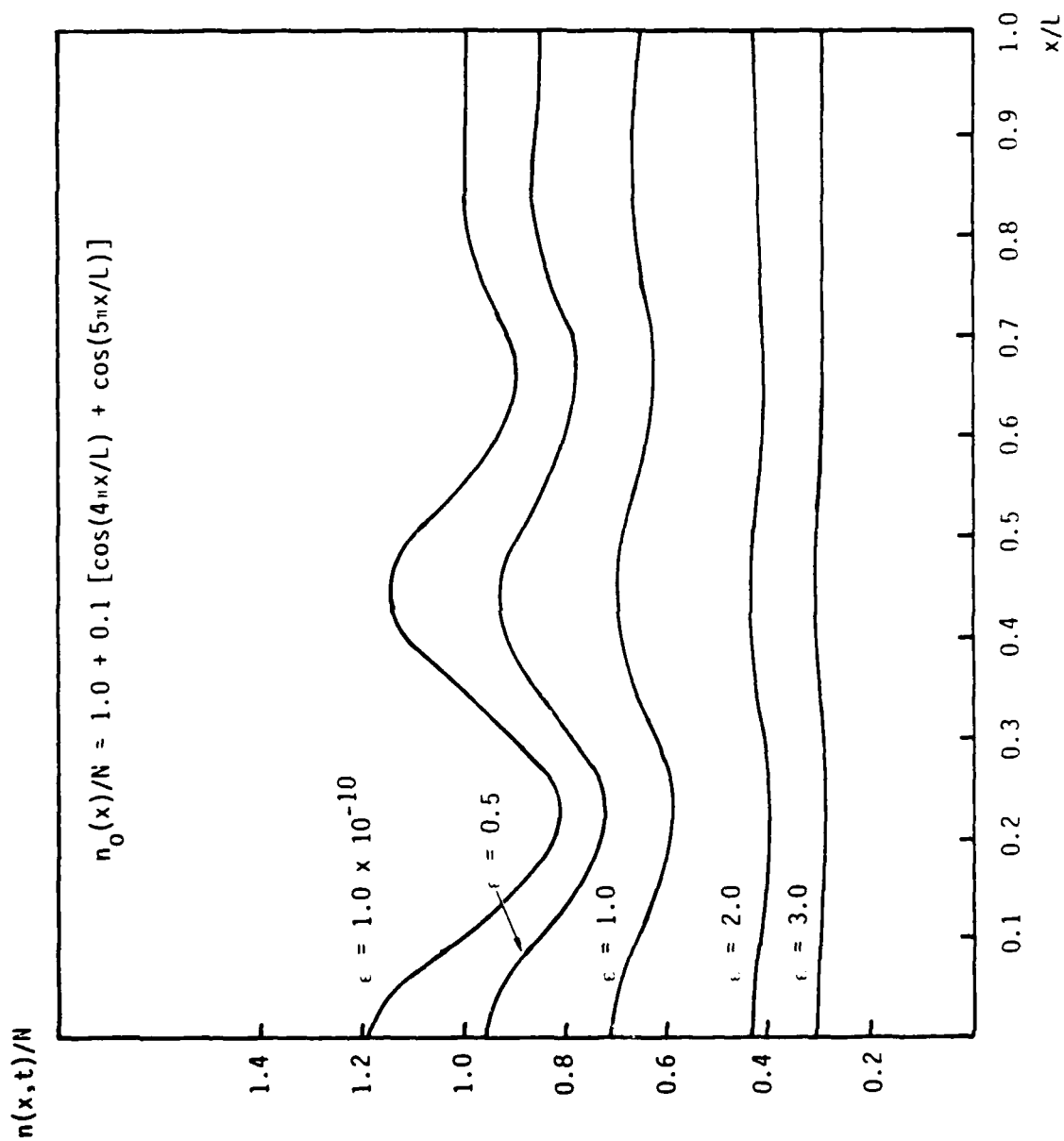


Figure 2.2c. $n(x,t)/N$ versus x/L for $T_e = 0.043$ eV and various ϵ . Initial density profile specified by Eq. (2.13c).

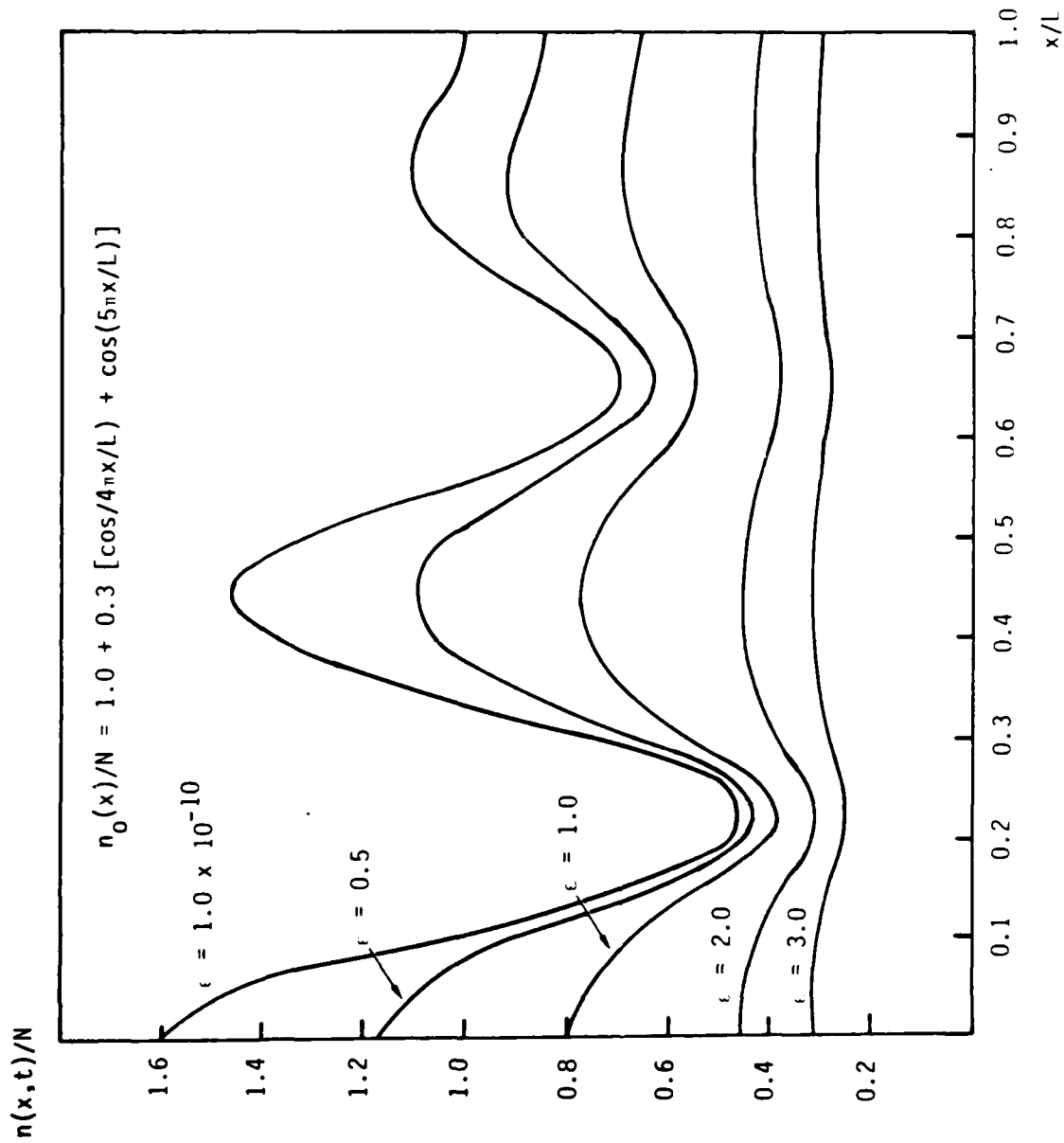


Figure 2.2d. $n(x,t)/N$ versus x/L for $T_e = 0.043$ eV and various ϵ . Initial density profile specified by Eq. (2.13d).

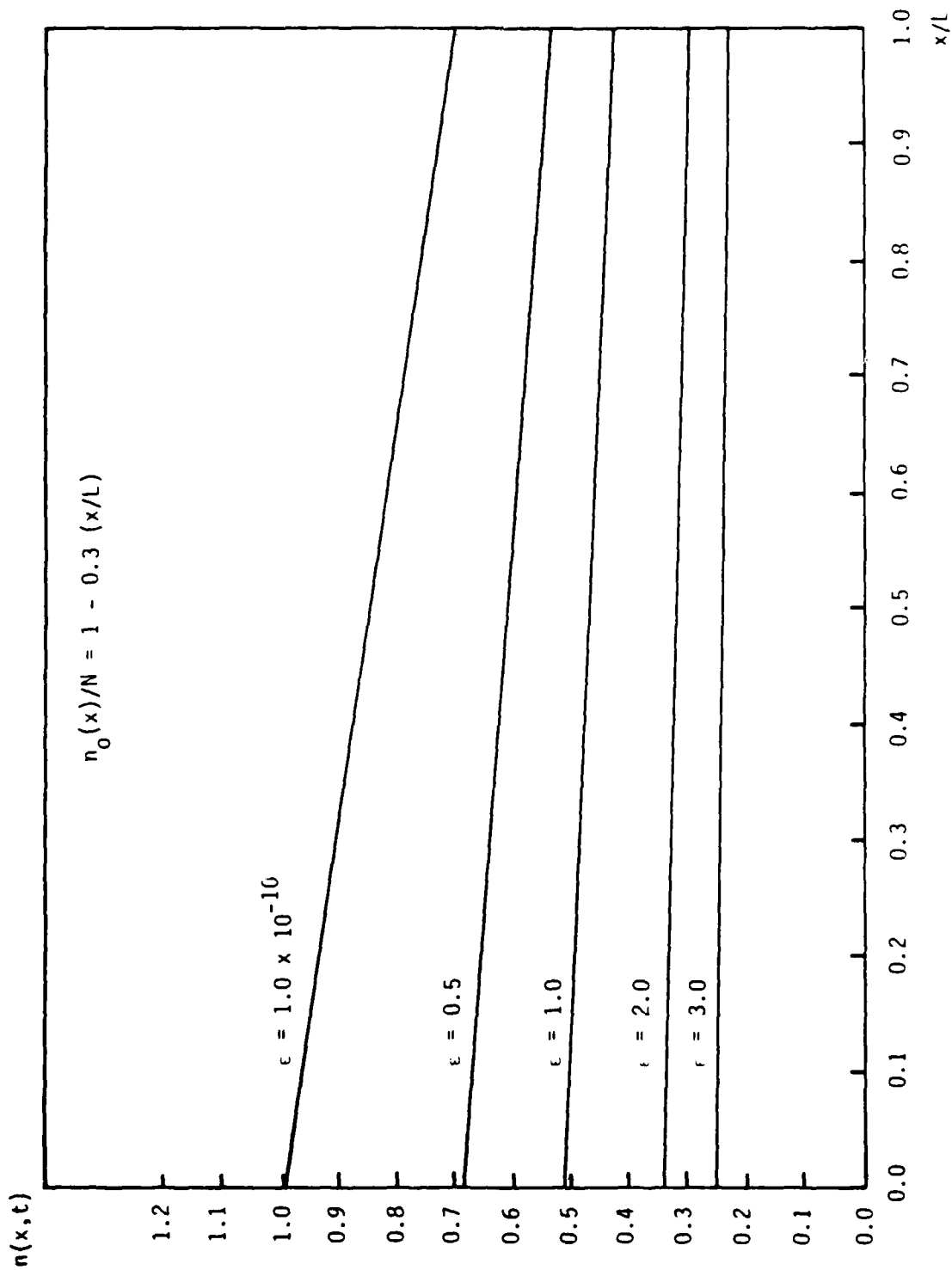


Figure 2.3a. $n(x,t)/N$ versus x/L for $T_e = 0.518$ eV and various ϵ .
Initial density profile specified by Eq. (2.13a).

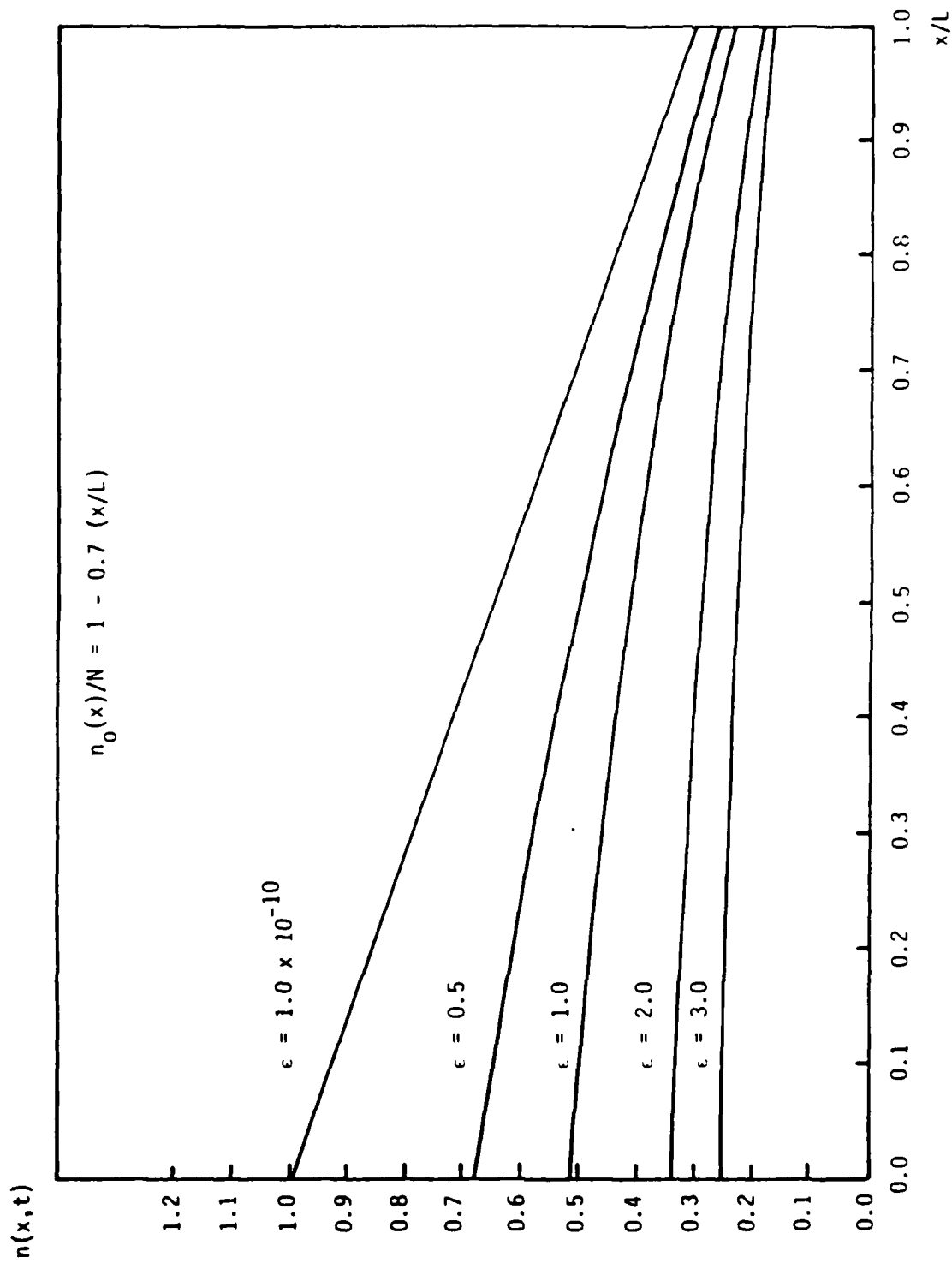


Figure 2.3b. $n(x,t)/N$ versus x/L for $T_e = 0.518$ eV and various ϵ . Initial density profile specified by Eq. (2.13b).

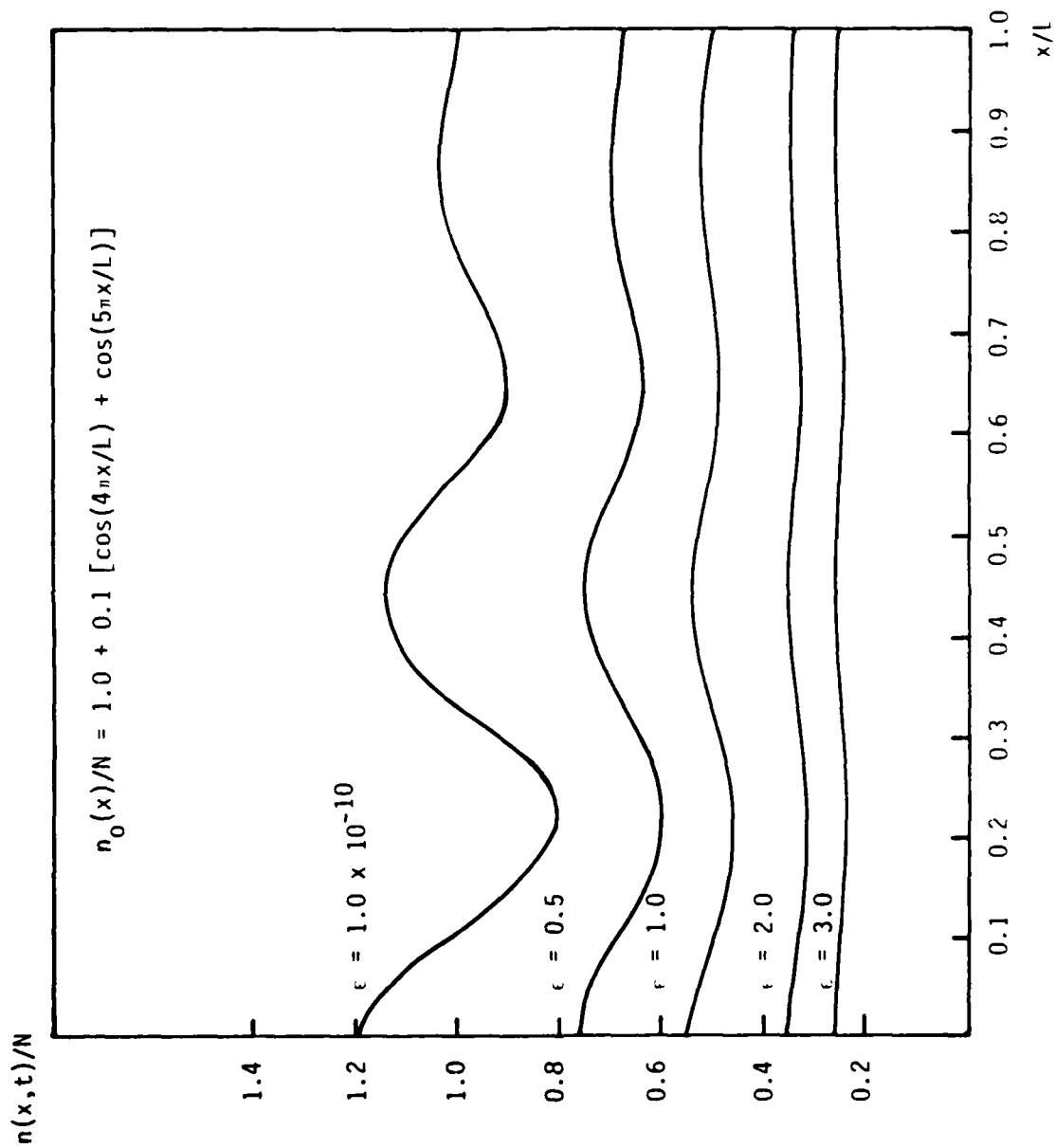


Figure 2.3c. $n(x,t)/N$ versus x/L for $T_e = 0.518$ eV and various ϵ . Initial density profile specified by Eq. (2.13c).

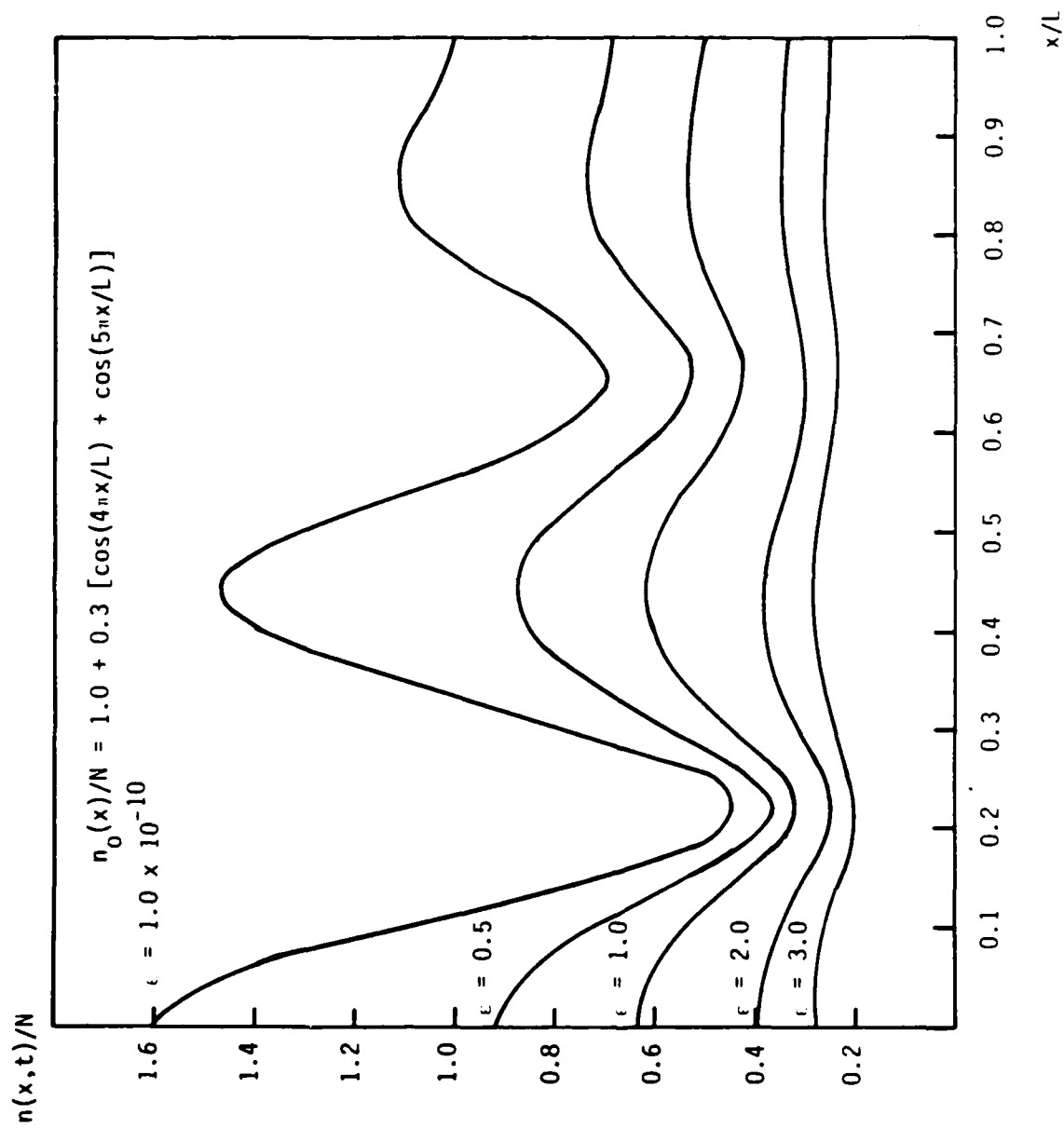


Figure 2.3d. $n(x,t)/N$ versus x/L for $T_e = 0.518$ eV and various ϵ . Initial density profile specified by Eq. (2.13d).

respectively. In the figures the various curves correspond to different assumed values of ϵ . A general characteristic of all the figures is the tendency for recombination to simultaneously reduce both the absolute density and density inhomogeneity. This characteristic is a consequence of the more rapid decay of charged particle density in spatial locations where the density is initially largest and the weaker decay at locations where density is initially smallest.

Because the recombination decay rate is strongly dependent upon density, the Fourier spectrum of the various initially inhomogeneous density profiles must be a function of time. Indeed, Figures 2.4a-d and 2.5a-d, which are plots of $|a_p(t)/a_0(t)|$ versus ϵ for different values of harmonic number, p , clearly demonstrate the time variation of the Fourier coefficients for the various density profiles considered. In Figures 2.4a-d and 2.5a-d the temperatures considered are $T_e = 0.043$ eV and 0.518 eV, respectively. The figures have several significant features. First, the absolute magnitude of $|a_p(t)/a_0(t)|$ is dependent upon the degree of density inhomogeneity. Specifically, as inhomogeneity increases the contribution of the $p \neq 0$ Fourier amplitudes which are initially present always decay relative to $a_0(t)$. This decay is a consequence of the density inhomogeneity erosion associated with recombination. Third, the $p \neq 0$ Fourier amplitudes which are not initially present generally grow relative to $a_0(t)$ for small values of ϵ . Only Figure 2.4d shows evidence of more complicated behavior superimposed on the general growth. The relative growth is caused by both the change in density profile shape and the simultaneous general decay of $a_0(t)$ (i.e., total density). The more complicated feature of Figure 2.4d is a consequence of the change in sign of certain $a_p(t)$ as ϵ increases from zero. Fourth, those $|a_p(t)/a_0(t)|$ which initially increase attain their maximum value for $\epsilon \sim 1$. For larger ϵ , these $|a_p(t)/a_0(t)|$ decrease. Fifth, for asymptotically large values of ϵ all $|a_p(t)/a_0(t)|$ for a specific electron temperature decay at the same rate. In particular from Eqs. (2.10a-b),

$$|a_p(t)/a_0(t)| \sim 1/\epsilon^{\gamma+1} \quad , \quad (2.17)$$

is independent of density profile and so density profiles become uniform on a faster time scale than total ionization decay. Because the value of γ is larger for $T_e = 0.043$ eV than for $T_e = 0.518$ eV, the relative decrease of the Fourier amplitudes as specified by Eq. (2.17) is more rapid at the lower temperature.

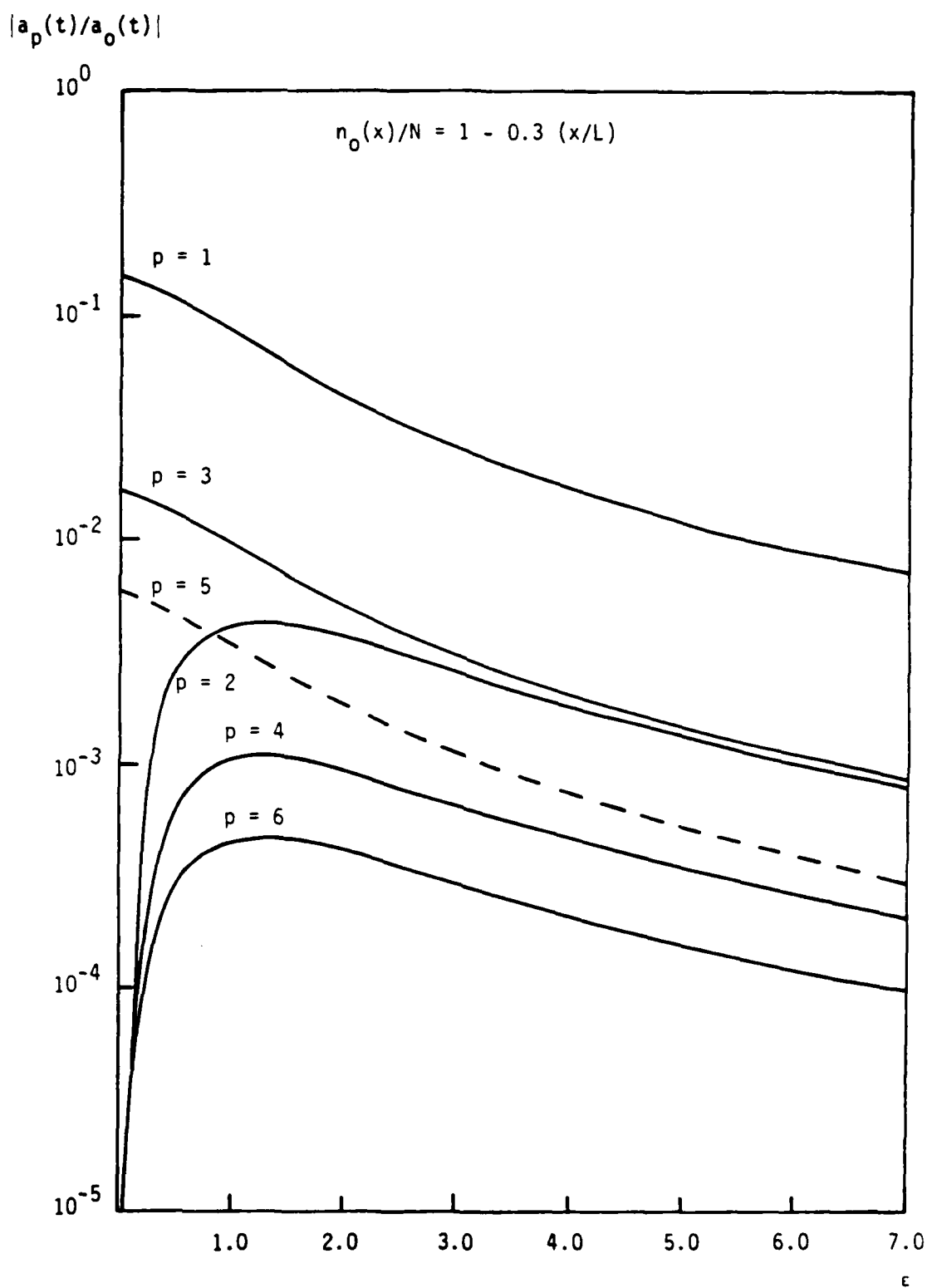


Figure 2.4a. $|a_p(t)/a_0(t)|$ versus ϵ for $T_e = 0.043$ eV and various p . Initial density profile specified by Eq. (2.13a)

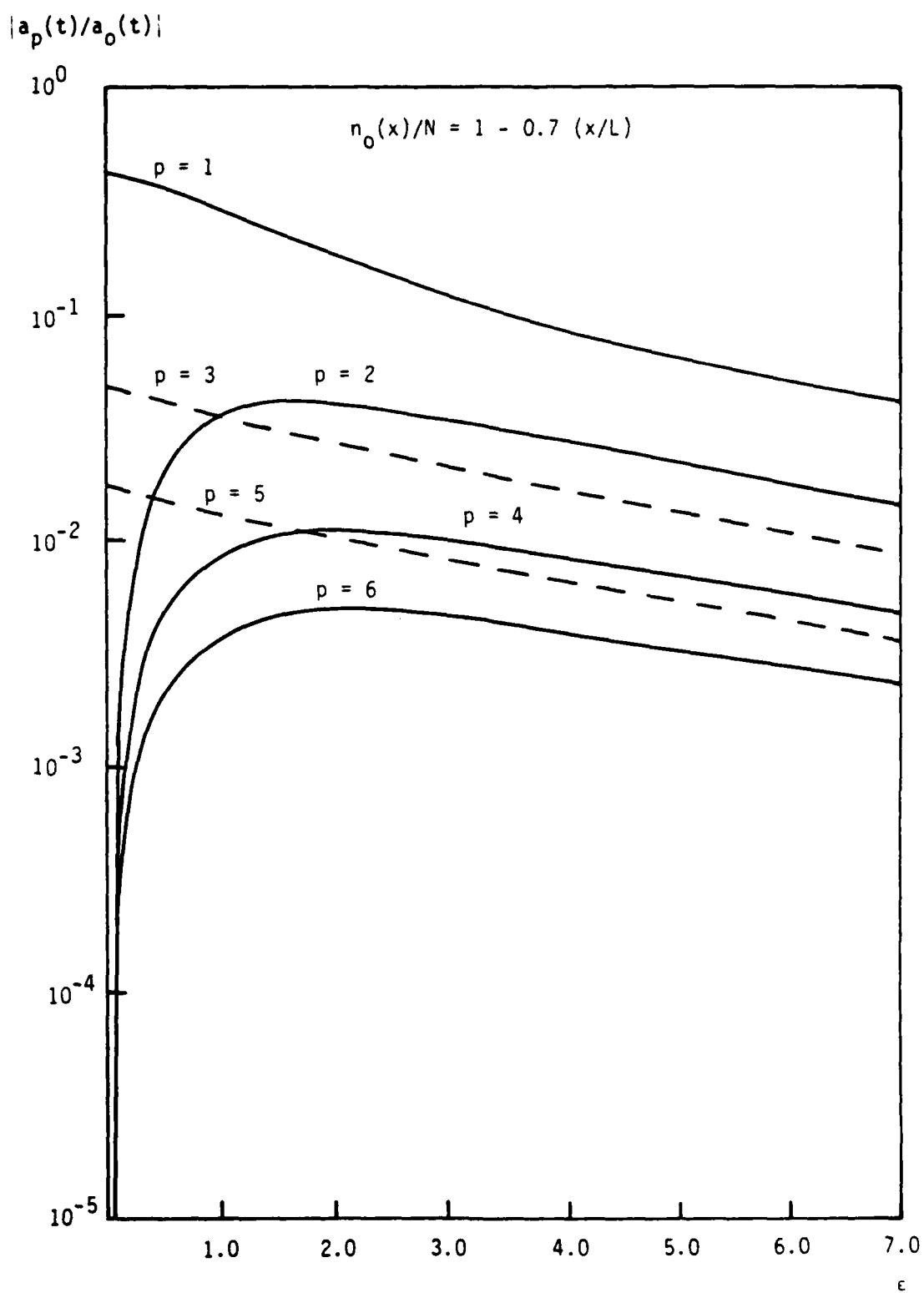


Figure 2.4b. $|a_p(t)/a_0(t)|$ versus ϵ for $T_e = 0.043$ eV and various p . Initial density profile specified by Eq. (2.13b).

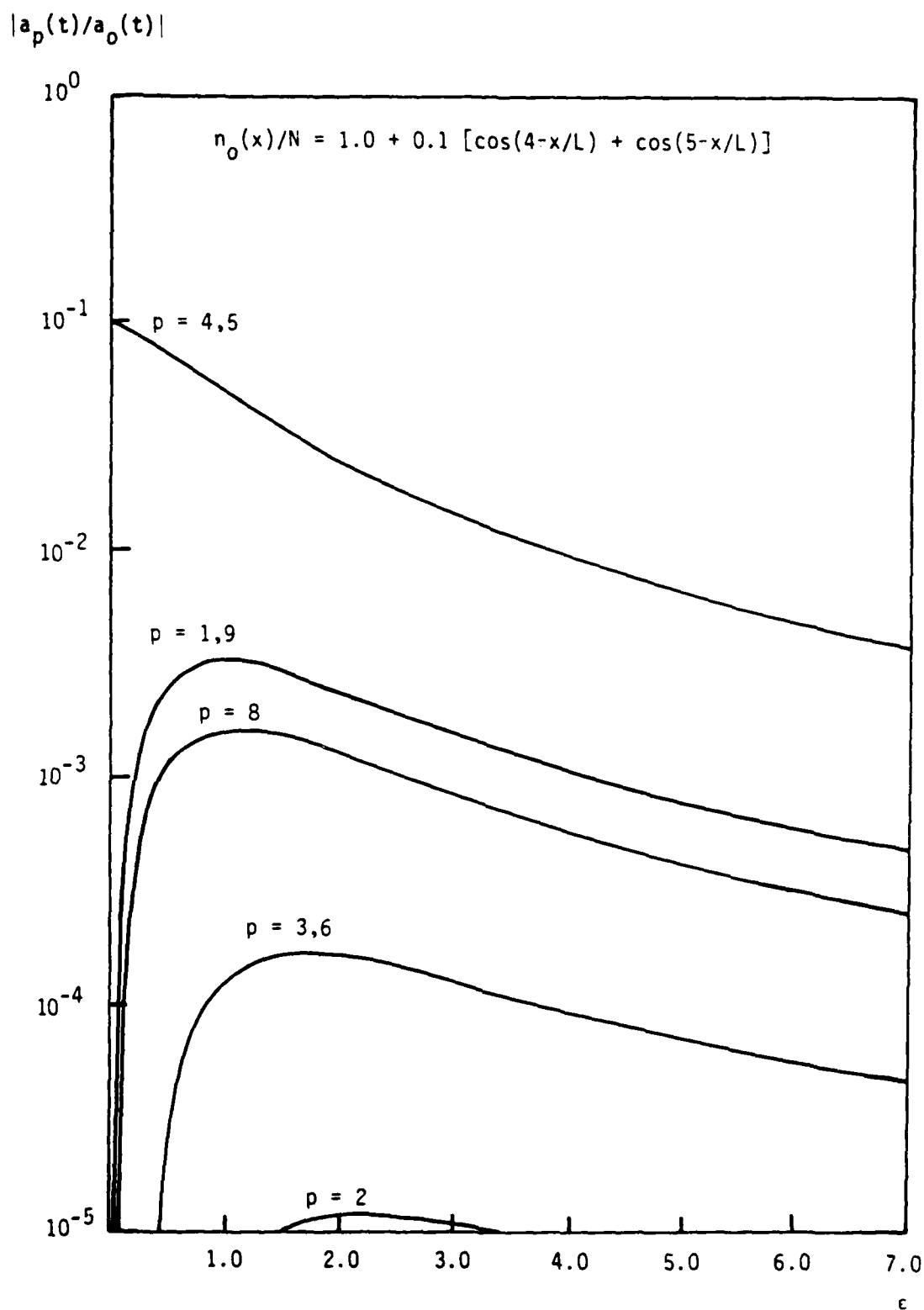


Figure 2.4c. $|a_p(t)/a_0(t)|$ versus ϵ for $T_e = 0.043$ eV and various p . Initial density profile specified by Eq. (2.13c).

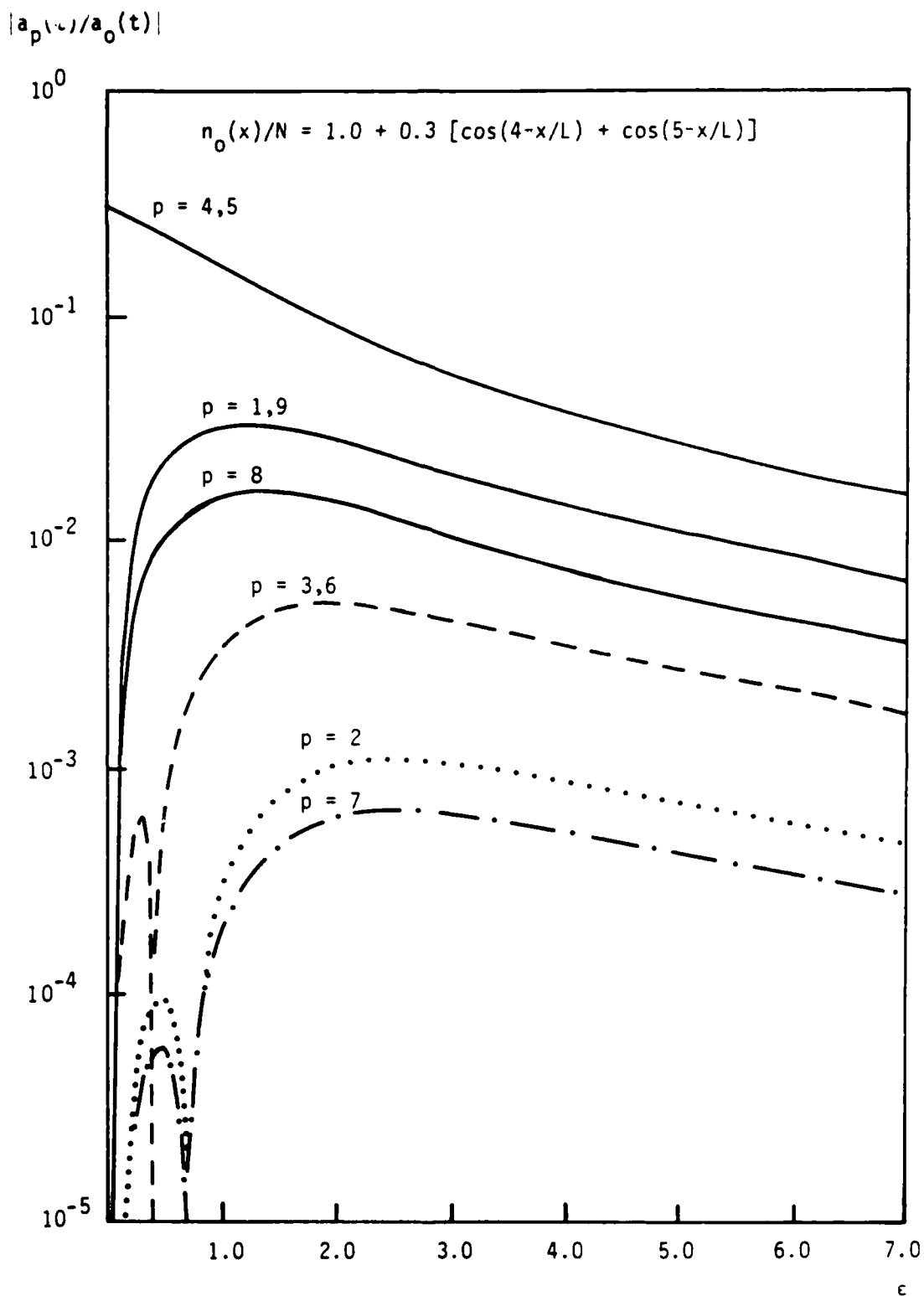


Figure 2.4d. $|a_p(t)/a_0(t)|$ versus ϵ for $T_e = 0.043$ eV and various p . Initial density profile specified by Eq. (2.13d).

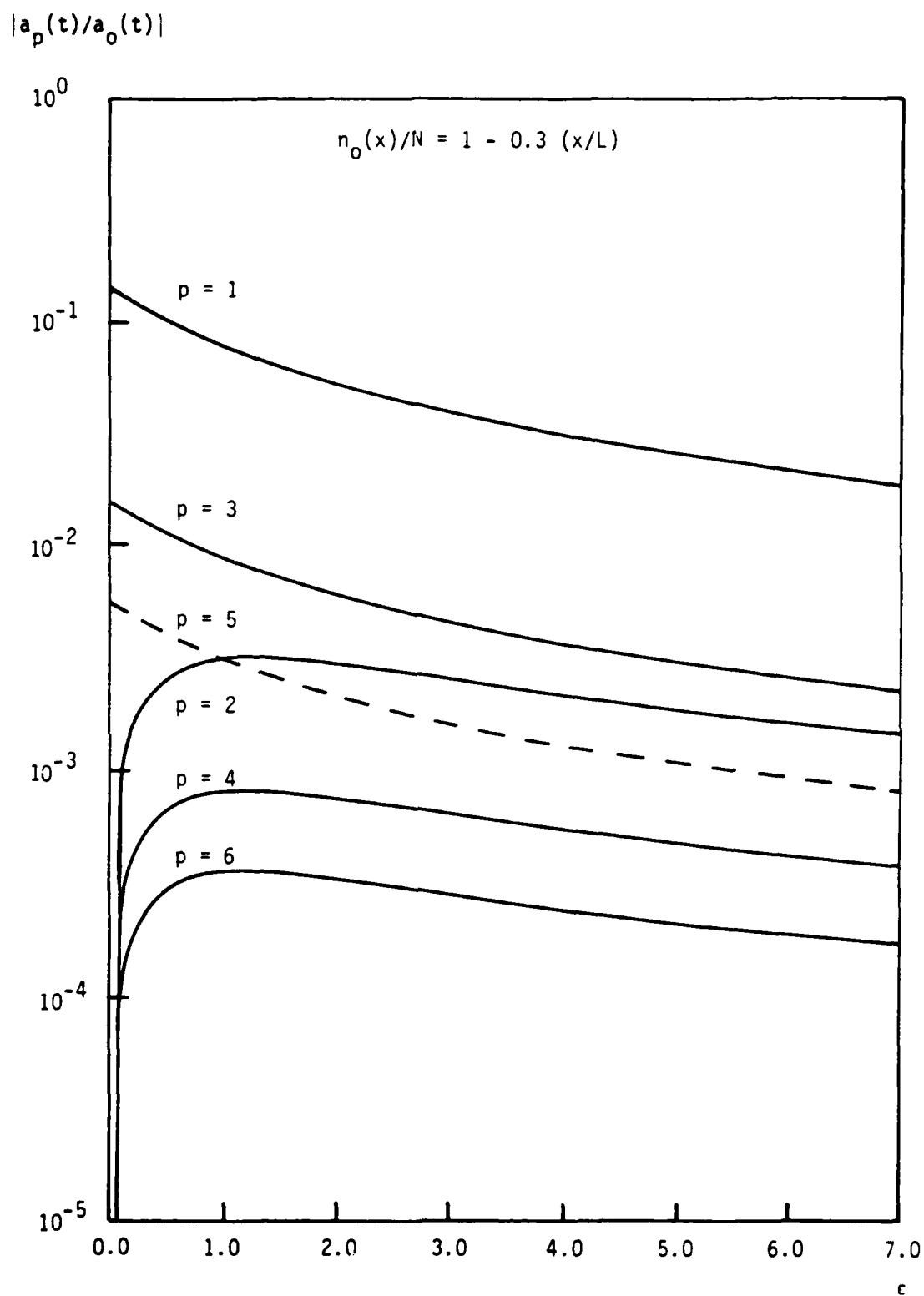


Figure 2.5a. $|a_p(t)/a_0(t)|$ versus ϵ for $T_e = 0.518$ eV and various p .
Initial density profile specified by Eq. (2.13a).

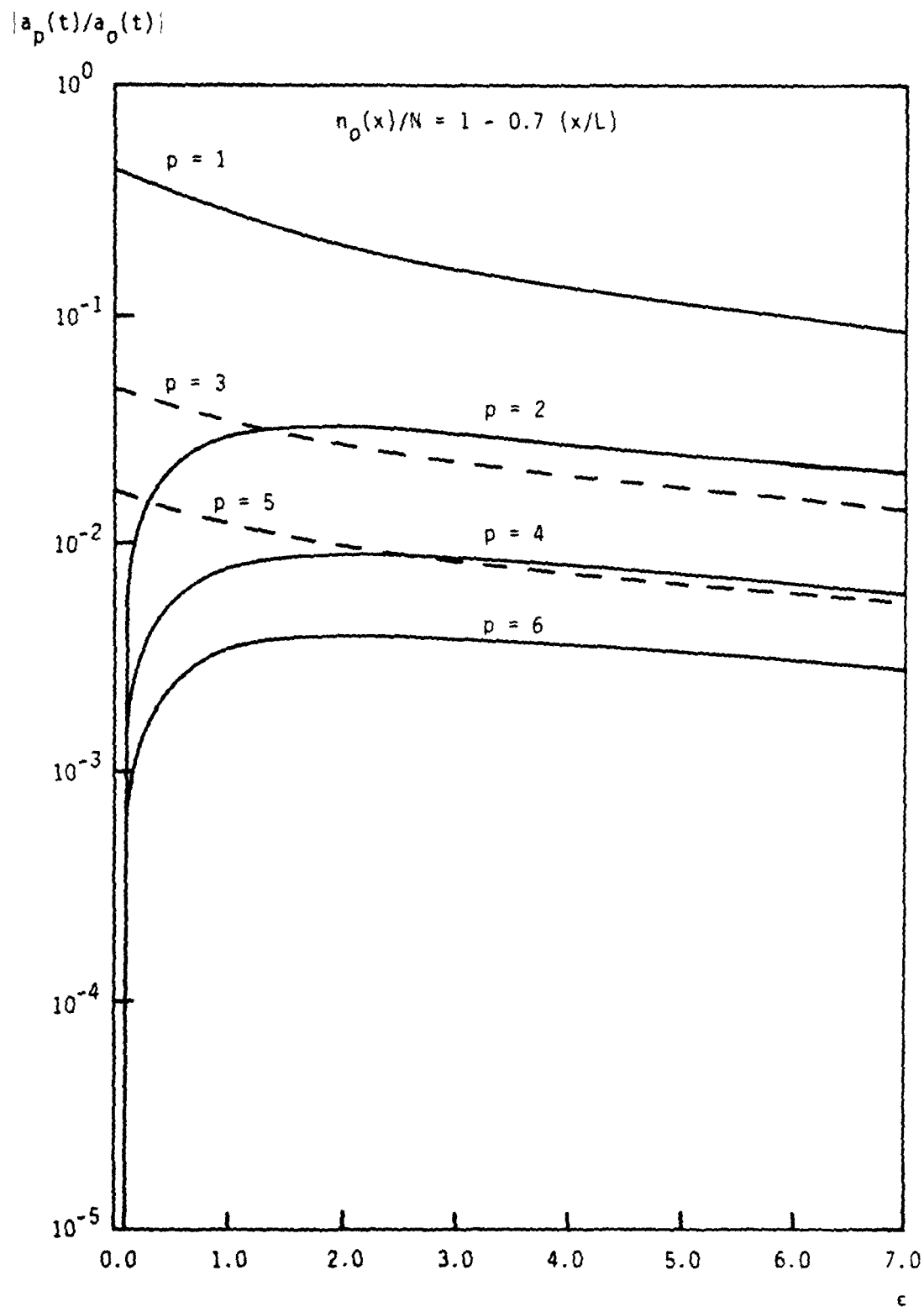


Figure 2.5b. $|a_p(t)/a_0(t)|$ versus ϵ for $T_e = 0.518$ eV and various p . Initial density profile specified by Eq. (2.13b).

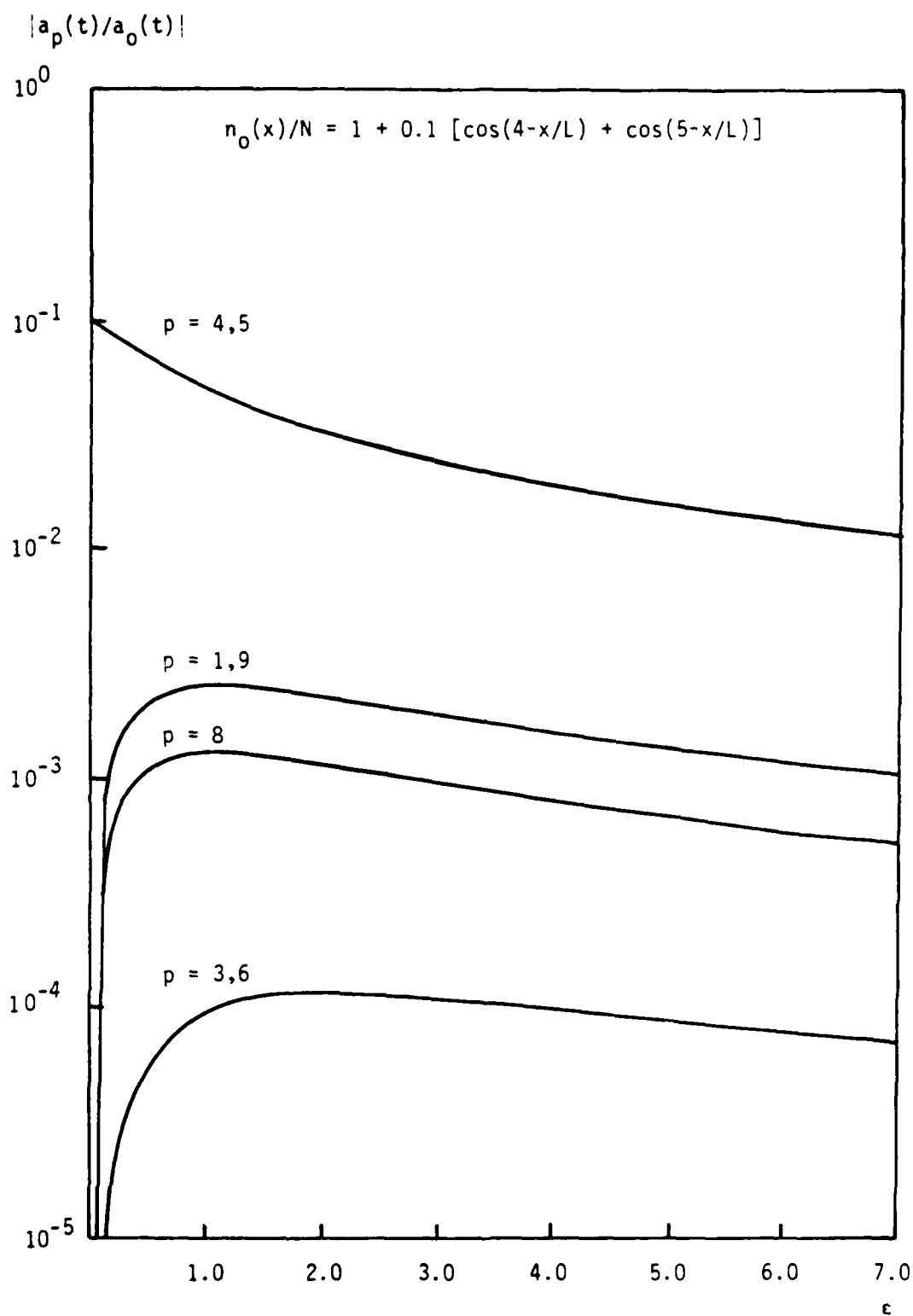


Figure 2.5c. $|a_p(t)/a_0(t)|$ versus ϵ for $T_e = 0.518$ eV and various p .
Initial density profile specified by Eq. (2.13c).

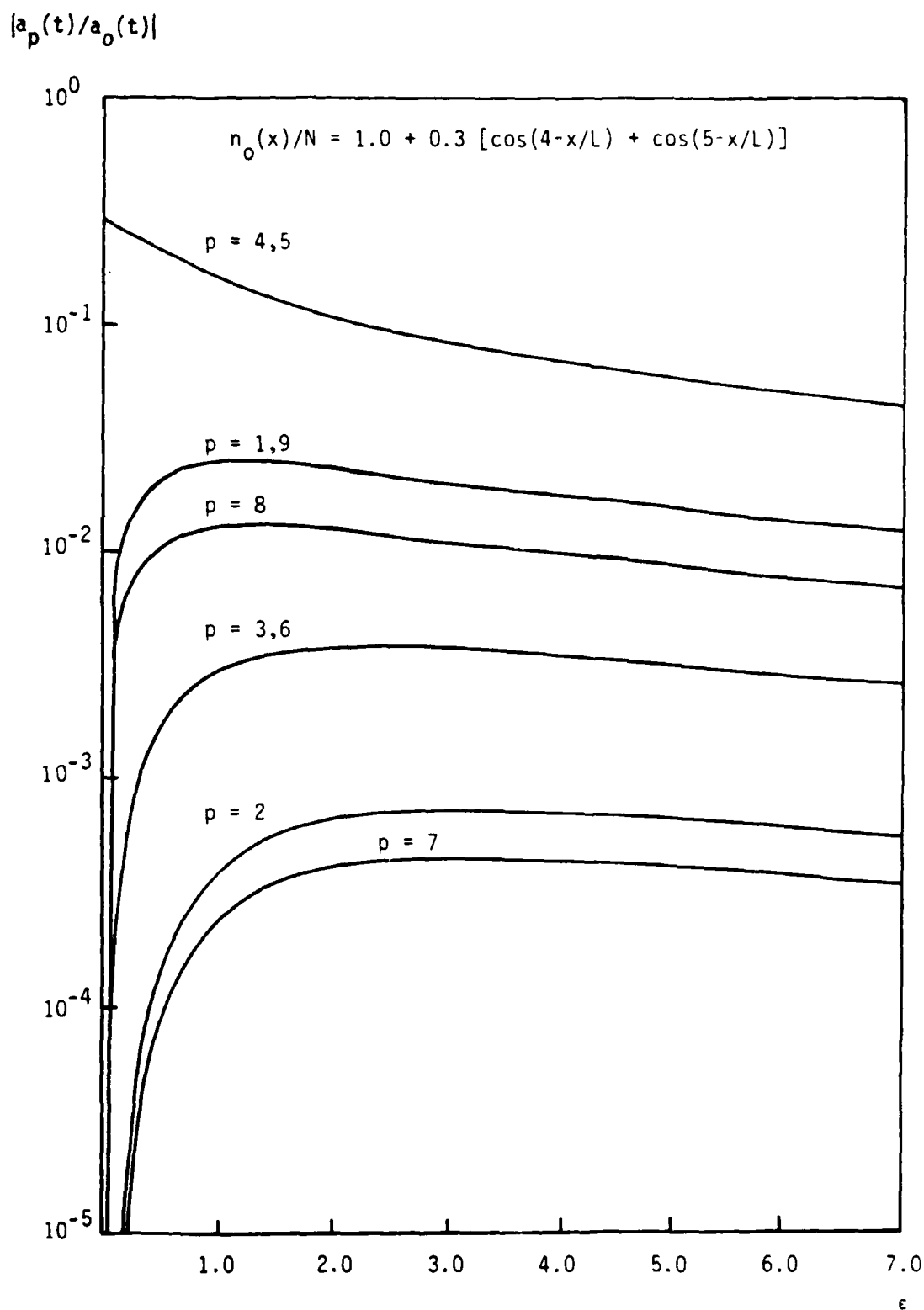


Figure 2.5d. $|a_p(t)/a_0(t)|$ versus ϵ for $T_e = 0.518$ eV and various p . Initial density profile specified by Eq. (2.13d).

The qualitative variation of certain of the $|a_p(t)/a_0(t)|$ on ϵ has been shown to be different depending on whether $\epsilon \lesssim 1$ or $\gtrsim 1$. This change in behavior can be related to real time by using Eqs. (2.10a-b) and (2.14). Figures 2.6a-b are plots of t (second) versus ϵ for $T_e = 0.043$ and 0.518 eV, respectively. The different curves in each of the figures correspond to different choices of density, $N(\text{cm}^{-3})$. The curves readily show that the recombination time scale, defined as the time when $\epsilon = 1$, is smallest when density is large and temperature is low. For example, in Figure 2.6a, $\epsilon = 1$ at approximately 12 seconds for $N = 1 \times 10^9 \text{ cm}^{-3}$ and at approximately 2.8×10^4 seconds for $N = 1 \times 10^7 \text{ cm}^{-3}$. Similarly in Figure 2.6b, $\epsilon = 1$ at approximately 25 seconds for $N = 1 \times 10^{11} \text{ cm}^{-3}$ and at approximately 3×10^3 seconds for $N = 1 \times 10^9 \text{ cm}^{-3}$. Other values of ϵ and the times to which they correspond can be read from the figures.

2.4 SUMMARY AND CONCLUSIONS

Recombination is a classical process which can both reduce total ionization and smooth out ionization density profiles irrespective of the plasma turbulence level. Hence, recombination is one classical process which provides a lower bound on the level of turbulence necessary to make the plasma behavior anomalous.

Because the temperature of the ionosphere is often comparable to 0.1 eV and the primary ionic species in the ionosphere is monatomic oxygen, the radiative combination is a relevant process for consideration in the ionosphere.^{2.1-2.4} Model calculations of the radiative recombination process for several different one-dimensional density profiles have been described for a neutral plasma containing monatomic oxygen atoms, the main neutral constituent in the ionosphere above approximately 300 kilometers.^{2.1} Qualitatively and quantitatively the radiative recombination process is identical for monatomic nitrogen.^{2.6}

The evaluation of the nonlinear recombination equation, Eq. (2.1), demonstrates the simultaneous change in the shape and total ionization of the density profiles. Time variation in the relative size of Fourier amplitudes is a direct consequence of the change in density morphology. In particular, for very short times, such that $\epsilon \ll 1$, those Fourier amplitudes not initially present for the density profile have a general tendency to grow relative to $a_0(t)$. Subsequently, for $\epsilon \gg 1$, all $p \neq 0$ Fourier amplitudes decay in the same functional way relative to $a_0(t)$. For long-times, $a_0(t)$ and total ionized particle density decay inversely

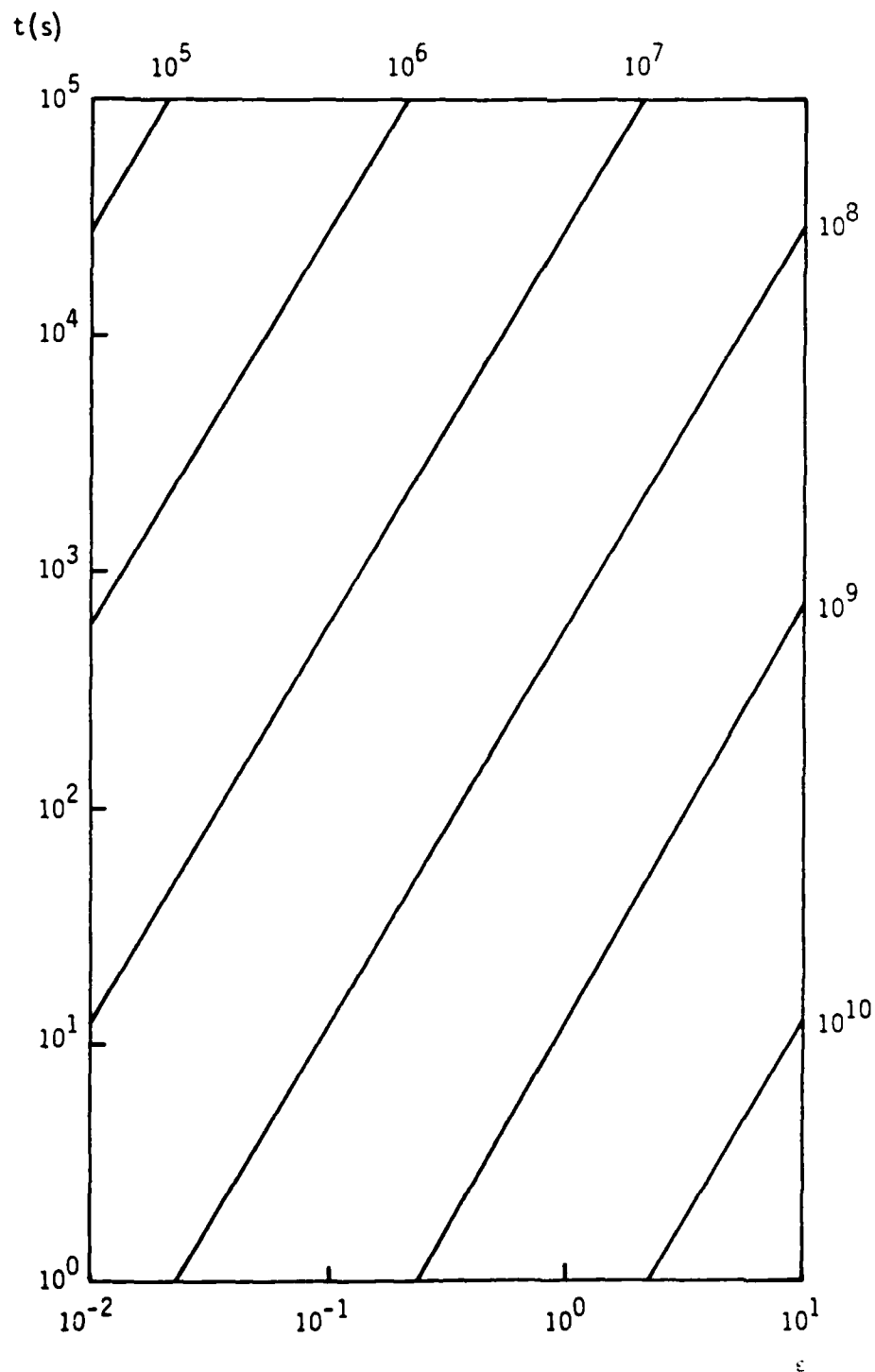


Figure 2.6a. $t(s)$ versus ϵ for $T_e = 0.043$ eV. The numbers at the top and right represent $N(\text{cm}^{-3})$.

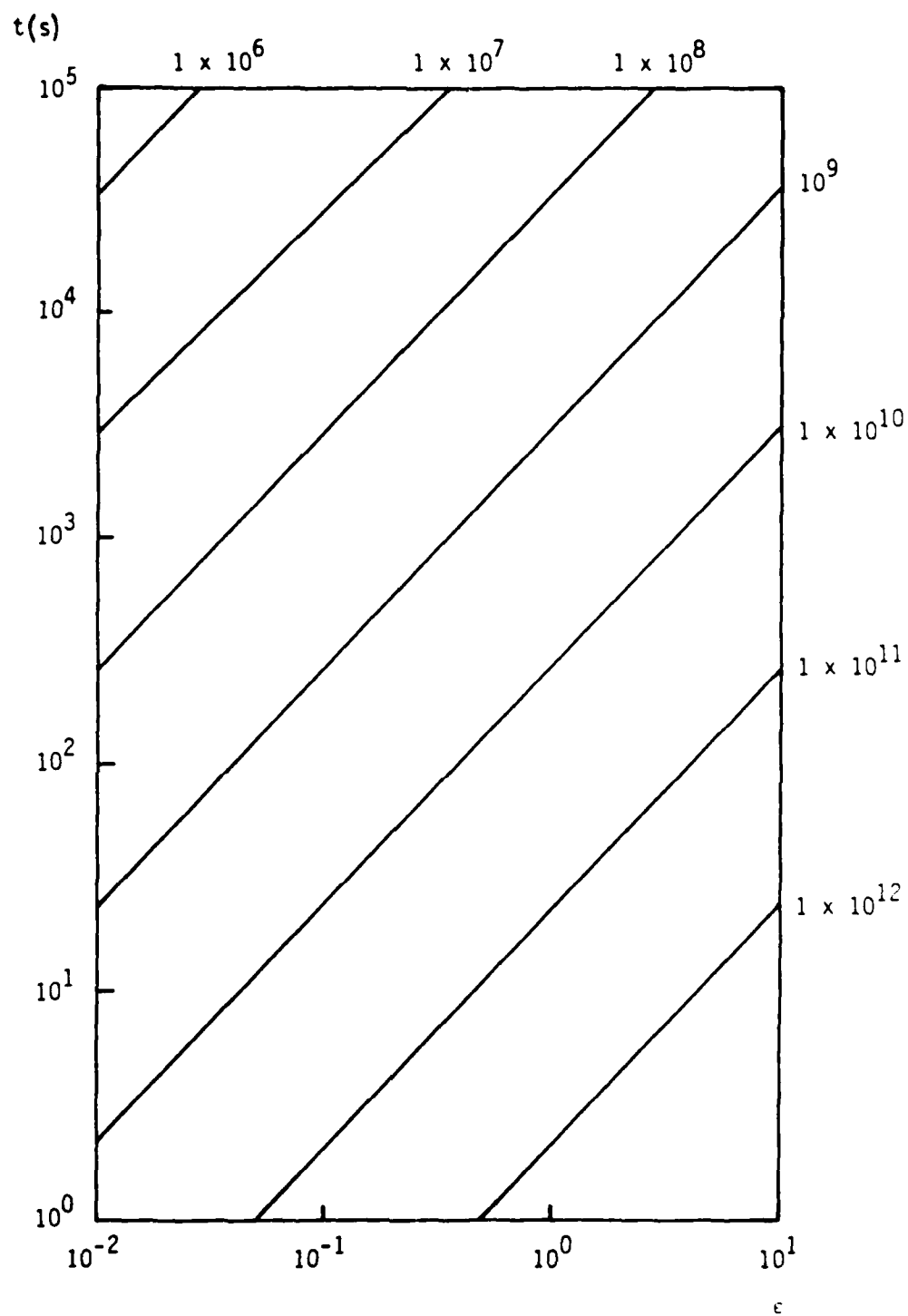


Figure 2.6b. $t(s)$ versus ϵ for $T_e = 0.518$ eV. The numbers at the top and right represent $N(\text{cm}^{-3})$.

with time to a power which depends on the electron temperature. The indicated functional behavior of long-term Fourier amplitude decay with time is a signature of the radiative recombination process.

REFERENCES

- 2.1 P. M. Banks and G. Kockarts, Aeronomy, Part A, Academic Press, ch. 10, 1973.
- 2.2 W. Knapp and K. Schwartz, Aids for the Study of Electromagnetic Blackout, National Technical Information Service, ch. 4, 1975.
- 2.3 H. H. Michels, F. T. Smith, and A. P. Hickman, Reaction Rate Handbook, T. Baurer and M. H. Bortner, Eds., General Electric Company, Space Division, Space Sciences Laboratory, ch. 16, 1979.
- 2.4 S. R. Goldman and J. L. Sperling, "Some Physical and Chemical Aspects of Striation Structure," J510-80-023/2128-02, JAYCOR, San Diego, California, ch. 8, 1980.
- 2.5 H. G. Booker, "Radio Scattering in the Lower Ionosphere," J. Geophys. Res., Vol. 64, No. 12, pp. 2164-2177, 1959.
- 2.6 D. Sappenfield, private communication.

3. NONADIABATICITY AND THE HIGH-ALTITUDE NUCLEAR ENVIRONMENT

3.1 INTRODUCTION

The magnetic moment is an adiabatic constant of motion in magnetic field configurations with sufficiently gentle magnetic field gradients and slow temporal variations. However, if spatial inhomogeneities in the magnetic field are large enough or if the magnetic fields change fast enough, the magnetic moment is not a reasonable constant of the motion.^{3.1-3.3} In fact, numerical studies of particle motion demonstrate a rather sharp transition between adiabatic and nonadiabatic behavior as the parameter $\lambda = \rho/L$ is increased.^{3.1-3.4} Here, $\rho = v/\Omega$ is the particle gyroradius for speed, v , and gyrofrequency, Ω , while L is the inhomogeneity scale length. Particles, whose motion does not conserve magnetic moment, generally have nonadiabatic changes in their magnetic moment as they pass through points of minimum (maximum) magnetic field strength on their guiding center trajectories. The magnitude of these nonadiabatic jumps depends on the particle pitch angle and gyration phase.

There are two situations where the nonadiabatic particle motion can influence the ionospheric and magnetospheric environments following a high-altitude nuclear burst. First, a nuclear burst can push aside the ambient geomagnetic field and temporarily create a new magnetic field configuration containing local extremums in magnetic field strength.^{3.5,3.6} Superthermal ions flowing down the field lines in this configuration can undergo nonadiabatic jumps in magnetic moment as they traverse these extremums. As a result, initial structure whose size is smaller than the maximum ion gyroradius is fuzzed on a size scale comparable to this gyroradius. Hence, nonadiabaticity, like charge exchange, supports the premise of outer scale length in the power spectral density being at least as large as the gyroradii of fast ions.^{3.6} Second, nuclear bursts may inject large quantities of superthermal ion material into the magnetosphere.^{3.7} However, only ions, whose trajectories sensibly conserve magnetic moment, can be confined on drift orbits in the magnetosphere and contribute to a magnetospheric ring current. These

ring currents not only have sharp gradients, which may directly influence electromagnetic transmissions from satellites, but by their inherent nature can affect the whole ionospheric and magnetospheric current system.^{3,7} For example, associated field-aligned currents may drive conventional ionospheric structuring mechanisms like the current-convective instability. Also, electron currents may permit shorting of ambipolar electric fields in the ionosphere and a concomitant increase in the basic ionospheric plasma diffusion rate. Changes in the rate of plasma diffusion can affect striation morphology.

This chapter shows the relevance of nonadiabatic scattering of ions to the phenomenology of the high-altitude nuclear environment. Section 3.2 gives a semi-quantitative description of conditions required for nonadiabatic changes in magnetic moment. Also, a Fokker-Planck model is described which is appropriate to situations where the jumps in magnetic moment are relatively small compared to the initial magnetic moment. Section 3.3 shows the results of an exact numerical evaluation of fast ion trajectories for a static magnetic field configuration with gradients which can be comparable to those associated with a high-altitude nuclear burst. These calculations clearly demonstrate that nonadiabatic jumps in magnetic moment can occur in an appropriately inhomogeneous magnetic field configuration. Section 3.4 shows that superthermal ions generated by a high-altitude nuclear burst can undergo nonadiabatic changes in magnetic moment in the magnetosphere. Section 3.5 summarizes the results and gives concluding remarks.

3.2 FOKKER-PLANCK MODEL FOR NONADIABATICITY

Numerical studies of particle motion in complex magnetic geometries show that particle trajectories begin to evince nonadiabatic behavior when^{3.1-3.4}

$$v/\Omega \gtrsim 0.04 L \quad , \quad (3.1)$$

and demonstrate large, nonperturbative changes in magnetic moment when^{3.2,3.4}

$$v/\Omega \gtrsim 0.1 L \quad . \quad (3.2)$$

For singly ionized monatomic oxygen ions with a speed, $v = 1 \times 10^8$ cm/s, and a magnetic field strength of 0.3 gauss, Eqs. (3.1) and (3.2) imply that $L \lesssim 140$ km

for the onset of nonadiabaticity and $L \lesssim 56$ km for very large changes in magnetic moment.

Whereas the magnetic moment, μ , can undergo jumps as particles traverse extremums in magnetic field strength, the sign of the jump, $\Delta\mu$, depends on the gyrophase of the electron at the minimum- (maximum) point. Hence,^{3.1}

$$\langle \Delta\mu \rangle \approx 0 \quad , \quad (3.3)$$

where the angle bracket denotes an average over gyrophase. The mean square quantity, $\langle \Delta\mu \rangle^2$,^{3.2} averaged over gyrophase, can be expressed as^{3.1-3.4}

$$\frac{\langle (\Delta\mu)^2 \rangle}{\mu^2} = A \frac{v^2}{v_{\perp 0}^2} \exp \left[-2 K(v^2/v_{\perp 0}^2) \frac{L}{\rho} \right] \quad , \quad (3.4)$$

where $v_{\perp 0}$ is the perpendicular particle speed at the minimum (maximum) point of magnetic field strength. The coefficient A can be taken to be roughly a constant,^{4.3.1-3.4} In general, $K(v^2/v_{\perp 0}^2)$ has a detailed complicated functional dependence which depends on geometry but the qualitative features of the function has the form illustrated in Figure 3.1.^{3.1,3.4} The value of $K(v^2/v_{\perp 0}^2)$ is a strong function of particle pitch angle, especially for trapped particles, $v^2/v_{\perp 0}^2 < 2$. The value of $K(v^2/v_{\perp 0}^2)$ increases with the pitch angle, i.e., $K(v^2/v_{\perp 0}^2) \gg 1$ for $(v/v_{\perp 0})^2 \rightarrow 1$. $K(v^2/v_{\perp 0}^2)$ is roughly constant (of the order of 1) for the regime $(v/v_{\perp 0})^2 \gtrsim 4$. Since for local perpendicular speed, v_{\perp} , local magnetic field strength, B , and particle mass, m ,

$$\mu = \frac{mv_{\perp}^2}{2B} \quad , \quad (3.5)$$

the change in pitch angle described by Eq. (3.4) goes to zero algebraically for small pitch angle and exponentially for large pitch angle. Nonadiabatic jumps in magnetic moment require oblique pitch angle.^{3.1,3.4}

A velocity space diffusion operator has previously been developed for the nonrelativistic limit using a Fokker-Planck formalism,^{3.2} appropriate to the limit $\langle (\Delta\mu)^2 \rangle / \mu^2 \ll 1$. According to Reference 3.2, the diffusion operator describing nonadiabaticity effects, N , has the following form,

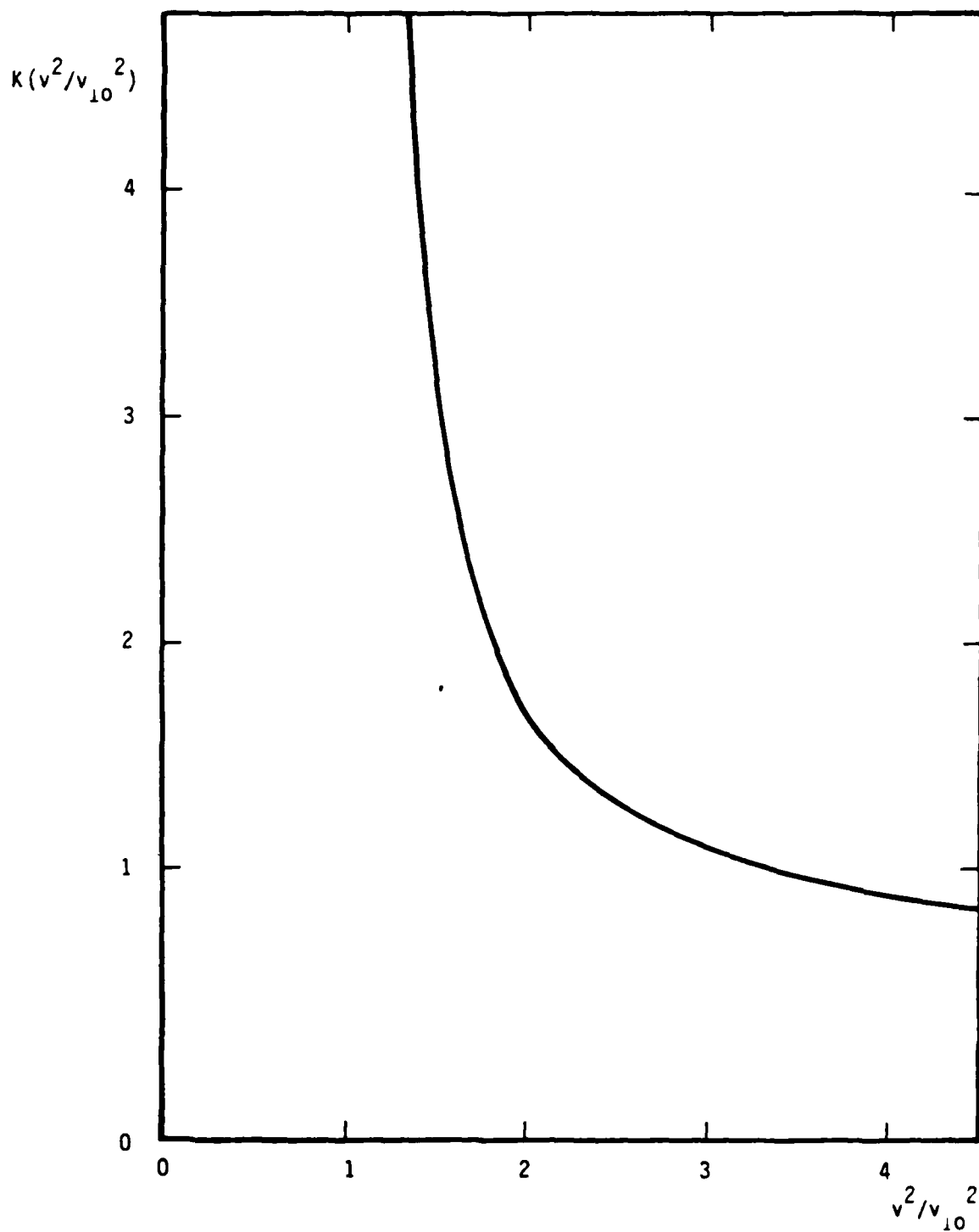


Figure 3.1. Qualitative plot of $K(v^2/v_{10}^2)$ versus v^2/v_{10}^2 .

$$N(\mu, \epsilon) f \equiv \frac{\partial}{\partial \mu} \left(\frac{\langle (\Delta \mu)^2 \rangle}{2 \Delta t} \frac{\partial f}{\partial \mu} \right) , \quad (3.6)$$

with f , the velocity distribution function. For trapped particles, Δt is the bounce period, while for untrapped electrons, Δt is the time required to traverse the magnetic field geometry of interest.

For application to the high-altitude nuclear environment, it is useful to rewrite Eq. (3.6) in terms of particle momentum components at the points which correspond to extremums in magnetic field strength. In particular,

$$N(p_{\perp 0}, p_{\parallel 0}) f = \left(\frac{p_{\parallel 0}}{p_{\perp 0}} \frac{\partial}{\partial p_{\perp 0}} - \frac{\partial}{\partial p_{\parallel 0}} \right) \frac{\langle (\Delta \mu)^2 \rangle}{2 \Delta t} \frac{m^2 B_0^2}{p_{\parallel 0}^2} f(p_{\perp 0}, p_{\parallel 0}) , \quad (3.7)$$

with

$$p_{\perp 0} = m v_{\perp 0} , \quad p_{\parallel 0} = m v_{\parallel 0} , \quad (3.8)$$

and the parallel velocity, $v_{\parallel 0}$, at the point with the minimum (maximum) magnetic field strength, B_0 .

An H-theorem can be derived from Eq. (3.7):

$$\begin{aligned} 0 &\geq \int d^3 p f(p_{\perp 0}, p_{\parallel 0}) N(p_{\perp 0}, p_{\parallel 0}) f(p_{\perp 0}, p_{\parallel 0}) \\ &= - \int d^3 p \frac{\langle (\Delta \mu)^2 \rangle}{2 \Delta t} \frac{m^2 B_0^2}{p_{\parallel 0}^2} \left[\left(\frac{p_{\parallel 0}}{p_{\perp 0}} \frac{\partial}{\partial p_{\perp 0}} - \frac{\partial}{\partial p_{\parallel 0}} \right) f(p_{\perp 0}, p_{\parallel 0}) \right]^2 . \end{aligned} \quad (3.9)$$

From Eq. (3.9) it follows that for the general case of initially oblique particle pitch angles, the nonadiabatic jumps in magnetic moment generally tend to drive the distribution function to isotropy while conserving energy. There are also special steady-state distribution functions corresponding to zero and ninety degree pitch angles, respectively.

In plasmas with rotational or translational symmetry there is a corresponding canonical momentum which is a constant of motion.^{3.8} This canonical momentum determines the trajectory in real space which can be traversed by the gyrocenter of a specific particle. Nonadiabatic changes in magnetic moment must preserve constant canonical momentum and so nonadiabaticity, by itself, does not necessarily imply particle diffusion across magnetic fields. However, nonadiabaticity can still result in the loss of particles by pushing them into loss cones. For systems which do not have a coordinate of symmetry, the kinetic diffusion operator, Eq. (3.7), has to be written in a more general form in order to accurately assess the diffusion associated with nonadiabatic changes in the magnetic moment.

3.3 EXAMPLE FOR THE VICINITY OF AN IONOSPHERIC NUCLEAR BURST

In this section we present numerical results which demonstrate that nonadiabaticity is a relevant process for magnetic field geometries with gradients comparable to those which might be expected in the vicinity of the magnetic bubble formed following an ionospheric nuclear burst. For these examples it was numerically convenient to use a simple mirror geometry to demonstrate the nonadiabatic changes in magnetic moment. The particular geometry chosen for the present analysis is appropriate to a straight, vacuum, mirror field:^{3.9}

$$B_z(r,z) = B_0 \left[\alpha - I_0\left(\frac{\pi}{L_0} r\right) \cos\left(\frac{\pi}{L_0} z\right) \right] , \quad (3.10a)$$

$$B_r(r,z) = - B_0 I_1\left(\frac{\pi}{L_0} r\right) \sin\left(\frac{\pi}{L_0} z\right) . \quad (3.10b)$$

Here α , L_0 , and B_0 are a numerical parameter, a scale length, and a magnetic field strength, respectively. These quantities are chosen to have values consistent with the high-altitude nuclear environment. The symbols, r and z , are the radial and axial coordinates of the straight cylinder, respectively. The functions, I_0 and I_1 , are the modified Bessel functions of the first kind and of order zero and one, respectively. The form for the fields assumes that only vacuum magnetic fields are present and neglects plasma diamagnetism.

Figures 3.2a-b, which are plots of $2\mu/mc^2(G^{-1})$ versus $z(km)$, are a consequence of the solution to the exact equation of motion in the magnetic field geometry specified by Eqs. (3.10a-b). The speed of light is represented by c . The values of $\alpha(13)$, L_0 (20 km), and B_0 (0.027 G) actually imply minimum and maximum magnetic field strengths on axis (i.e., $r = 0$) of ~ 0.32 and ~ 0.38 G, respectively. The particle considered is singly ionized monatomic oxygen with an initial pitch angle of 45° and an initial location of $r = 10$ km and $z = 0$ km. The magnetic field strength at the initial particle location is 0.3 G.

Figure 3.2a, which assumes an ion speed of 1×10^3 km/s, shows that the magnetic moment is not an adiabatic constant for the specified parameters. The initial ion position is at $z = -20$ km and the initial ion velocity is in the positive z -direction. Away from $z = 0$, there are oscillations in the magnetic moment which are directly related to the ion gyration about the magnetic field lines. Near the point of minimum magnetic field strength at $z = 0$, there is a nonadiabatic increase in magnetic moment. Just before $z = 20$ km, the particle's parallel velocity becomes zero and undergoes a single bounce motion (not shown in Figure 3.2a) before crossing the $z = 20$ km point. It is evident from Figure 3.2a that a particle which is initially untrapped can become temporarily trapped around a point of minimum magnetic field strength if the magnetic moment is not constant. Conversely, a particle which is initially trapped can become untrapped if the magnetic moment is not an adiabatic invariant. Such behavior is impossible for situations where the magnetic moment is sensibly constant.

Figure 3.2b assumes the same parameters as Figure 3.2a except that the ion speed is 2×10^3 km/s. The particle motion is initially in the positive direction and begins with the solid line at $z = -20$ km. As in Figure 3.2a, there are oscillations in the magnetic moment away from $z = 0$. Near $z = 0$ there is a mild nonadiabatic change in the magnetic moment but the ion continues to travel to $z = 20$ km. The particle trajectory corresponding to the dashed line begins at $z = -20$ km with initial ion velocity components identical to the final ones at $z = 20$ km for the solid line. The dashed line demonstrates a dramatically different behavior for the magnetic moment than the solid line. This line shows a substantial nonadiabatic increase in magnetic moment near the point of minimum magnetic field strength at $z = 0$. Beyond $z = 0$, the ion has a subsequent reversal in trajectory and the ion moves in the negative direction. Only part of this motion

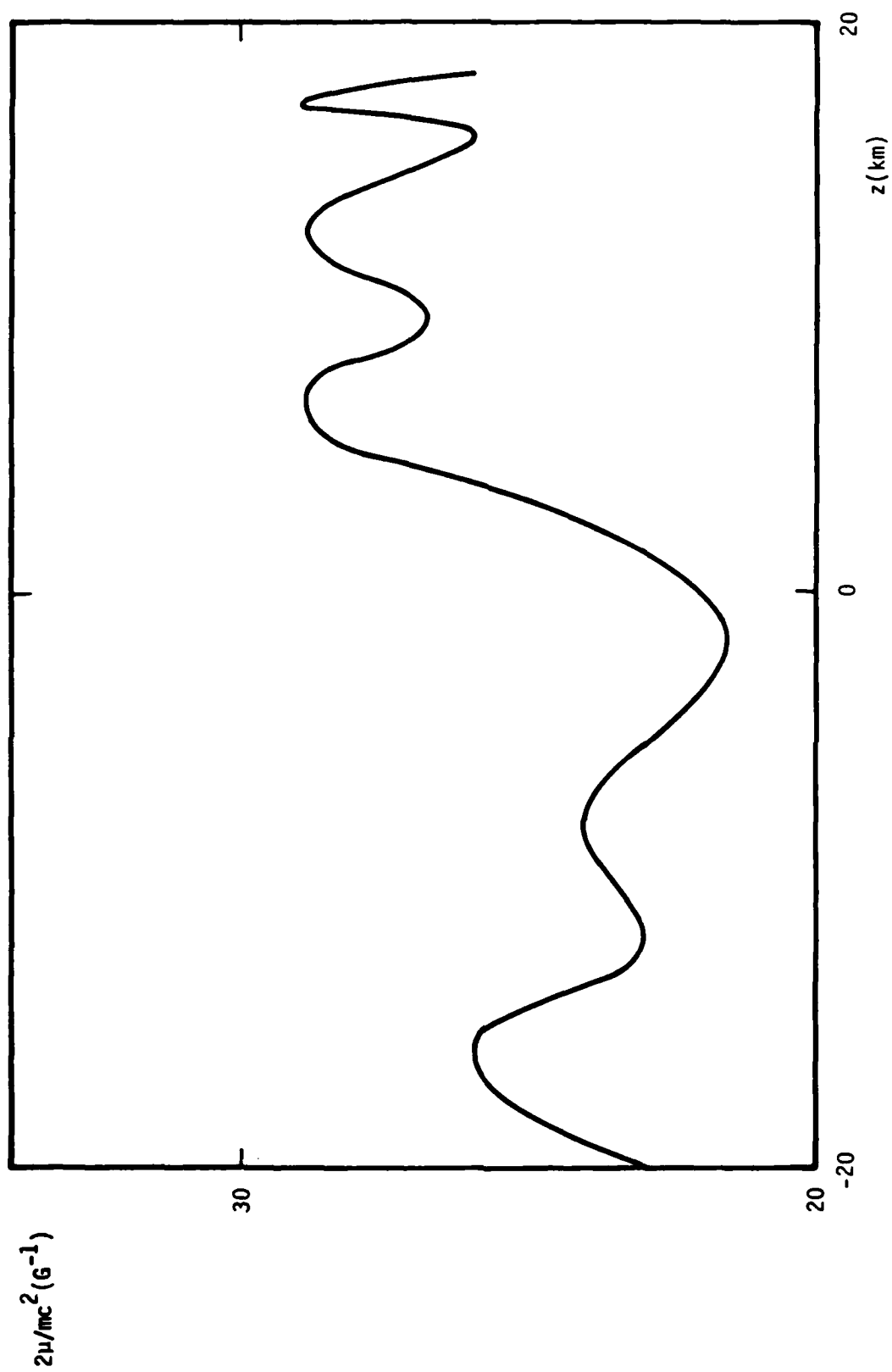


Figure 3.2a. $2\mu/mc^2 (\text{G}^{-1})$ versus $z(\text{km})$ for singly ionized monatomic oxygen ions with $v = 1 \times 10^3 \text{ km/s}$.

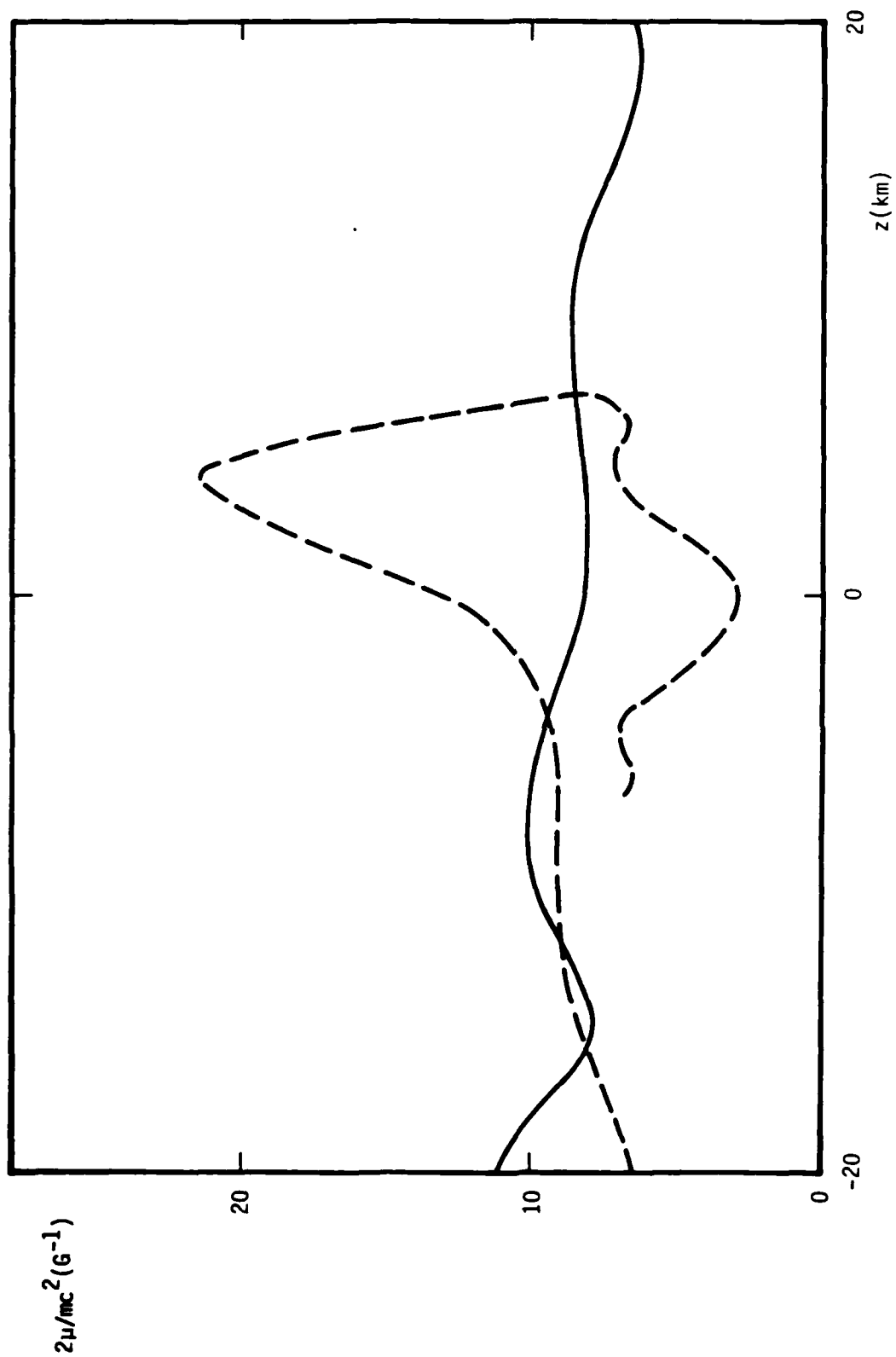


Figure 3.2b. $2\mu/mc^2(G^{-1})$ versus $z(km)$ for singly ionized monatomic oxygen ions with $v = 2 \times 10^3$ km/s.

in the negative direction is shown in Figure 3.2b. The trapping of the ion by the magnetic field is only temporary and eventually the ion crosses the $z = 20$ km point after one bounce motion. In addition to demonstrating the possibility of both trapped and untrapped particle dynamics when the magnetic moment is not conserved, Figure 3.2b shows that the nonadiabatic change in magnetic moment is a function of pitch angle and gyrophase. This result follows from the different trajectories associated with the solid and dashed lines.

During early times, nuclear bursts in the ionosphere strongly modify the ambient magnetic field geometry, for example, by creating magnetic bubbles.^{3.5-3.6} Energetic ions traveling through this geometry may cross points of minimum or maximum magnetic field strength with resulting substantial changes in magnetic moment and pitch angle. The nonadiabatic jumps in magnetic moment are a function of pitch angle and gyrophase.

Consider a structure consisting of energetic ions and having a size transverse to the magnetic field which is initially smaller than the maximum gyroradius possible for a given speed. It is evident that nonadiabaticity tends to broaden the transverse size and make it comparable to the maximum gyroradius. Nonadiabaticity supports the premise of minimum outer scale length being comparable to the early-time energetic ion-gyroradius.^{3.6}

3.4 NONADIABATICITY IN THE MAGNETOSPHERE

Following a high-altitude nuclear burst, ions may be injected into the magnetosphere. Only those ions, with reasonably constant magnetic moments, can be confined on drift orbits in the magnetosphere and contribute in a substantial way to the magnetospheric ring current. These currents, by virtue of their sharp gradients, may not only directly affect transmissions from satellites but also may have a direct impact on the whole ionospheric and magnetospheric current system.^{3.7} Associated field-aligned currents may drive conventional ionospheric structuring mechanisms like the current-convective instability. Also, electron currents may permit shorting of ambipolar electric fields in the ionosphere and permit a concomitant increase in the basic ionospheric plasma diffusion rate and the inner scale length of the power spectral density.

The consideration of nonadiabatic particle behavior permits a bound to be put on the maximum energy of ions confined to the magnetosphere. This bound does

not depend on a hypothetical anomalous mechanism but rather only depends on the inherent magnetic field geometry of the magnetosphere.

To demonstrate that nonadiabaticity is a valid consideration for ions injected into the magnetosphere following a nuclear burst, we consider a dipole magnetic field geometry for the earth^{3,10}

$$B_R = \frac{2M \sin(\theta_m)}{R^3} \quad (3.11a)$$

$$B_{\theta m} = \frac{M \cos(\theta_m)}{R^3} \quad (3.11b)$$

with $M = 8 \times 10^{25} \text{ G-cm}^3$. The radial distance from the center of the earth and the magnetic latitude are represented by R and θ_m , respectively. The radial and azimuthal magnetic field components are denoted by B_R and $B_{\theta m}$, respectively. The gradient scale length at the magnetic equator is

$$L_B \equiv |B_{\theta m} / (\partial B_{\theta m} / \partial R)|_{\theta_m=0} = \frac{R}{3} \quad (3.12)$$

Consider a singly ionized monatomic oxygen ion with a speed of $1 \times 10^3 \text{ km/s}$. The appropriate magnetic field strength and magnetic field gradient scale length for $R = 3.5 \times 10^4 \text{ km}$ at the magnetic equator are $1.87 \times 10^{-3} \text{ G}$ and $1.17 \times 10^4 \text{ km}$, respectively. The corresponding maximum possible ion-gyroradius, v/Ω , is $8.9 \times 10^2 \text{ km}$ and so

$$v/\Omega \approx 0.08 L_B \quad (3.13)$$

Hence, from Eq. (3.1) it follows that nonadiabaticity can preclude the long-term confinement of singly ionized monatomic oxygen ions with a speed of $1 \times 10^3 \text{ km/s}$ on the magnetic flux surface for $R = 3.5 \times 10^4 \text{ km}$ at the magnetic equator. In fact, Eq. (3.1) implies that ion speeds smaller than $5.2 \times 10^2 \text{ km/s}$ are probably necessary for long-term confinement on the flux surface being considered.

Equations (3.1), (3.11b), and (3.12) indicate that singly ionized ions with an atomic mass of α can be confined on flux surfaces with a radius of $R_{eq}(\text{km})$ at the magnetic equator for speeds $v(\text{km/s})$ satisfying the criterion

$$v < \frac{1.0 \times 10^{13}}{\alpha R_{eq}^2} \quad (3.14)$$

Equation (3.14) shows that the ability to confine energetic ions with a particular speed is decreased by higher altitude and larger atomic mass. For example, confinement of singly ionized monatomic oxygen ions with speeds of 1×10^3 and 2×10^3 km/s are limited to magnetic flux surfaces with R_{eq} less than $\sim 2.5 \times 10^4$ km and 1.8×10^4 km, respectively.

From the standpoint of particle kinetic energy, $W(\text{eV})$, Eq. (3.14) implies that

$$W < \frac{5.4 \times 10^{23}}{\alpha R_{eq}^4} \quad (3.15)$$

Hence, for a specified kinetic energy, ions with a lower atomic mass can be confined to a higher altitude than those of larger atomic mass. For example, singly ionized iron ions with energy below $\sim 2.5 \times 10^4$ eV can be confined to the flux surface with $R_{eq} = 2.5 \times 10^4$ km, while the corresponding limit for singly ionized monatomic oxygen ions is $\sim 8.6 \times 10^4$ eV.

3.5 SUMMARY AND CONCLUDING REMARKS

The magnetic moment is an adiabatic invariant for particle motion in a magnetic field geometry with sufficiently weak magnetic field gradients.^{3.1-3.4} Particles with sufficiently large speeds can have trajectories which do not preserve the constancy of the magnetic moment. This nonadiabatic behavior affects the high-altitude nuclear environment in two ways. First, the magnetic field geometry can be significantly altered by a high-altitude nuclear burst during early-times. Nonadiabaticity can cause pitch angle scattering of ions at points of maximum (minimum) magnetic field strength in this modified geometry. This process supports the premise of minimum outer scale length in the high-altitude nuclear environment being at least as large as the energetic ion-gyroradii. Second, ions injected into the magnetosphere following a high-altitude nuclear burst can be confined in the magnetosphere only if their kinetic energy is below a bound determined by the onset of nonadiabaticity. This result implies that the characterization of the ionic population in the magnetosphere and the effect of the ions on the ionosphere is influenced by the nonadiabatic scattering associated with the magnetospheric magnetic field.

REFERENCES

- 3.1 J. E. Howard, "Nonadiabatic Particle Motion in Cusped Magnetic Fields," Phys. Fluids, Vol. 14, No. 11, pp. 2378-2384, 1971.
- 3.2 I. B. Bernstein and G. Rowlands, "Diffusion in Velocity Space Associated with Nonadiabatic Changes in the Magnetic Moment of a Charged Particle," Phys. Fluids, Vol. 19, No. 10, pp. 1546-1550, 1976.
- 3.3 R. H. Cohen, G. Rowlands, and J. H. Foote, "Nonadiabaticity in Mirror Machines," Phys. Fluids, Vol. 21, No. 4, pp. 627-644, 1978.
- 3.4 S. Hamasaki, N. A. Krall, and J. L. Sperling, "Parametric Study of the Relativistic Electron Ring," J510-81-067, JAYCOR, San Diego, CA, 1981.
- 3.5 Ralph Kilb, private communication.
- 3.6 S. R. Goldman and J. L. Sperling, "Some Physical and Chemical Aspects of Striation Structure," J510-80-023/2128-02, Interim Final Report for Period 1 February 1979 to 15 August 1980, JAYCOR, San Diego, CA, 1980.
- 3.7 J. F. Vesecky, J. W. Chamberlain, J. M. Cornwall, D. A. Hammer, and F. W. Perkins, "Irregularities in Ionospheric Plasma Clouds: Their Evolution and Effect on Radio Communications," JSR-80-15, SRI International, Arlington, VA, pp. III-31 - III-34, 1980.
- 3.8 H. Goldstein, Classical Mechanics, Addison-Wesley, ch. 7, 1965.
- 3.9 S. Hamasaki, H. H. Klein, N. A. Krall, J. B. McBride, and J. L. Sperling, "Microwave Heating of the Elmo Bumpy Torus Relativistic Electron Ring," Phys. Fluids, Vol. 24, No. 9, pp. 1706-1715, 1981.
- 3.10 J. C. Brandt and P. Hodge, Solar System Astrophysics, McGraw-Hill, pp. 397-399, 1964.

DISTRIBUTION LIST

DEPARTMENT OF DEFENSE

Defense Nuclear Agency

ATTN: STNA
ATTN: NAFD
ATTN: RAEF
ATTN: NATD
ATTN: RAAE, P. Lunn
3 cy ATTN: RAAE
4 cy ATTN: TITL

Defense Technical Information Center
12 cy ATTN: DD

DEPARTMENT OF THE ARMY

US Army Nuclear & Chemical Agency
ATTN: Library

US Army Satellite Comm Agency
ATTN: Doc Con

DEPARTMENT OF THE NAVY

Naval Research Lab

ATTN: Code 4720, J. Davis
ATTN: Code 4780
ATTN: Code 7500, B. Wald
ATTN: Code 4780, S. Ossakow
ATTN: Code 6700
ATTN: Code 7950, J. Goodman
ATTN: Code 4187
ATTN: Code 4700

Theater Nuc Warfare Proj Office
ATTN: PM-23, D. Smith

DEPARTMENT OF THE AIR FORCE

Air Force Technical Applications Ctr
ATTN: TN

Air Force Wpns Lab
ATTN: SUL
ATTN: NTYC
ATTN: NTN

DEPARTMENT OF ENERGY CONTRACTOR

Los Alamos National Lab

ATTN: MS 664, J. Zinn
ATTN: P. Keaton
ATTN: D. Simons
ATTN: MS 670, J. Hopkins
ATTN: T. Kunkle, ESS-5
ATTN: R. Jeffries
ATTN: J. Wolcott
ATTN: C. Westervelt

DEPARTMENT OF DEFENSE CONTRACTORS

Berkeley Research Associates, Inc

ATTN: S. Brecht
ATTN: C. Prettie
ATTN: J. Workman

DEPARTMENT OF DEFENSE CONTRACTORS (Continued)

General Research Corp

ATTN: B. Bennett

Geo-Centers, Inc

ATTN: E. Marram

Honeywell, Inc

ATTN: G. Collyer, Avionics Dept
ATTN: G. Terry, Avionics Dept

JAYCOR

4 cy ATTN: J. Sperling
4 cy ATTN: S. Hamasaki

Kaman Sciences Corp

ATTN: T. Stephens

Kaman Tempo

ATTN: DASIAC

Mission Research Corp

ATTN: R. Hendrick
ATTN: C. Lauer
ATTN: R. Kilb
ATTN: F. Fajen
ATTN: R. Bigoni
ATTN: G. McCartor
ATTN: F. Guigliano
ATTN: Tech Library
ATTN: S. Gutsche
ATTN: R. Bogusch

Pacific-Sierra Research Corp

ATTN: H. Brode, Chairman SAGE

R&D Associates

ATTN: B. Yoon

Science Applications, Inc

ATTN: L. Linson
ATTN: C. Smith
ATTN: E. Straker
ATTN: D. Hamlin

Science Applications, Inc

ATTN: J. Cockayne

SRI International

ATTN: G. Price
ATTN: R. Tsunoda
ATTN: J. Vickrey
ATTN: W. Chesnut
ATTN: R. Livingston
ATTN: D. Neilson
ATTN: J. Petrickes
ATTN: D. McDaniels
ATTN: R. Leadabrand
ATTN: M. Baron
ATTN: A. Burns
ATTN: C. Rino
ATTN: G. Smith
ATTN: V. Gonzales
ATTN: W. Jaye

DEPARTMENT OF DEFENSE CONTRACTORS (Continued)

Visidyne, Inc

ATTN: C. Humphrey
ATTN: O. Shepard
ATTN: W. Reidy
ATTN: J. Carpenter

EOS Technologies, Inc

ATTN: B. Gabbard

DEPARTMENT OF DEFENSE CONTRACTORS (Continued)

R&D Associates

ATTN: R. Lelevier
ATTN: C. Greifinger
ATTN: R. Turco
ATTN: H. Ory
ATTN: W. Wright
ATTN: M. Gantsweg
ATTN: W. Karzas
ATTN: F. Gilmore

DATE
ILME